MAGNETIC MACHINES FOR MICROENGINE POWER GENERATION

A Dissertation
Presented to
The Academic Faculty

By

David Patrick Arnold

In Partial Fulfillment
of the Requirements for the Degree
Doctor of Philosophy in the
School of Electrical and Computer Engineering

Georgia Institute of Technology
December 2004

MAGNETIC MACHINES FOR
MICROENGINE POWER GENERATION

Approved by:

Dr. Mark G. Allen, Advisor

Dr. Oliver Brand

Dr. Ronald G. Harley

November 12, 2004

ACKNOWLEDGEMENTS

I would like to first thank Prof. Allen for the many opportunities and experiences during my time at Georgia Tech. I also graciously thank my dissertation reading committee members, Prof. Brand and Prof. Harley for helping to guide this research and reviewing this document. Also, I extend thanks to Prof. Frazier and Prof. Hesketh for sitting on my defense committee.

I want to acknowledge all the members of the Microsensor and Microactuator Group. In particular, I thank Dr. Florent Cros for the memorable days of mentoring during my first years at Tech. I also thank Dr. Iulica Zana and Dr. Jin-Woo Park for their invaluable efforts and assistance during this research. I extend special thanks to Richard Shafer for his technical assistance in helping setup experiments, locating materials, and seemingly endless bits of wisdom for making things work. I also thank Gary Spinner and the Microelectronics Research Center (MiRC) cleanroom staff for their technical assistance and support of the cleanroom facilities, and lastly the MiRC support staff, including Purnima, Jana, Melissa, Diane, and Jennifer.

I thank many people at MIT for their assistance on this project. First, I owe Prof. Lang special thanks for his dedicated collaboration on this project. I will always remember the many hours of phone conferences, milestone setting, etc., all filled with learning. I thank Sauparna Das for the design and modeling of the generators, and for the enjoyable and productive time we spent in both Boston and Atlanta. I also thank Prof. Epstein for spearheading the microturbine project, and the many other unnamed members of the MIT Gas Turbine Lab. Also at MIT, I extend gratitude to Prof. Freeman and Salil Desai for the use of their microvision image analysis system.

From Clark Atlanta University, I thank Prof. Veazie for his assistance in mechanical characterization and collaboration on the mechanical integrity for the microengine. Also from CAU, I acknowledge Dr. Yeun-Ho Joung and Brian Shonkwiler.

This research could not have been possible without financial assistance. The project was supported by the Army Research Office (DAAG55-98-1-0292) and Army Research Laboratory under the Collaborative Technology Alliance Program (DAAD19-01-2-0010). I also graciously acknowledge the National Science Foundation for my graduate research fellowship, which carried me from my master's degree through the first few years of my Ph.D. work.

Finally, none of this would be possible without the love and support of my family. I thank my parents for the past 27 years; for teaching me life's basics; for providing opportunities to grow and explore as a child, teenager, and adult; for teaching me right from wrong; and most importantly, for equipping me with the ability to make good decisions. Lastly, I thank my wife, Jennifer, for the most wonderful devotion that can only come from a spouse. Thank you for being there, for patiently supporting me, and for loving me all the way.

TABLE OF CONTENTS

LIST OF FIGURES

LIST OF TABLES

SUMMARY

This dissertation presents an investigation of miniaturized magnetic induction and permanent magnet (PM) machines intended for portable power generation in a novel device, known as a microengine. Similar to a macroscale turbogenerator, a microengine comprises a small, gas-fueled turbine engine for converting chemical fuel energy into mechanical power and an integrated electrical generator for converting mechanical power to electrical power. Such a system is proposed as a refuelable, 10-100 W, portable power source with higher power densities and lower lifetime costs than conventional batteries. The focus of the research is on the design, fabrication, and characterization of microfabricated magnetic machines integrable with microengines for high-density electrical power generation.

To begin this research, innovative microfabrication techniques were developed to permit magnetic machine components to be embedded within micromachined (etched and wafer-bonded) silicon for eventual integration within a silicon-based microengine system. Using these fabrication techniques, both magnetic induction machines and PM machines were designed, fabricated, and characterized. Both types of machines used planar geometry (axially directed magnetic fields) for compatibility with typical microfabrication processes and were nominally 10 mm in diameter and 1.5-2.3 mm in thickness.

First, two-phase, eight-pole induction machines were constructed within silicon substrates using Cu coils in a laminated, slotted ferromagnetic NiFe or CoFeNi stator core. Silicon etching, wafer bonding, and electrodeposition were used to form all of the magnetic machine components. The induction machines were characterized in motoring

mode using tethered rotors and demonstrated motoring torques of up to 2.5 μN·m. These results verified the capability of a integrating a magnetic machine within bulk-micromachined silicon.

Next, PM machines were fabricated using a hybrid microfabrication/assembly approach. Three-phase, eight-pole stators were built using surface wound electroplated Cu coils on ferromagnetic NiFeMo (Moly Permalloy) substrates. Rotors were formed using magnetically patterned SmCo as the PM and FeCoV (Hiperco 50) as a back iron. The PM machines were tested in generating mode with free-spinning rotors, powered by an air-driven spindle. This enabled the demonstration of 2.6 W of mechanical-to-electrical power conversion and continuous DC power generation of up to 1.1 W at 120 krpm rotor speed.

The primary contributions of this work are (1) the demonstration of a magnetic induction machine with power magnetic machine components fully integrated within micromachined silicon and (2) the demonstration of multi-watt power conversion from a microfabricated PM generator. These two achievements represent progress in the ongoing development of silicon-based microengines. Also, while this research focused on magnetic machines for microengines, the fabrication technologies and devices can be applied to a variety of other applications (e.g. pumps, valves, etc.).

CHAPTER 1

INTRODUCTION

This dissertation presents an investigation of miniature magnetic induction and permanent magnet (PM) machines intended for compact, portable, electrical power generation. Chapter 1 introduces the concept of microengine power generation, reviews previously reported micromotors and microgenerators, and presents the challenges for integrating magnetic machinery into a microfabricated microengine. Chapter 2 presents several fabrication processes developed to enable the fabrication of magnetic machine components, particularly within silicon microstructures. Chapter 3 presents an optimization of magnetic laminations, based on microfabrication constraints. Chapter 4 details the design, fabrication, and characterization of silicon-based, magnetic induction machines. Similarly, Chapter 5 details the development of surface-wound, permanent magnet machines. Finally, conclusions and opportunities for future work are presented in Chapter 6.

1.1 Origin and History of the Problem

The power demands of modern electronic devices are quickly outpacing the energy and power density of today's best batteries. This has driven the development of new, compact electric power sources, coined as "Power MEMS," in the 10-100 watt range for use in portable electronics, self-powered sensors, robotic devices, etc. [1]. One novel approach, first proposed by A. H. Epstein and S. D. Senturia [2-4] and shown in Figure 1.1, is a microengine—a small (few cubic centimeter) gas-fueled turbine engine coupled to an electrical power generator. Such a system is enabled by modern

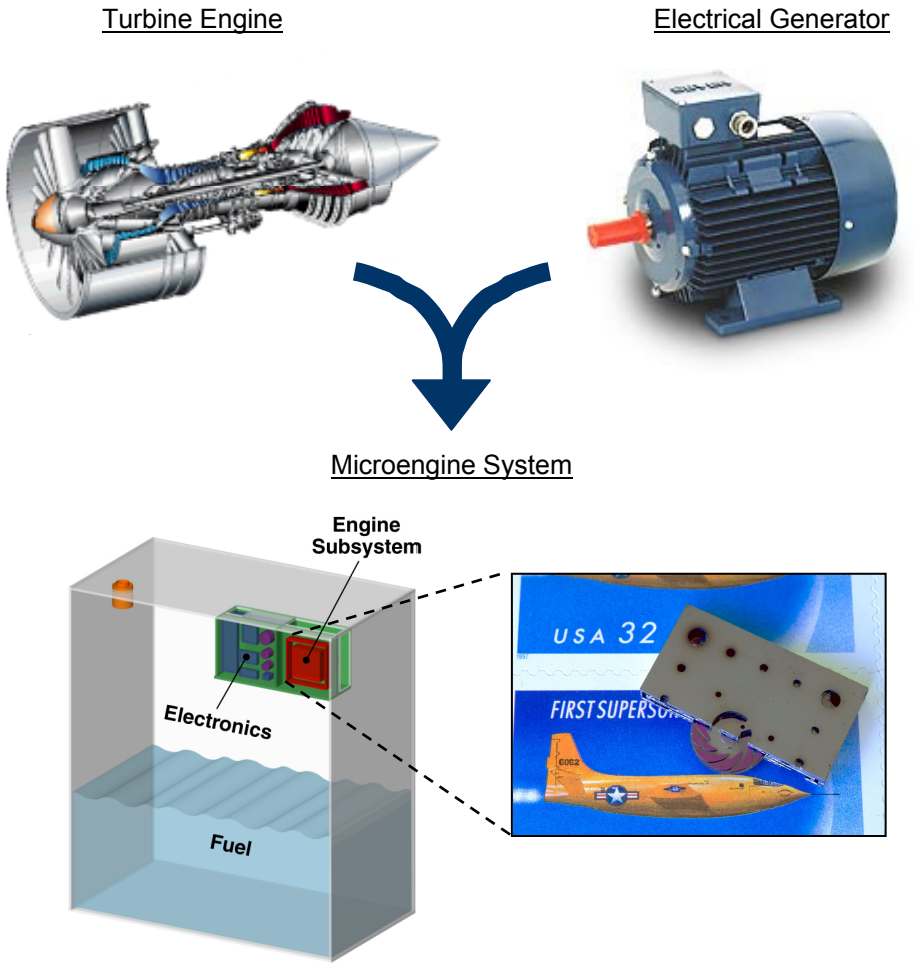

Figure 1.1. Microengine concept (Figure courtesy of Stuart Jacobson, MIT).

microfabrication techniques and has the potential to reduce the mass, life-cycle costs, and cumbersome logistics of conventional batteries while providing uninterrupted high-density power. For perspective, modern batteries have energy densities of 100-400 W·hr/kg, advanced fuel cells are promising 400-700 W·hr/kg, while hydrocarbon fuels boast 12,000-14,000 W·hr/kg. If microengines can achieve the 30-40% efficiency of their macroscale turbogenerator counterparts [5], net energy densities in excess of 3,500 W·hr/kg are possible.

1.2 Microengine Concept

Led by the Massachusetts Institute of Technology (MIT), silicon-based microengines have been under investigation since 1995. The complex and highly interdisciplinary nature of this device has spawned research and development across many research areas at several universities. The ultimate goal, as shown in Figure 1.2, is a structure consisting of a hydrocarbon fueled gas turbine with a fully integrated electric power generation system, achieved via deep reactive ion etching (DRIE) and fusion bonding of multiple silicon wafers. The key component is a composite, free-spinning, multilevel silicon disk, which functions as a compressor, turbine, and generator rotor. This rotor is supported by gas-lubricated air bearings to minimize the mechanical losses and enable sustained high-speed operation in excess of 1 Mrpm. All of the fluidic plumbing and generator stator components are integrated into the layers of silicon surrounding the rotor.

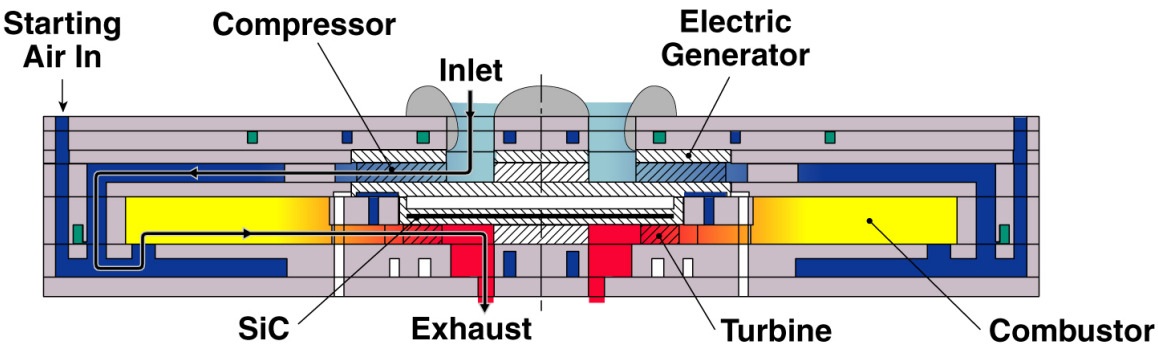

Figure 1.2. Proposed silicon-based, multi-wafer microengine design by MIT (Figure courtesy of Stuart Jacobson, MIT).

A variety of increasingly complex devices have been developed to demonstrate various subsystem elements critical to the overall design. First was a microbearing rig [6-9], which permitted rotational speeds of only 60 krpm, but helped to verify the design of the turbine section of the rotor. Next came two microcombustion systems [10-12], which included no moving parts, but were used to verify the feasibility and sustainability of microscale combustion. Then came a second-generation bearing rig [13,14] with improved bearings, which served as a test bed for the compressor section of the rotor and experimentally verified ultra-high speed (>1 Mrpm) rotation. Other supporting work has focused on materials research [15-17] and fabrication technologies [18-21]. In summary, relevant progress has been made in the development of the turbine to convert fuel into mechanical energy. The next section focuses on the machinery to convert the mechanical energy into electrical energy.

1.3 Micromotors/Microgenerators

A generator is used to convert the mechanical energy of the turbine rotor into usable electric power. For compatibility with the silicon-based microturbine, this machine must support high rotational speeds (~1 Mrpm) and withstand high operating temperatures (~300°C). In addition, it must be fabricated using processes that permit integration with the multi-wafer bonded silicon microstructure, a significant design and fabrication challenge. This shapes the goal of this dissertation: to investigate microscale power generation using magnetic micromachines that could be incorporated within a silicon-based microengine system. Specifically, machines should be designed using compatible geometries, fabrication methods, and operating temperatures, but monolithic integration with a microturbine, 1 Mrpm rotor speeds, and the use of air bearings to support rotation are long term milestones and outside the scope of this thesis.

1.3.1 Microgenerators for Microengines

Initially, the microengine design was based on the use of an electrostatic induction machine [22-28]. The machine, designed using a silicon-based, fusion-bond-compatible process, used six phases and 131 pole pairs, and measured 3.8 mm in diameter and approximately 1 mm in thickness [22]. First tested using tethered rotors in motoring mode, a maximum torque of 0.22 μN·m was achieved for a 90 V, 300 kHz excitation [23]. Then, a microfabricated structure was built to characterize the machine with a free-spinning rotor [24-28]. While intended as a fusion-bonded silicon stack, the five device layers were ultimately clamped together, rather than bonded, for testing. Initial characterization indicated a maximum torque of 0.3 μN·m (26 $N \cdot m/m^3$ torque density) at 15 krpm, corresponding to a shaft power of 0.5 mW (45 kW/m^3 power

density) [24]. The machine was subsequently redesigned to incorporate improvements in the stator for minimizing parasitic capacitances. This second-generation build resulted in a maximum torque of 3.5 μN·m (309 N·m/m^3) at speeds in excess of 55 krpm, corresponding to 20 mW (1.8 MW/m^3) of motoring power [25,26]. Even more recently, the machine successfully demonstrated generation of ~0.1 mW of output power at 245 krpm [27,28].

While this monolithically integrated, silicon-based generator represented a monumental step toward a fully integrated microengine, the electrostatic induction principle suffers from three challenges for use in a microengine: a very small air gap (~4 μm) results in high windage losses (fluidic drag); high voltages and small gaps between conductors can result in electrical breakdown of the dielectric layers; and uncompensated parasitic capacitances can result in an imbalanced phase stimulus. All of these effects limit the maximum power density and machine speed.

Magnetic machines may offer the following advantages over their electrostatic counterparts: higher power densities, higher efficiencies (e.g., lower windage losses as a result of larger rotor-stator air gap), less stringent fabrication tolerances (e.g., larger air gap), and simpler power electronics. They also operate at lower voltages, higher currents, and lower frequencies and are therefore easier to integrate with typical electronic devices. These advantages come at the expense of increased fabrication complexity.

First-generation, "proof-of-concept" magnetic machines were explored for use in the microengine [29-35]. Two-phase induction machines were designed with either six or eight poles. The devices were fabricated using SU-8 micromolding and multilevel electroplating of Cu and NiFe on NiFe substrates, and measured 2 mm in thickness and 4

mm in diameter. Characterized using tethered rotors, the six-pole design achieved a maximum torque of ~0.3 μN·m (12 $N \cdot m/m^3$ torque density) using a 6 A_{pk}, 90 kHz excitation, but was severely limited by eddy currents in the unlaminated stator. While the machines successfully demonstrated electromechanical power conversion, the structures were not integrable with the proposed microturbine; the fabrication was not silicon-based or wafer-bond compatible, and the presence of the SU-8 limited the operating temperature to ~200°C.

Magnetic structures are quite difficult to fabricate within the system-level constraints of the silicon-based microengine. Electrostatic devices can be built using relatively thin films and surface micromachining techniques, whereas magnetic machines require voluminous conductors and magnetic regions to support high currents and magnetic flux. These larger structures add mass and volume to the stator, and more importantly to the rotor. Incorporating large volumes of dense, relatively low-strength (compared to silicon), magnetic alloys into a high-speed spinning rotor poses a major material and mechanical design challenge. As compared to rotors used for the previously demonstrated electrostatic induction machine [24-28], the additional mass and non-uniform density distribution of a composite magnetic rotor adversely affects the mechanical rotor integrity and bearing stability in the following ways: higher stresses, larger radial and bending deformations, and potential plasticity and poor adhesion of the magnetic materials within the rotor.

1.3.2 Other Magnetic Micromachines in the Literature

Various other microfabricated magnetic machines, not designed for heat engine applications, have also been reported in the literature. First in 1993, H. Guckel et al. [36]

reported surface-micromachined, planar variable reluctance motors, constructed of electrodeposited nickel using the LIGA process. Speeds of 30 krpm were achieved with a 55-μm thick, 285-μm diameter rotor using 0.6 A_{pk} excitation. A later publication in 1994 by H. Guckel et al. reported a torque of 100 μN·m and speeds of up to 150 krpm [37]. Also in 1993, C. H. Ahn et al. [38] reported a variable reluctance micromotor with fully integrated stator and coils, fabricated using multilevel electroplating of Cu and NiFe in photodefined polyimide molds. Speeds of 500 rpm were demonstrated for a 40-μm thick, 500-μm diameter rotor using a 200-mA excitation with a projected maximum torque of 3.3 nN·m. Later, in 1995, Jungreis and Kelley [39] reported an interesting design coined as an axial air gap wobble motor. Macromachined prototypes were built using 8.5-mm and 50-mm diameter rotors, and demonstrated speeds of up to 218 rpm and 98 rpm, respectively, and a theoretical design for a 1-mm diameter micromachined version was given but not implemented.

In addition to these variable reluctance motors, permanent magnet (PM) motors have also been investigated. In 1993, Wagner et al. [40] demonstrated rotational machines using rare-earth PM's over simple electroplated gold coils. Using a 1 mm thick, 1.4 mm diameter rotor, torques of 100 nN·m were achieved at 2 krpm using 500-mA. In 1996, Kamper et al. [41] and, later in 1998, Berg et al. [42] reported the development of a 1.9-mm diameter PM synchronous micromotor constructed using conventional machining and LIGA technology. The device achieved speeds of up to 200 krpm and torques of 7.5 μN·m, and, using an integrated micro gear box, could deliver 300 μN·m of torque. More recently in 2000, P.-A. Gilles et al. [43] demonstrated a planar, three-phase, synchronous PM machine using magnetic thrust bearings. An initial, conventionally built

prototype used an 18-mm rotor that reached 40 krpm and 50 μN·m of torque for 0.5-A_{pk} excitation. Smaller, hybrid structures were proposed using micromachined coils and a 0.5-mm thick, 8-mm diameter, macromachined $SmCo_5$ rotor, which would be magnetized with alternating poles before assembly. And lastly, in 2001, C. Yang et al. [44] reported similar 1.5-mm thick axial-flux permanent magnet machines using 1-mm and 2-mm diameter rotors, built using LIGA to achieve six levels of copper windings in the stator and electro discharge machining (EDM) to form a SmCo permanent magnet rotor disc. The machines demonstrated 18 krpm and 25 krpm and 1.5 μN·m and 2.8 μN·m, for the 1- and 2-mm designs, respectively.

All of the machines listed to this point were designed and tested as micromotors, but microgenerators have also been reported. In 1996, T. G. Wiegele [45] reported a planar microturbogenerator intended to be operated as a switched reluctance machine. The machine used a 100-300-μm thick, 3.5-mm diameter rotor and demonstrated speeds up to 4.5 krpm, but the power generation portion was never implemented. In 2004, A. S. Holmes et al. [46] reported an axial-flow microturbine power generation system using a permanent magnet generator. The device was fabricated using a combination of DRIE, electroplating, and laser micromachining using silicon, SU-8, electroplated copper, and conventional NdFeB permanent magnets. The composite turbine/generator rotor was supported by conventional ball-race bearings and measured 1 mm in thickness and 6 mm in diameter. The overall machine was 0.5 cm^3 and demonstrated 1 mW of power generation at 30 krpm when placed in an air-stream of 35 L/min.

This summary provides some background of what has been accomplished using microfabricated motors and generators. While these devices show the potential for

magnetic generation, none are directly compatible with the proposed microengine; they do not use an integrable fabrication process and were not designed for high temperature and high speed operation. The next section discusses the relevant fabrication technologies required to achieve such devices.

1.4 Fabrication Considerations

This section first briefly reviews two traditionally distinct microfabrication technologies: (1) bulk micromachining and wafer bonding of silicon and (2) electrodeposition and lamination of magnetic components, as depicted in Figure 1.3. This is followed by a summary of the challenges for merging these two methods for the construction of Si-based magnetic machines embedded in a silicon microengine.

1.4.1 Bulk Micromachining & Wafer Bonding of Silicon

Bulk micromachining of silicon MEMS typically relies on either wet etching, using KOH or other aqueous etchants, or dry etching technologies, such as DRIE. In conjunction with deep silicon etching, wafer bonding is a popular fabrication technique to achieve large mechanical structures, fluidic channels, sealed cavities, membranes, floating elements, etc., as reviewed by M. A. Schmidt [47]. Fusion, or direct, bonding is preferred to other bonding methods (e.g., anodic, eutectic, polymer, glass frit, etc.) because it is simple and low cost, eliminates thermal mismatch issues, requires no intermediate layers, and results in a strong, uniform bond. However, fusion bonding of silicon requires chemically clean, polished surfaces and a post-bond anneal to strengthen the bond; typically, an RCA clean is performed before bonding, and post-bond annealing is performed at temperatures from 300–1100°C [48].

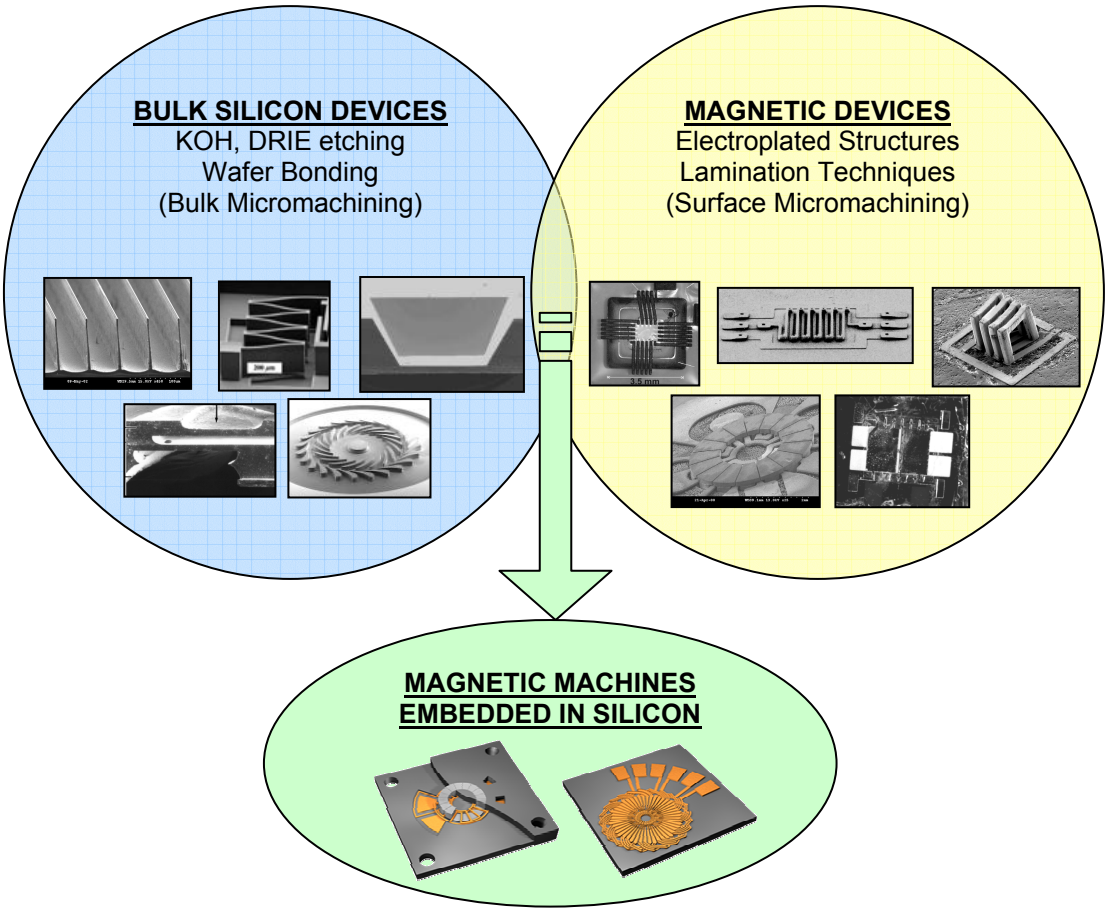

Figure 1.3. Schematic depicting the synergy of bulk silicon micromachining and magnetic microfabrication approaches for achieving magnetic machines embedded in a silicon microengine.

The most commonly reported fusion bonding cycle is 1100°C for 1 hr under nitrogen in a tube furnace, resulting in a bond strength approaching that of the silicon itself [48]. Many metals used in MEMS devices cannot withstand such an extreme temperature (e.g., the melting point of Cu is 1085°C), but in many cases, such strong bonds are not required. There have been many previous investigations reporting high bond strengths using "low-temperature" silicon-silicon fusion bonding [20,48-54]. The literature offers some processing suggestions for metal compatibility [53] and shows that a protective oxide layer can be used to protect the silicon surface during various micromachining steps before bonding [21]. However, an investigation of embedded electroplated metals in fusion-bonded silicon has not been previously demonstrated.

1.4.2 Electrodeposition & Lamination of Magnetic Components

In contrast to bulk-etched silicon devices, magnetic actuators [55], power converters [56], and motor/generators [29-46] form a distinctly different class of MEMS devices, in terms of materials, fabrication approach, and integration strategy. Typically, magnetic devices are built on a variety of substrates in a surface-micromachining fashion, using multilevel metallization of electroplated materials in polymer micromolds [57]. Electrodeposition has proven to be an effective method for building the thick (tens or hundreds of micrometers) conductive and magnetic components to support the high currents and magnetic fluxes required for optimum electromechanic coupling and maximum power density.

One key design consideration for these types of devices is minimization of frequency-dependent core losses, which result from hysteresis and eddy current effects. Hysteresis losses can be minimized by careful control of the ferromagnetic alloy

composition and are typically considered minor losses. Eddy current losses are minimized either by using high-resistivity magnetic materials or by laminating the material into dielectrically separated thin sheets. Conductive metallic alloys such as NiFe are often preferred over high-resistivity ferrites because they support larger saturation flux densities and thus higher power densities. In macroscale magnetic devices, low-loss laminated cores are typically achieved by stacking alternating layers of core material and insulating material and laminating the entire stack together. In contrast, incorporating laminations into batch-fabricated microscale devices poses a manufacturing challenge.

The lamination thickness should be reduced to the order of the magnetic skin depth (typically 1-100 μm range) while maintaining large total core thicknesses (10 μm-1 mm) to prevent saturation. These requirements dictate large numbers of thin, high-aspect-ratio laminations, which are difficult to achieve using conventional microfabrication techniques, but several approaches have been proposed: mechanical lamination of polymer-coated magnetic foils [58]; repetitive deposition of polymer insulator, seed layer, and electroplated magnetic layers [59]; alternating electrodeposition of magnetic and sacrificial metal layers [60]; alternating sputtering of thin-film magnetic and dielectric layers [61]; and one-step electroplating of high-aspect-ratio vertical structures [62]. Although these approaches have all demonstrated reduction of eddy currents, processability and scaling remain unaddressed issues. The applicability of any of these techniques depends on the specific core geometry and desired lamination thickness. It should be noted that these are primarily surface-micromachining techniques, and most are not silicon-based techniques.

1.4.3 Integration of Magnetic Machine Components in Silicon

It follows that magnetic components could be used in tandem with the bulk-micromachined and wafer-bonded silicon structures. Magnetic sensing/actuation schemes offer high energy density transduction over long coupling distances. Bulk-micromachining and wafer bonding offer highly three-dimensional silicon structures with stable and well-characterized mechanical properties.

However, to achieve truly integrated silicon-based magnetic devices, fabrication techniques must be developed to enable the magnetic materials to be embedded within bulk micromachined silicon. These processes are crucial to the development of the silicon-based microengine. In addition to merging fabrication technologies, the integrated magnetic components should be able to withstand sustained operation at elevated temperatures. Figure 1.4 shows a conceptual schematic of how two different magnetic machines, an induction machine and a PM machine, would be embedded in a multi-wafer silicon stack to form a microengine.

To achieve such unique and complicated structures, several novel fabrication methods are needed. First, methods for integrating thick electroplated metals into a multi-wafer fusion bonding process must be developed. The high temperatures required for bond annealing demand that oxidation, diffusion, thermal mismatch, and metallurgical/microstructural changes must all be addressed. In addition, almost all metals are incompatible with the standard RCA pre-bond cleaning process, so an alternative metal-compatible pre-clean needs to be identified. Second, the results from the first-generation induction machines [29-35] indicated that laminations are critical for maximum machine performance. Existing methods for microfabricating magnetic

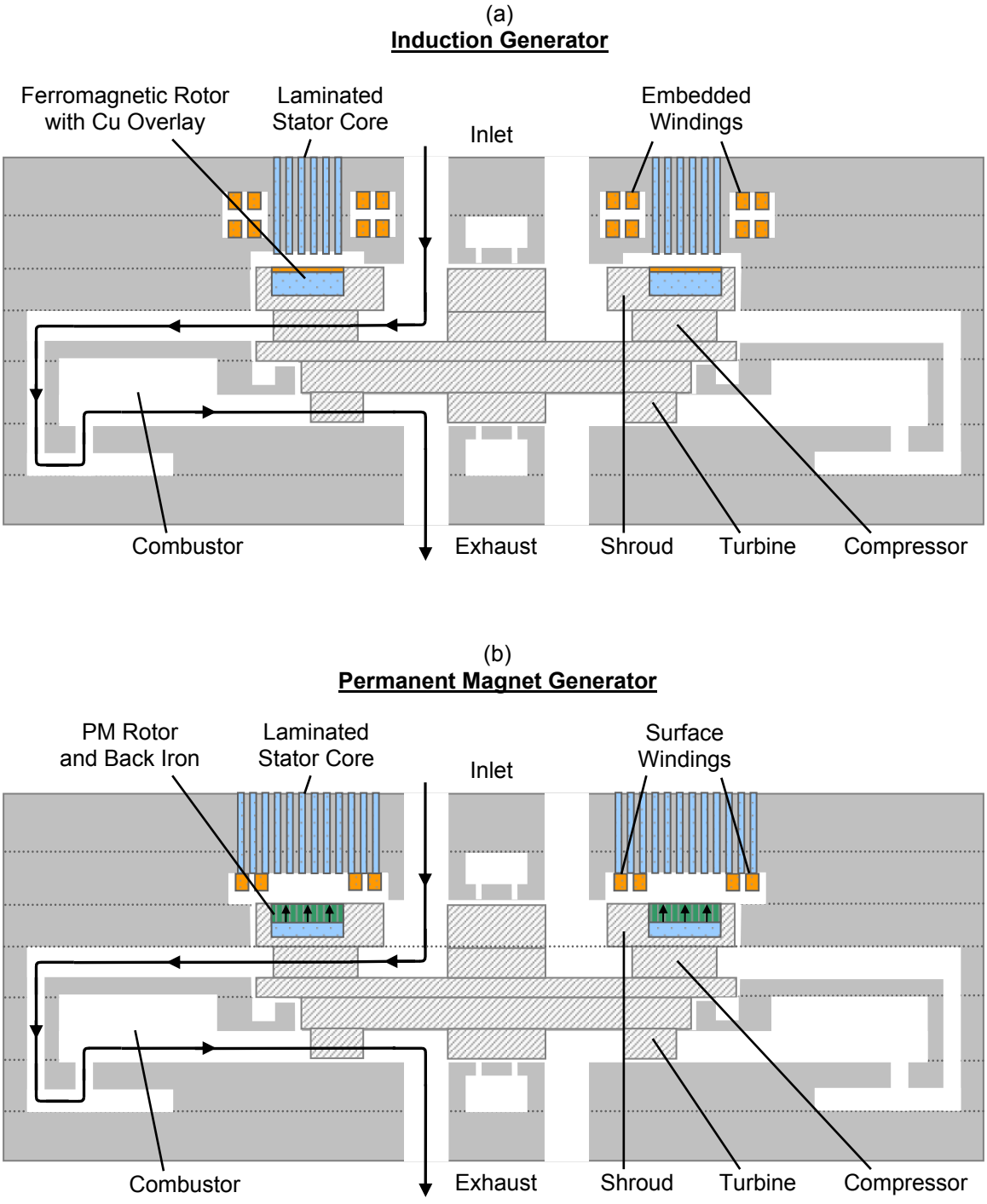

Figure 1.4. Conceptual diagrams of (a) magnetic induction and (b) permanent magnet generators embedded in a multi-wafer silicon microengine.

laminations are not suitable, so methods for achieving vertically laminated magnetic stator cores in silicon are required. Finally, a method must be developed for inlaying large volumes of magnetic materials in silicon to form the machine rotor. Novel fabrication approaches are discussed in Chapter 2 to meet each of these design challenges.

CHAPTER 2

FABRICATION PROCESS DEVELOPMENT

Several fabrication process technologies were developed and characterized to advance the development of silicon-based, magnetic micromachines.

2.1 Metals Embedded in Fusion-Bonded Silicon

In this section, fabrication methods are presented and verified for incorporating thick (tens or hundreds of microns) electroplated metals within fusion-bonded silicon, as shown in Figure 2.1. Electrodeposited Cu and NiFe are the two most popular materials for magnetic MEMS devices and thus were used to verify the process. Cu and $Ni_{80}Fe_{20}$ (Permalloy) test structures were embedded inside silicon wafers, which were subsequently fusion-bonded at 500°C for 4 hr with nearly 100% yield. Resistance tests validated the electrical integrity of the metals after annealing, and magnetic measurements indicated that NiFe maintained its magnetic performance after annealing. Additional mechanical tests verified a strong, uniform bond and that the presence of metal does not degrade the bond strength.

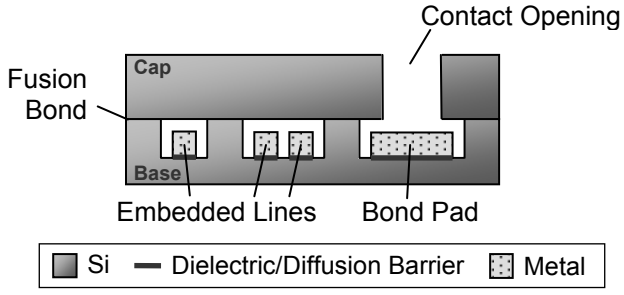

Figure 2.1. Schematic of metal structures embedded in fusion-bonded silicon, depicting single and double embedded lines and a bond pad with a contact opening.

2.1.1 Fabrication Development

Many initial and parallel experiments were performed to guide the development of a suitable fabrication sequence. The key results and lessons learned are discussed throughout.

Pre-bond Clean

The first objective was to identify a metal-compatible pre-bond cleaning sequence that provided a highly bondable surface without damaging or significantly etching the electroplated metal structures. The sequence used an organic clean, an oxide etch, and an "activation" step to hydrophilicize the silicon surface, as shown in Table 2.1. This process is similar to conventional pre-bond procedures based on the RCA clean, but the metallic ion clean (HCl-based SC2 bath) is omitted and the concentration of NH_4OH is reduced in the activation step to limit oxidation of the metals. Experiments showed that this sequence resulted in a small (<<1%) but measurable increase in the resistance of 35 μm thick electroplated Cu and NiFe test structures, which can be attributed to surface oxidation (oxidizing bath) and cross-sectional reduction (etching of the generated oxide by HF).

Table 2.1. Metal-compatible pre-bond cleaning procedures.

Step	**Chemicals**	**Temp. (°C)**	**Time (min)**
1. Organic Clean	1:1:5 NH_4OH:H_2O_2: H_2O	80	10
2. Oxide Etch	(1:6) BOE	25	2 -15*
3. Surface Activation	0.25:1:5 NH_4OH:H_2O_2: H_2O	80	10

*Oxide etch time depends on thickness of oxide; the etch was stopped immediately after all oxide was removed

Thermal Limits

Next, experiments were performed to explore the thermal limits of the metals during wafer-bond annealing. If Cu were used as a conductor in a magnetic device, it would typically be dielectrically isolated from the Si substrate by an SiO_2 layer. Diffusion of Cu was considered a crucial factor, as it is known that Cu readily reacts with Si and SiO_2 to form silicide compounds at temperatures as low as 200°C [63]. Inter-diffusion between the Cu and Si substrate would cause electrical shorts and could not be tolerated. Comprehensive reviews of diffusion barriers between Cu and Si/SiO_2 can be found in [64] and [65]. Ta was selected as a suitable diffusion barrier for its ease of deposition, good adhesion, and reported thin-film diffusion protection up to 650°C [63]. In the case of NiFe, inter-diffusion and interfacial silicide formation were not considered as crucial, as long as the bulk material retained its magnetic properties. These interfacial effects could be tolerated because magnetic isolation would be maintained even if the structure was electrically shorted to the substrate. Therefore, a thin Cr adhesion layer was used instead of Ta for the NiFe structures.

Measurements were made on electroplated Cu four-point resistive test structures on flat silicon wafers before and after annealing to emulate the fusion-bonding process and determine the survivability of the metal structures. The structures were very similar to the embedded test structures that will be described in detail later. Electroplated Cu lines 30-100 μm wide and 35 μm thick were patterned on a 300 nm DC-sputtered Ta diffusion barrier on top of either a 200 nm dry thermal oxide or a 1 μm wet thermal oxide. Figure 2.2 shows the average resistance change after annealing in nitrogen for 1 hr at temperatures from 500-1000ºC. The structures exhibited good adhesion and a slight decrease in resistance when annealed up to 900ºC, with no appreciable difference

between the two oxides. The decrease in resistance can be attributed to microstructural changes, specifically grain growth and reduction of intergranular defects, as described in [66]. Above 900ºC, the copper failed catastrophically, and energy-dispersive X-ray spectroscopy (EDS) analysis revealed the formation of Cu-Si compounds, indicative of diffusion barrier failure. While the nature of the Cu-Ta-Si interfaces and failure mechanism were not fully explored, these temperatures are higher than the 650ºC limit previously reported for thin films of Cu [63-65]. These results demonstrated that Cu could survive the high temperatures for wafer-bond annealing.

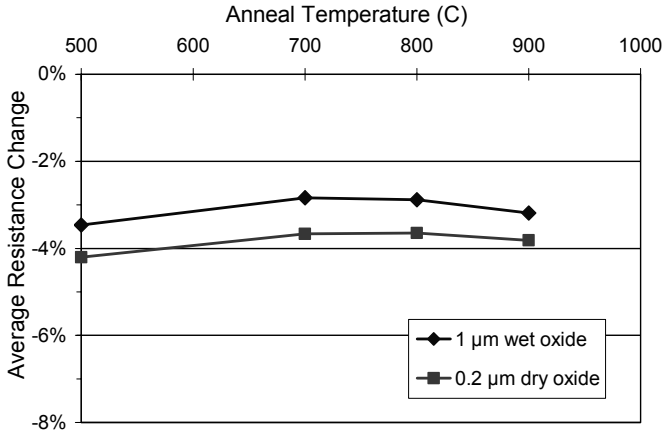

Figure 2.2. Resistance change of electroplated Cu test structures on oxidized silicon wafers using 300 nm Ta diffusion barrier after annealing in nitrogen for 1 hr.

Embedded Metal Process

The next step was to develop a fabrication process for embedding metals within cavities in fusion-bonded silicon. The primary focus was to maintain a pristine silicon bonding surface during all processing before fusion bonding. As a result, fabrication approaches that required polishing of the bonding surfaces were not considered, as the

surface roughness and cleanliness are the most important factors for reliable bonds [48]. Two complementary methods were proposed, as shown in Figure 2.3. In Method 1, a flat base wafer is electroplated with metal, and another cap wafer with corresponding cavities is bonded around the metal structures. In Method 2, metal is patterned in pre-etched cavities in the base wafer, and a flat cap wafer is bonded to seal the metals inside.

The conceptual fabrication sequence begins by growing a thermal oxide on a flat or pre-etched base silicon wafer. This oxide serves as an electrical insulator for the electroplated metal and as a sacrificial protective layer [21] for the nonplated areas, which will later become bonding surfaces. A diffusion/adhesion layer and seed layer are sputtered across the entire wafer. The diffusion barrier prevents interaction of the plated metal with the silicon, and the seed layer ensures a highly conductive surface to initiate the electrodeposition. Thick photoresist is then patterned to define an electroplating mold. In the case of the pre-etched wafers, the pattern is defined down into the trench to prevent electrodeposition on the side walls and overgrowth protrusions that would require polishing. Next, metal is electroplated to the desired thickness and the mold is stripped. The thin films in the nonplated areas are then wet-etched back down to the silicon surface. The cap wafer is prepared separately by etching cavities and/or contact holes in the appropriate locations. Both wafers are then cleaned, aligned, bonded, and annealed. The seed, diffusion layers, etch chemistries, and details of the processing steps for Cu and NiFe will be discussed, but the general procedure is applicable to a variety of electroplated materials.

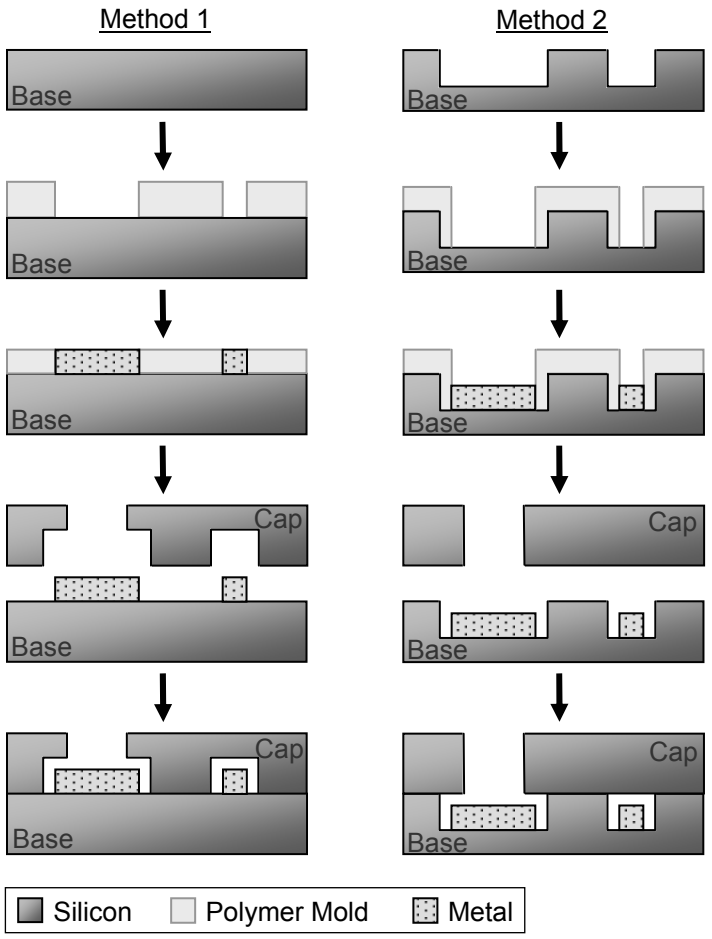

Figure 2.3. Two alternative fabrication methods for embedding metal in wafer bonded silicon, depicting an embedded line and bond pad with contact opening. Note diffusion, seed, and oxide thin-film layers are not shown.

There are advantages and disadvantages to each method. The challenge for Method 2 is the micromolding and electroplating in cavities in the base wafer. However, Method 2 does not require an aligned wafer bond (requiring specialized equipment) or a double etch of the cap wafer, as compared to Method 1. Method 2 is also more easily integrated with commonly used wafer-bonded structures, and for these reasons, it was selected as the primary method for investigation.

To achieve structures that are fully recessed in the base wafer using Method 2, a polymer plating mold needed to be patterned within the confines of the cavities. The mold was designed to leave a gap between the metal and the Si sidewall. This helped to reduce thermal stresses and eliminate diffusion barrier failures resulting from defects in the rough sidewall. The resulting "bottom-up" plating also enhanced uniformity and prevented metal from protruding from the cavity. Futurrex NR9-8000P (Franklin, NJ) high aspect ratio negative photoresist was used. A gradient in the exposure dose results in high cross-linking of the upper surface but low cross-linking deep in the trench. This can lead to cracking at the top surface and/or undercutting deep in the trench during development, as shown in Figure 2.4. The subsequent protrusions can inhibit bonding and the sidewall contact in the trench can result in diffusion barrier failures. These defects were eliminated by maintaining a sidewall gap of at least 1/3 the trench depth (e.g., 50 μm gap for 150 μm deep cavity) for cavities up to 150 μm deep. SU-8 photosensitive epoxy (Microchem, Newton, MA) was also investigated, but the difficulty of removal precluded its use.

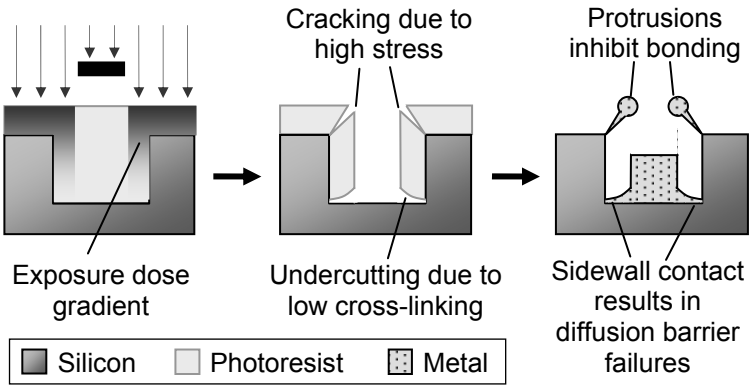

Figure 2.4. Schematic depicting two unwanted mold defects when trying to minimize sidewall gap using negative photoresist.

2.1.2 Test Structure Fabrication

For verification of this fabrication approach, embedded Cu and NiFe test structures were fabricated using Method 2, described above. Masks were designed with a variety of test structures, which were dimensioned to fit inside cavities, as shown in Figure 2.5a. These patterns were used to explore the electrical and magnetic properties of the Cu and NiFe after various processing steps. The majority of the structures had four 2 x 2 mm bond pads and interconnecting lines of various widths (w_c = 100-320 μm) with various sidewall gaps (g = 10-60 μm), forming a four-point resistance test structure with an active length of 4 mm, as shown in Figure 2.5b. Some others contained pairs of lines separated by various distances (d = 40-60 μm) for testing the isolation between two parallel conductors, as shown in Figure 2.5c. Others had only bond pads (no interconnecting lines) and were used for magnetic characterization. Half of the structures had contact openings for access to the bond pads, while the others were completely sealed for mechanical tensile testing.

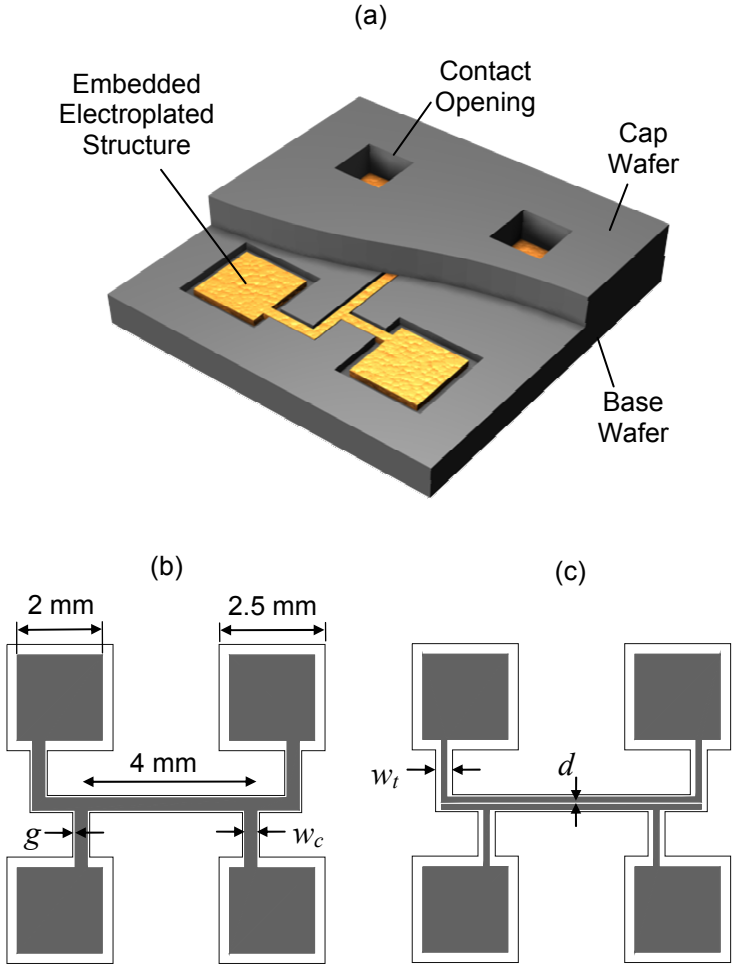

Figure 2.5. (a) Rendering of embedded test structure with a cutaway of cap wafer. The accompanying mask patterns for (b) four-point resistive test structure and (c) parallel line test structure are also shown. The variable parameters in the mask set were the conductor width, w_c = 100-320 μm, trench width, w_t = 100-400 μm, sidewall gap, g = 10-60 μm, and parallel line gap, d = 40-60 μm.

Both the Cu and NiFe test structures were prepared using standard 100-mm diameter, p-type (1-10 Ω·cm), <100> silicon wafers. Figure 2.6 shows the fabrication sequence for patterning electroplated metal in cavities on the base wafer and bonding a cap wafer over the cavities. The processes for forming the Cu and NiFe test structures were almost identical, so variations for the NiFe wafer are denoted in brackets.

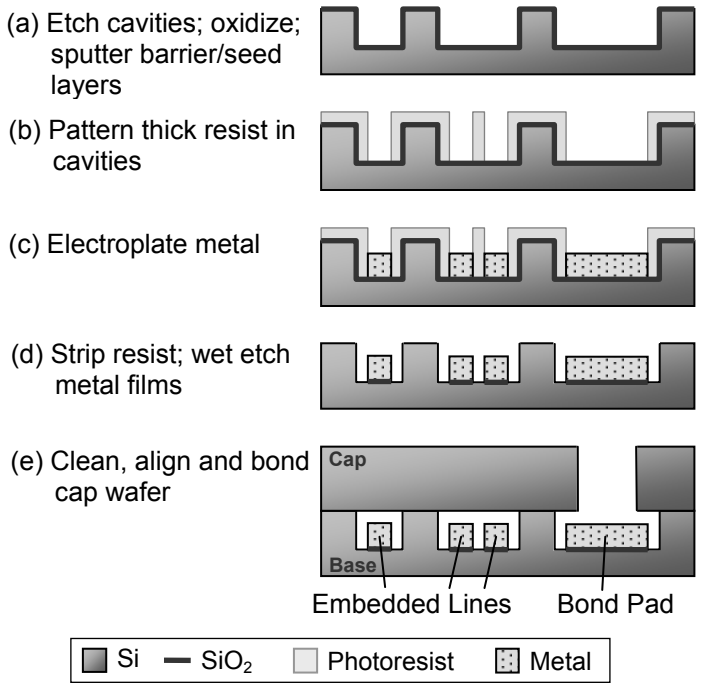

Figure 2.6. Fabrication sequence for embedding electroplated metal in base wafer and encapsulating with cap wafer, depicting examples of single and double embedded lines and a bond pad with a contact opening.

The sequence began by growing a 0.2 μm dry oxide on the base and cap wafers. This oxide served as a protective layer during all future processing. Clariant AZ4620 photoresist (Somerville, NJ) was then used as a DRIE mask to form the cavities and contact holes on the base and cap wafers, respectively. The oxide and silicon were etched, forming 75 μm deep cavities in the base wafer and 500 μm deep through-holes in

the cap wafer. A post-DRIE piranha clean was performed on both wafers, and the cap wafer set aside.

For the base wafer, a 1 μm wet thermal oxide was grown, followed by blanket DC sputtering of a 400 nm Ta diffusion barrier {30 nm Cr adhesion layer}, 200 nm Cu seed layer, and 30 nm Ti adhesion layer (Figure 2.6a). The Ta {Cr} layer limited diffusion and enhanced adhesion, the Cu layer provided a conductive seed layer for electrodeposition, and the upper Ti layer improved adhesion for the subsequent photoresist mold. Next, Futurrex NR9-8000P (Franklin, NJ) negative photoresist was patterned to define the electroplating mold within the confines of the cavities (Figure 2.6b). The limitations of this method were previously discussed. Then, after a brief dip in diluted HF to remove the Ti layer, Cu {NiFe} was electroplated 35 μm thick (Figure 2.6c) using standard electroplating baths, as listed in Appendix A.

After plating, the resist molds were stripped using Futurrex RR4 (Franklin, NJ). The stripper consistently had a difficult time stripping the samples that had been in the NiFe bath, and additional ultrasonic agitation and oxygen plasma treatment were necessary to remove all of the residues. The thin-film Ti, Cu, and Ta {Cr} layers were then selectively wet etched back down to the SiO_2 layer (Figure 2.6d). Wet etching was preferred over dry etching to prevent particle contamination and micromasking, sometimes encountered when using plasma etching tools. The Ti layer was removed using 1:20 HF:H_2O for ~30 s, and the Cu seed was removed using "blue etch" (NH_4OH saturated with $CuSO_4$) for ~5 min. A wet etch was developed and characterized for the Ta that proved to be quite slow, but sufficiently selective: a 1:1 mixture of H_2O_2:EDTA (1M) was used at 60°C for ~3.5 hr. {For the NiFe samples, the Cr was removed using a

standard chromium etchant (Cyantek, Freemont, CA).} At this point, only the Cu {NiFe} test structures remained on the SiO_2 layer. Figure 2.7 shows an example of the resulting structure recessed in a silicon trench.

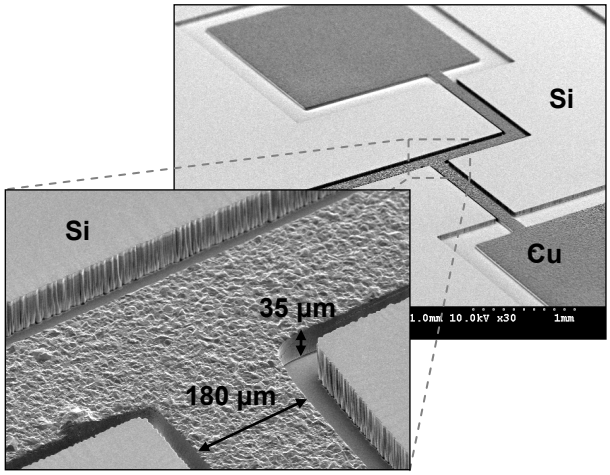

Figure 2.7. SEM of electroplated Cu test structure recessed in a Si cavity before bonding.

Next, both the base and cap wafers were prepared for bonding using the methods outlined in Table 2.1. The cap and base wafers were then aligned by hand and contacted at room temperature (Figure 2.6e). The bonded pair was inspected using infrared (IR) transmission imaging and typically indicated >90% bonded area with void regions near the edges of the wafers. Finally, the wafers were annealed using a wafer bonder (Suss Microtec, Germany) at 500°C for 4 hr in vacuum ($<2 \times 10^{-6}$ torr) with 200 kPa clamping pressure. Figure 2.8 shows cross-sections of embedded Cu lines after annealing. Post-bond IR imaging indicated the bond area had typically increased to nearly 100%, as shown in Figure 2.9a.

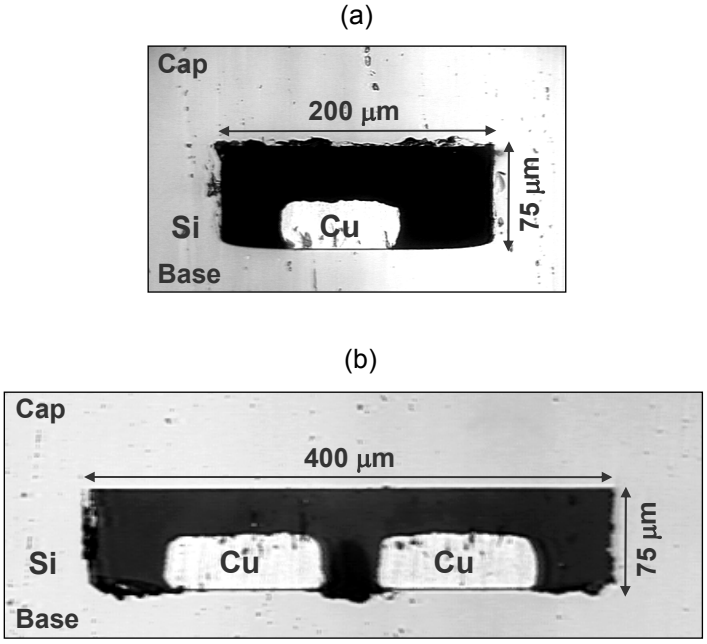

Figure 2.8. Cross-sections of Cu structures embedded in Si after bonding at 500°C for 4 hr: (a) single buried line; (b) double buried lines. Chipping of the silicon is from dicing/polishing.

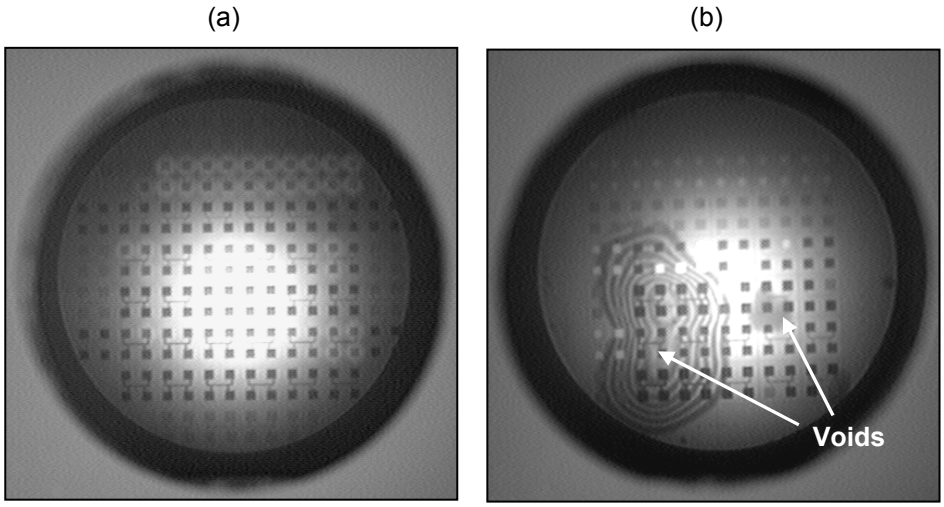

Figure 2.9. Typical post-anneal infrared transmission images of bonded pairs after annealing in (a) wafer bonder (~100% bonded area), and (b) tube furnace (<60% bonded area).

It should be noted that initial attempts for bonding were made in a tube furnace at temperatures up to 900°C for 1 hr under pure N_2 or 4% H_2 / 96% N_2 forming gas, but the bond yield was usually unacceptably low (<60% bonded area), as shown in Figure 2.9b. This could have been due to thermally induced stresses and/or outgassing from the electroplated structures. Switching to the wafer-bonding system offered a vacuum environment and the use of a physical clamping force. This system improved the bond yield, but limited the temperature to 500°C. During all low-temperature bonding, no bubble voids were observed, as have been reported in other studies [50-53]. The presence of the etched cavities may act to getter any gases released from the bond interface during annealing [50].

2.1.3 Electrical Tests

The resistances of the test structures were measured before and after bond annealing using a four-point resistance measurement at 1 A, as shown in Figure 2.10a. Immediately after contacting, the average resistivities of the Cu and NiFe were 1.79±0.40 μΩ·cm and 14.8±3.6 μΩ·cm, respectively. After bonding at 500°C for 4 hr, an average resistance reduction of 2.6% for the Cu and 23% for the NiFe was measured, as shown in Figure 2.10b. The resistance drop corresponds to post-bond resistivities of 1.75±0.39 μΩ·cm and 11.4±2.8 μΩ·cm for Cu and NiFe, respectively.

The slight decrease in the Cu resistance was similar to the previously discussed results for the non-embedded test structures, and attributed to grain growth and a reduction of intergranular defects [66]. The much larger decrease in the NiFe resistance is consistent with other studies in the literature. Electrodeposited NiFe (Permalloy) exhibits a transition region at ~350-400°C, where gross recrystallization and significant

grain growth occurs, resulting in deterioration in the film resistivity (>20% change) and magnetic properties [67], as will be discussed later.

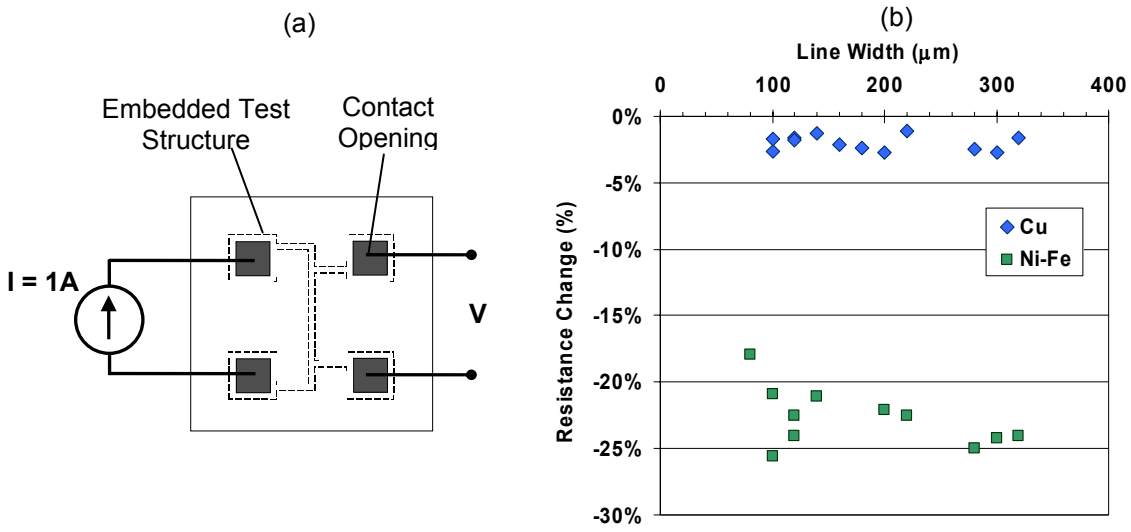

Figure 2.10. (a) Four-point resistance measurement of embedded test structure, using a 1 A DC current. (b) DC resistance change of embedded Cu and NiFe of various line widths after bonding (500°C, 4 hr in vacuum).

Additional measurements were performed using the parallel-line test structures to determine if the metals were dielectrically isolated from the substrate and each other both before and after annealing. Any dielectric failure (e.g. pinhole defects, diffusion barrier failure) could be detected by a resistance measurement between the two adjacent lines after annealing. The Cu structures showed a resistance above the limits of the meter used for testing (>20 MΩ) before and after annealing, verifying dielectric isolation and proving the effectiveness of the Ta diffusion barrier. On the other hand, the NiFe parallel lines showed a short circuit (2-10 Ω) through the substrate, indicative of diffusion through the dielectric layer. This was not entirely unexpected, as no diffusion barrier was used (only a Cu adhesion layer), and not necessarily a problem since the NiFe would not

necessarily need to be dielectrically isolated from the substrate. It should also be noted that this short to the silicon would not significantly affect the previously discussed resistance measurements, as the resistivity of the silicon was ~10^5 larger than the metal.

Lastly, the Cu test structures were tested at high currents to verify the current capacity. A DC current of up to 10 A, the maximum output current of the power supplied used, was passed through a test structure line with a cross-section of 40 μm x 40 μm for a period of several minutes. This corresponded to a current density of >6 x 10^9 A/m^2 and resulted in an oxidation of the surface of the Cu and heating of the wafer to >100°C. However, subsequent microscopic inspection indicated the Cu structure remained in good condition. This experiment verified the ability for the embedded Cu lines to sustain high current densities, as needed for implementation in a magnetic machine.

2.1.4 Magnetic Tests

To verify that the NiFe material could survive the wafer bond annealing, magnetization measurements were performed using a Lake Shore Model 7300 (Westerville, OH) vibrating sample magnetometer (VSM) on 2 mm x 2 mm square pads of NiFe before and after annealing at 500°C for 4 hr. The results, shown in Figure 2.11, indicate a negligible difference in magnetic saturation, but a substantial rise in coercivity from 0.47 Oe (37.4 A/m) to 3.55 Oe (382.6 A/m). As discussed earlier, this effect is attributed to the recrystallization and grain growth of the NiFe during the bond annealing, and consistent with the ~10x increase reported in [67]. The increased coercivity results in larger hysteresis losses in a magnetic device and must be considered in the overall design. However, in many cases, hysteresis is only a minor fraction of the total magnetic

loss, so the overall degradation in performance may be small. Thus, these experiments verify that survivability of the NiFe as an embedded magnetic material.

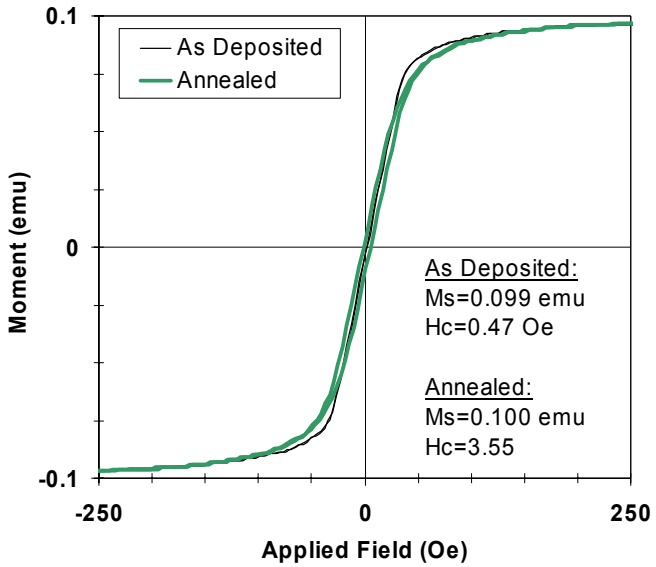

Figure 2.11. Magnetization curves for NiFe before and after annealing (500°C, 4 hr in vacuum).

2.1.5 Mechanical Tests

Finally, tensile failure tests [49] were conducted to measure the bond strength and, more importantly, to verify that the presence of the electroplated metal did not adversely affect the bond strength. The test structures with embedded metals and no contact openings were used for these measurements. After bonding at 500°C for 4 hr, the wafers were diced into 1 cm x 1 cm test samples of three different types: cavities with Cu, cavities with NiFe, and empty cavities. The bonded samples were mounted to steel block test fixtures using cyanoacrylate adhesive and tensile loads were applied using an MTS (Eden Prairie, MN) loading frame, as shown in Figure 2.12a. The debonding failure

force was measured and then divided by the contacted surface area (contacted surface area, excluding cavities) to determine the bond strength.

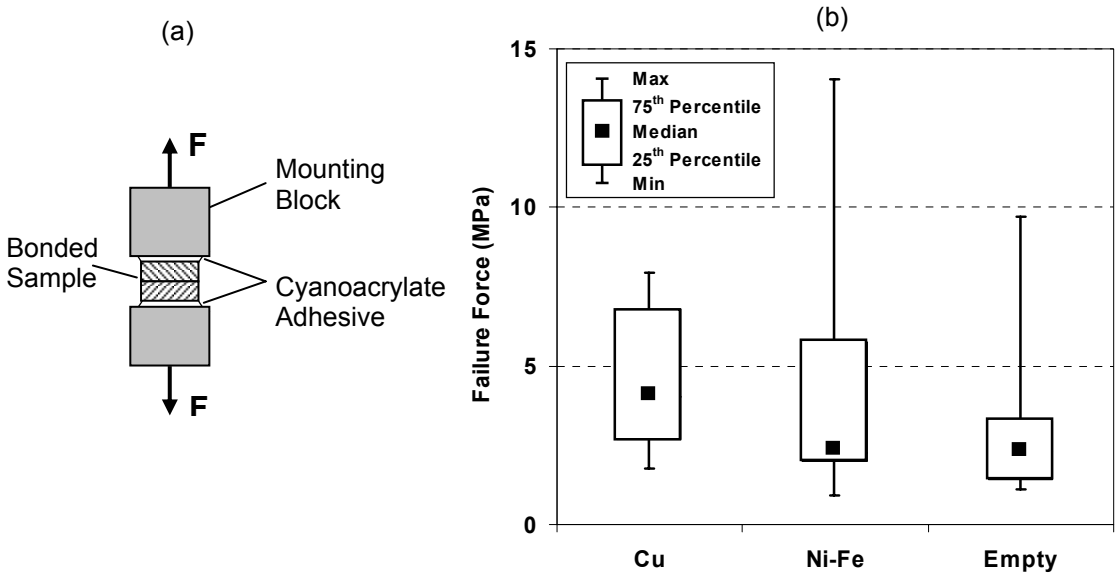

Figure 2.12. (a) Method for tensile testing wafer bonded pairs, depicting the bonded sample mounted to the mounting blocks with cyanoacrylate. (b) Failure forces for bonded samples with embedded Cu or NiFe compared to bonded samples with empty cavities (500°C, 4 hr in vacuum).

This mode of bond strength testing has large statistical deviations because of the unstable modes of failure. To best show the variation in the data, the measured bond strengths are shown in quartile format in Figure 2.12b. The mean values (not shown) were 4.6 MPa, 4.6 MPa, and 3.2 MPa for the Cu, NiFe, and empty cavities, respectively. Even with the large variations, it is evident that the presence of Cu or NiFe does not reduce the bond strength. Other tests performed early in the development showed average bond strengths of 12.2 MPa could be achieved by bonding at 900°C for 1 hr. However, as stated previously, the yield was quite low because of bond voids and diffusion barrier failures.

Previous investigators report a wide spread of Si-Si bond strengths from tensile failure tests: [49] reported 12-21 MPa after 1 hr at 120-400°C and [53] reported an average of 17 MPa after 4 hr at 200°C, while [51] reported a maximum of 4.25 MPa after several hours at 1000°C. The measured bond strengths of the test samples are on the low side when compared to these previous results, but unaccounted for stress concentrations in the non-uniform cross-section may be artificially lowering the "apparent" interfacial force. Nevertheless, the devices could be diced and handled without debonding, and Figure 2.13 shows further evidence of a strong, uniform bond. Examination of the bond interface after tensile failure reveals fracture in the bulk silicon, rather than interfacial delamination.

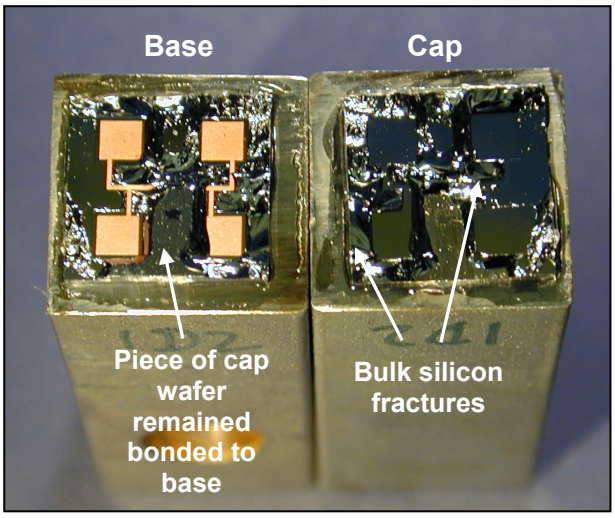

Figure 2.13. Photograph of base and cap samples on mounting blocks after tensile failure testing. General silicon fractures are evident and a piece of the cap is seen still bonded to the base, indicating a strong bond.

These tests demonstrate a successful fabrication process for embedding thick electroplated metallic materials in fusion-bonded silicon. The results show that

embedded Cu and NiFe test structures sustain the high temperatures required for bond annealing, and the Si-Si bond strength was unaffected by the presence of the plated materials. These fabrication methods are compatible with a variety of electroplated materials and will be applied for the development of the Si-based magnetic machines.

2.2 Vertically Laminated Magnetic Cores in Silicon

This section presents two fabrication methods developed to enable vertically laminated magnetic core structures within silicon, as shown in Figure 2.14. Both methods rely on through etching a silicon wafer and then electrodepositing ferromagnetic material. The first, more novel approach relies on direct electrodeposition onto the sidewalls of highly conductive silicon. The second, more direct approach uses oxidized silicon as a mold for electrodeposition from a separate seed wafer. Both methods provide the following advantages over previously reported approaches [58-62]:

- Cores of large total thickness having micron-scale laminations, achieved in a single electrodeposition step
- Vertically laminated structures, permitting magnetic flux to pass both in-plane and out-of-plane
- Integrability of cores with other microfabricated structures
- High-temperature compatible structures

In addition to presenting and verifying these fabrication methods, a mathematical framework is presented for determining the optimal lamination geometry for a particular application, based on certain fabrication constraints.

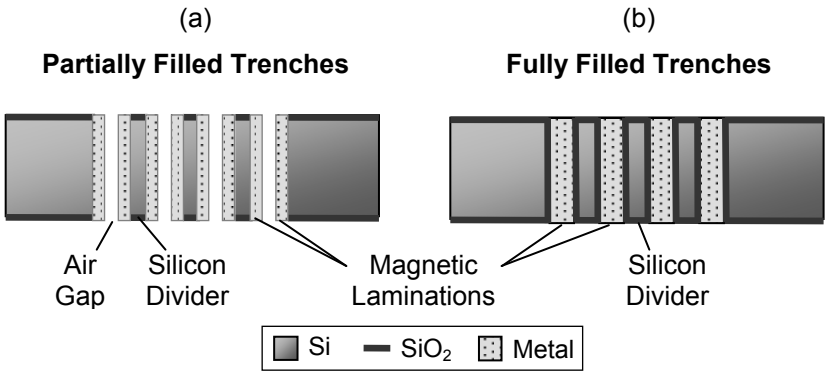

Figure 2.14. Schematic of vertically laminated cores in silicon achieved using (a) partially filled trenches and (b) fully filled trenches.

2.2.1 Partially Filled Trench Method

Fabrication

Laminated magnetic cores were built by directly plating NiFe onto the sidewalls of vertically etched trenches, as shown in Figure 2.15. Low-resistivity (0.001 Ω·cm), 525-μm thick, 100-mm diameter, n-type, <100> silicon wafers were used. The fabrication process began by growing a 200 nm dry thermal oxide, which later prevented electrodeposition on the top and bottom wafer surfaces (Figure 2.15a). Next, AZ4620 photoresist (Clariant, Muttenz, Switzerland) was patterned as a mask for etching trenches in the oxide and silicon using DRIE. The through etch was achieved by etching half way from the top of the wafer (Figure 2.15b) and then etching the remainder from the bottom side (Figure 2.15c). The photoresist was then stripped, and the wafer was cleaned in "piranha etch" (3:1 H_2SO_4:H_20_2, 120°C) for 10 min. A brief HF dip was used to remove the native oxide on the silicon sidewalls immediately before electroplating. A standard NiFe bath, listed in Appendix A, was used with two nickel anodes placed approximately 3 cm from each face of the sample. The low-resistivity silicon provided a conduction

path for electrodeposition, and the magnetic material was deposited only on the etched silicon sidewalls to a thickness such that an air gap remained between adjacent laminations (Figure 2.15d).

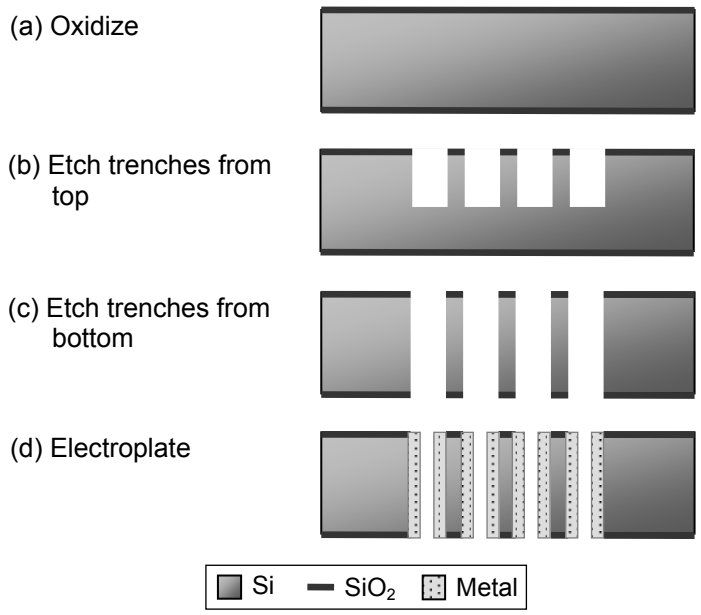

Figure 2.15. Simplified process flow for vertically laminated cores using partially filled trench method.

Using this technique, a variety of vertically laminated cores were produced with overall dimensions of 1 mm wide x 4 mm long x 0.525 mm thick, as shown in Figure 2.16. To explore the fabrication limits and the effectiveness of eddy current reduction, the lamination geometries were varied as shown in Table 2.2. Figure 2.17 shows optical images of cross-sections of several plated NiFe structures.

Table 2.2. Range of fabricated lamination geometries.

Parameter	Range
w_{etch}	60-180 μm
w_{div}	20-50 μm
w_{lam}	3-53 μm
w_{air}	53-163 μm

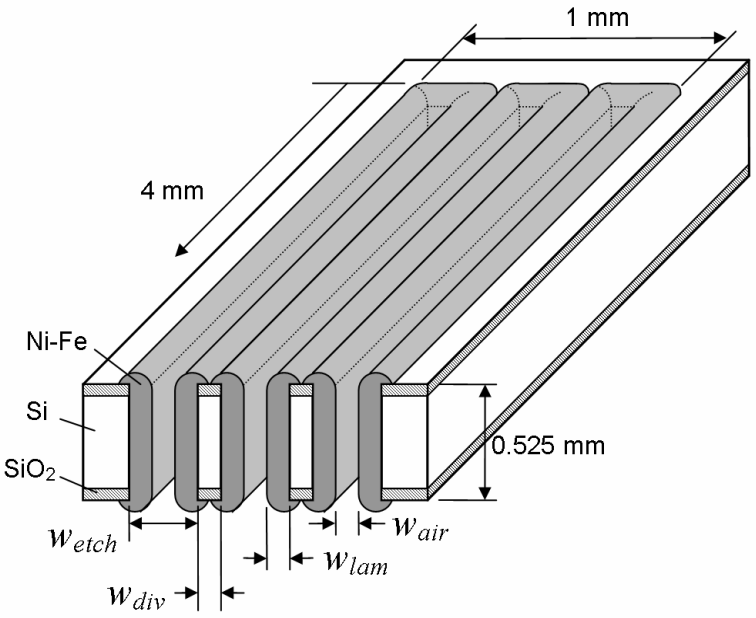

Figure 2.16. Schematic of vertically laminated core. For illustration, $w_{etch} = 3w_{div} = 3w_{lam} = 3w_{air}$, depicting a packing density of $\alpha = 0.5$.

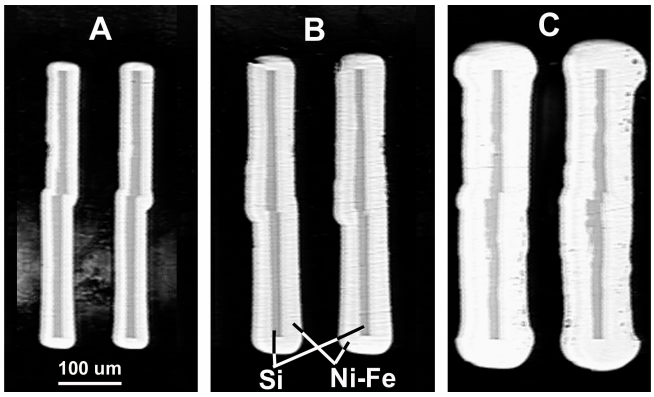

Figure 2.17. Optical images showing partial cross-sections of laminated NiFe structures with different w_{lam} (A = 23 μm, B = 38 μm, and C = 53 μm). Some misalignment is noted between the top- and bottom-side etch.

The silicon divider width, w_{div}, was limited to ~20 μm by deep silicon etching technology. Reliably creating much smaller Si dividers presented a substantial fabrication challenge (particularly when front-to-back alignment is used to etch from both sides). No change in plating uniformity was noted for the different silicon divider widths, so only the cores with 20 μm dividers (highest packing density) were used for testing.

The air gap, w_{air}, was limited by electrodeposition non-uniformities caused by current crowding effects and restricted ion transport as the gap between the advancing plated layers is reduced [68]. This resulted in a deposit that tended to "pinch" or "key-hole," leaving a void in the center region. Pinching was limited by stopping the plating at the onset of non-uniform deposition, as indicated in Figure 2.17c. For silicon trenches of all widths, it was found empirically that the minimum air gap was approximately equal to the lamination thickness ($w_{air} \approx w_{lam}$). Even with these fabrication constraints, packing densities in excess of 50% were achieved.

Characterization

To verify that the vertically laminated NiFe cores were effective in reducing eddy current losses, the impedances of the various laminated cores were measured from 10 kHz - 40 MHz. The theoretical frequency dependence of the inductance of a laminated core due to eddy current losses is given by [69]

$$L(f) = L_0 \beta(n) = L_0 \frac{1}{n} \frac{\sinh n + \sin n}{\cosh n + \cos n}, \tag{2.1}$$

where L_0 is the low-frequency (DC) inductance and $\beta(n)$ is a shaping function. The frequency-dependent argument, denoted as the lamination ratio, n, is given by

$$n = \frac{w_{lam}}{\delta} = w_{lam} \sqrt{\frac{\pi f \mu_0 \mu_r}{\rho}}. \tag{2.2}$$

Here, w_{lam} is the lamination width, δ is the skin depth, μ_0 is the permeability of free space, μ_r is the relative permeability of NiFe, ρ is the resistivity of NiFe (15 μΩ·cm), and f is the frequency. The cutoff frequency, f_c, is defined as the frequency when $w_{lam} = \delta$, or equivalently, $n = 1$. Therefore,

$$f_c = \frac{1}{w_{lam}^2 \mu_0 \mu_r \sigma \pi} \tag{2.3}$$

and $L(f_c) = 0.968\, L_0$.

Measurements were made using a 27-turn, 3.5 mm long, 2 mm diameter solenoid coil connected to an HP4194A impedance analyzer (Agilent, Palo Alto, CA). The various laminated core structures were inserted into the coil, as shown in Figure 2.18, and the inductance was measured as a function of frequency. For analysis, the inductance of the coil with no core present (air core) was subtracted from the inductance of the coil with the magnetic core. This permitted analysis of the inductance contribution from only the magnetic core. Also, the silicon skeleton of the core was assumed to have a permeability of unity and no eddy current losses, because the dimensions of the silicon were smaller than the skin depth, even at 40 MHz (δ_{Si} = 250 μm).

Figure 2.19 shows the inductance of three samples (shown in Figure 2.17) with different lamination thickness (and packing density). The sample with the thickest laminations has the largest low-frequency inductance, L_0, but the lowest cutoff frequency, f_c. Figure 2.20 shows the cutoff frequencies plotted versus lamination thickness, along with several theoretical curves using Equation 2.3 (assuming constant permeability). As predicted, the cutoff frequency decreases with increasing lamination thickness, confirming that the laminating scheme is effective in reducing eddy current losses.

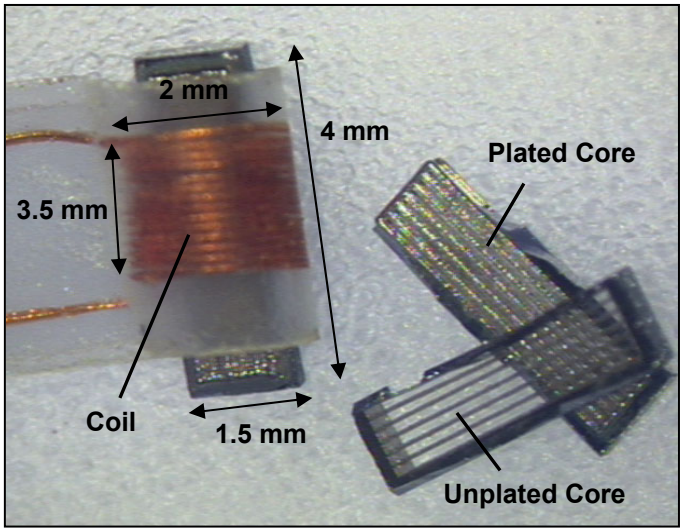

Figure 2.18. Coil and example cores used for impedance measurements.

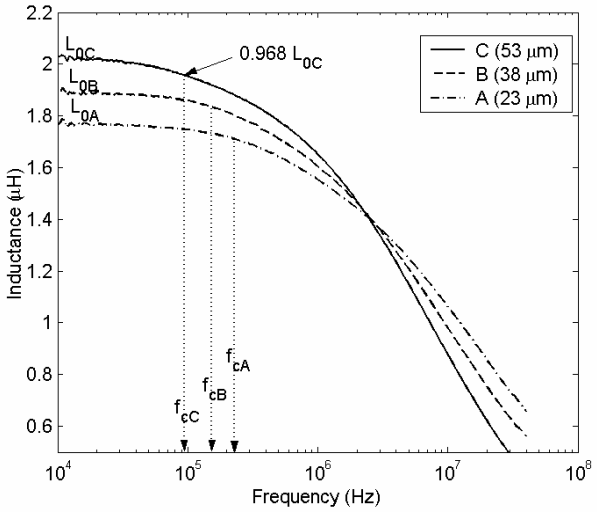

Figure 2.19. Inductance vs. frequency for three samples (shown in Figure 2.17) of increasing lamination thickness (and increasing packing density). The key parameters for each curve are the low-frequency (DC) inductance, L_0, and cutoff frequency, f_c.

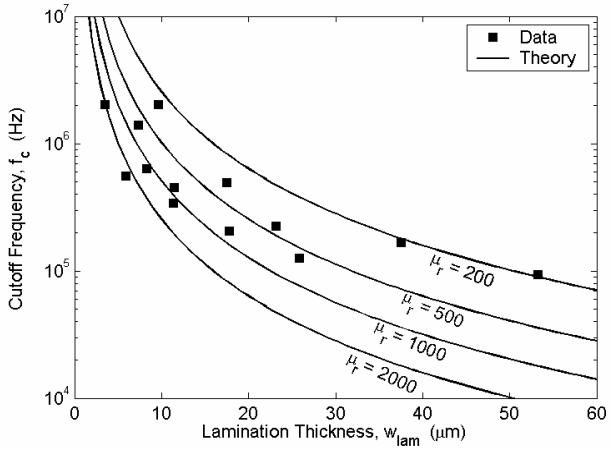

Figure 2.20. The measured cutoff frequencies, f_c, decrease with lamination thickness, w_{lam}. Theoretical cutoff frequencies (assuming constant relative permeabilities) are shown for reference.

Finally, several laminated samples were annealed at 500°C for 4 hr in vacuum to simulate a wafer bonding step. The samples survived with no apparent cracking or physical damage. This indicates that the laminated structure can withstand fusion bonding temperatures, despite the coefficient of thermal expansion mismatch between the NiFe and Si.

2.2.2 Fully Filled Trench Method

Fabrication

The second method for achieving vertically laminated cores takes a more conventional approach. Oxidized silicon takes the form of a mold, and NiFe is electroplated up from a seed wafer, which is temporarily bonded to the substrate using photoresist, as shown in Figure 2.21. Here, 500-μm thick, 100-mm diameter, p-type (1-10 Ω·cm), <100> silicon wafers were used. The fabrication process began by through etching the wafer using a Clariant AZ4620 (Muttenz, Switzerland) photoresist mask. For this step, etching could be performed from one or both sides. After stripping the

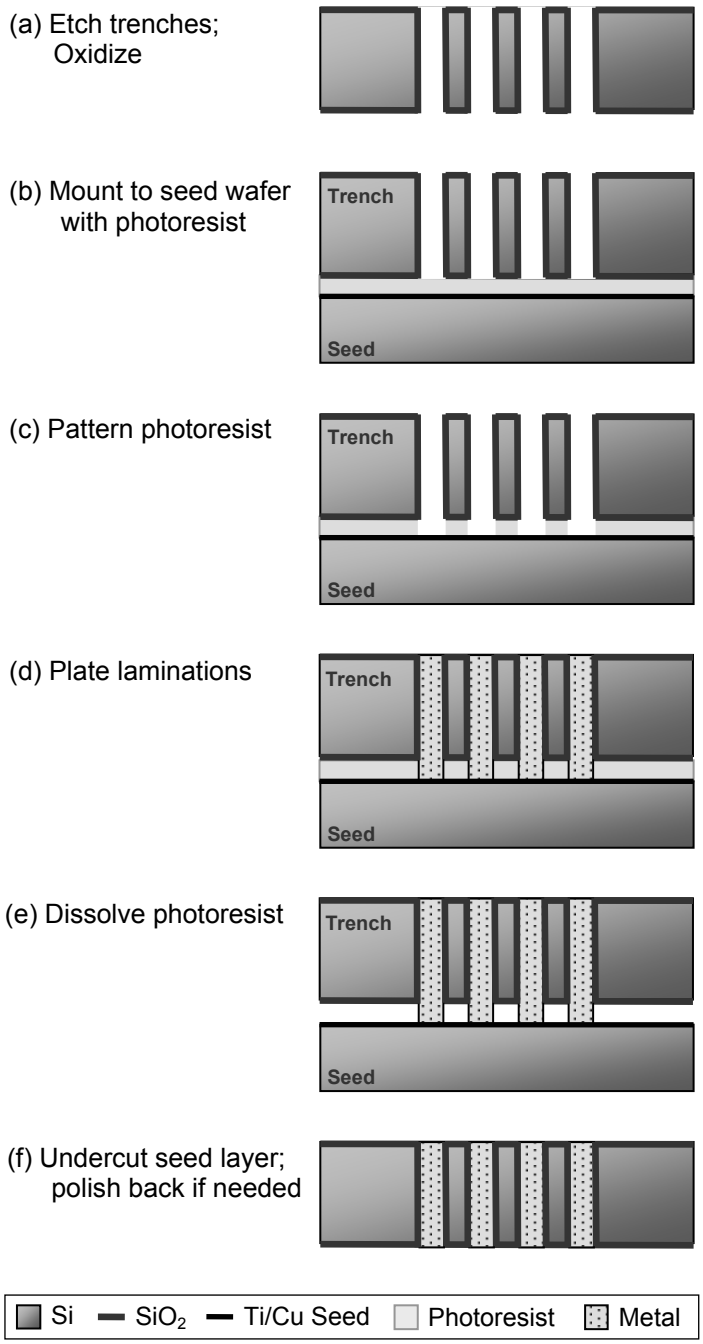

Figure 2.21. Process flow for vertically laminated cores using fully filled trench method.

photoresist, the wafer was cleaned in "piranha etch" (3:1 H_2SO_4:H_20_2, 120°C) for 10 min. Then a 1 μm wet oxide was grown to dielectrically isolate all surfaces of the silicon (Figure 2.21a).

Next, a separate "seed wafer" with a sputtered Ti (20 nm) / Cu (200 nm) seed layer was bonded to the etched wafer using photoresist. A ~2 μm layer of Shipley (Marlborough, Massachusetts) S1813 photoresist was spun and the etched wafer was pressed onto the seed wafer (Figure 2.21b). Following a 3 min, 100°C bake, the intermediate photoresist layer was patterned using the etched wafer as mask. This removed all of the resist from the base of the trenches, selectively exposing the seed layer (Figure 2.21c). A standard NiFe bath, listed in Appendix A, was then used to electroplate material up in the trenches (Figure 2.21d). Once finished plating, the photoresist bonding layer was dissolved (Figure 2.21e), and a selective Cu etch was used to undercut the electroplated structures, releasing the plated wafer from the seed wafer (Figure 2.21f). Any protrusions of metal could be polished down flush to the surface if needed.

Laminated NiFe samples were fabricated using this fully filled method, with variations of $w_{etch} = w_{lam}$ = 60-180 μm and w_{div} = 20-50 μm. Several examples are shown in Figure 2.22, indicating good uniformity. For this process, both the minimum lamination width and silicon divider width are limited to ~20 μm by the deep silicon etching technology. Also, the electroplating takes substantially longer than the partially filled method (tens of hours vs. hours), because the metal is plated up through the thickness of the wafer rather than from the sidewalls. While these structures demonstrated the fabrication method, characterization was not performed, because the partially filled method was selected for implementation, as discussed in Chapter 3.

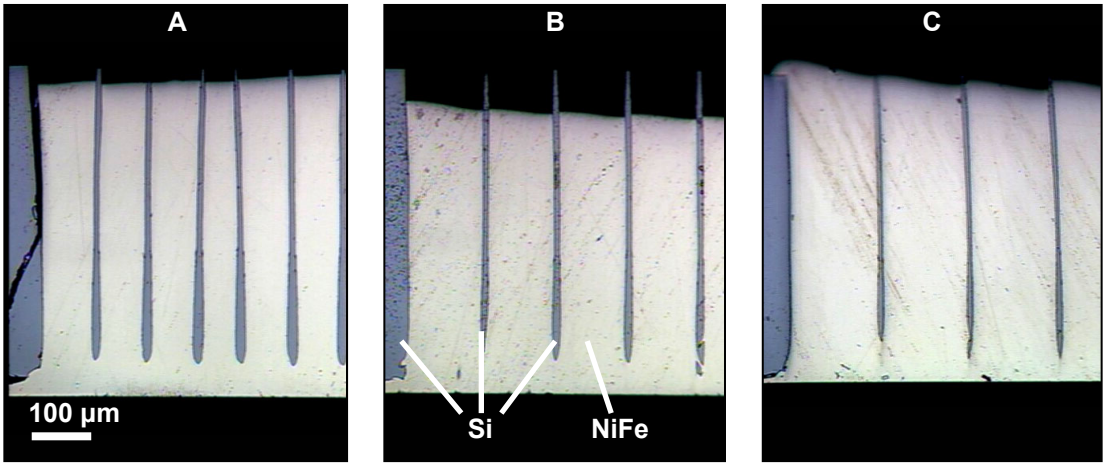

Figure 2.22. Optical images showing partial cross-sections of laminated NiFe structures with w_{div} = 20 µm and various w_{lam} (A = 60 µm, B = 90 µm, and C = 120 µm). Some underplating is seen on the bottom surface, and sample B is not plated all the way to the top surface.

2.3 Thick Solid Magnetic Cores in Silicon

In this section, methods are presented for inlaying large volumes of magnetic materials for the machine rotors. The process is shown in Figure 2.23 and uses low-resistivity (0.001 Ω·cm), n-type, <100> Si wafers. The process begins by depositing a thick (>5 µm) topside oxide layer, achieved using thermal oxidation followed by PECVD (Figure 2.23a). Deep (100 µm +) silicon etches are made in the silicon and a second thermal oxide is grown. Then, using photoresist molds, openings are made in the oxide at the bottom of the trenches (Figure 2.23b). Next, the metal (e.g., NiFe) is electroplated directly on the conductive silicon, overfilling the trenches (Figure 2.23c). The wafer is then polished back down to the original surface, leaving the metal flush with the surface (Figure 2.23d). If needed, a timed wet etch can be used to etch back the first metal layer (Figure 2.23e), and a second metal can be electroplated on top (Figure 2.23f).

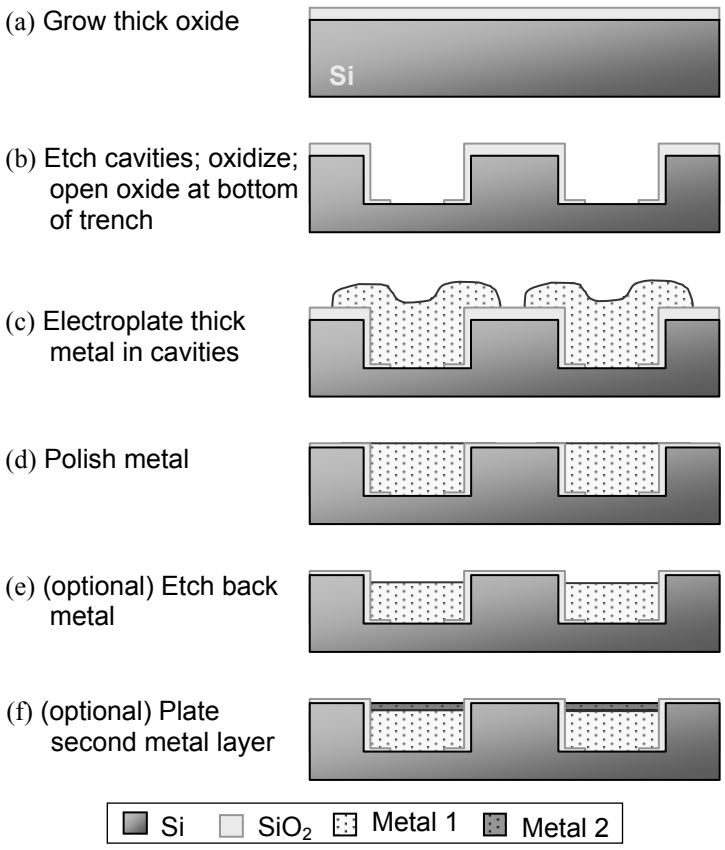

Figure 2.23. Process flow for inlaying thick metal structures within silicon, with optional overcoat metal.

This process was verified by creating thick discs and annuli of NiFe embedded in silicon. The uniformity of the deposits was very good, and typically no delamination occurred. After electroplating, lapping was performed using a 9.5 μm aluminum oxide powder slurry (#17028, Extec Corp., Enfield, CT) followed by polishing with a 0.06 μm colloidal silica polishing suspension (#16790, Extec Corp., Enfield, CT). Figure 2.24 shows a 300-μm thick, 6-mm diameter NiFe disc and Figure 2.25 shows the cross-section of a 350-μm thick, 2 mm annulus of NiFe.

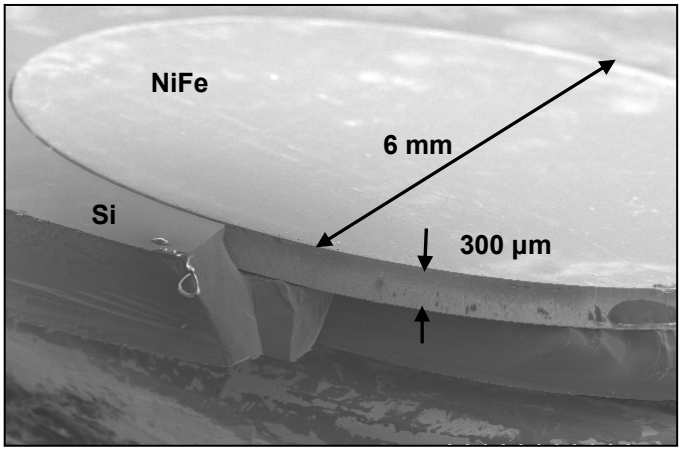

Figure 2.24. SEM of 300-µm thick NiFe disk inlayed in Si. The silicon structure was broken away to reveal the embedded NiFe.

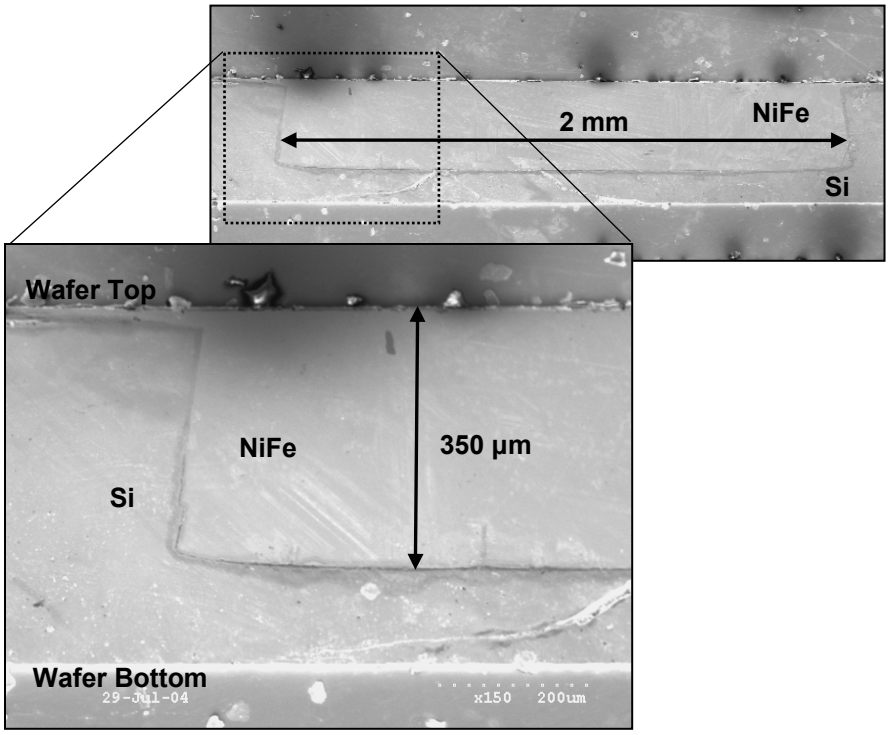

Figure 2.25. Cross-section SEM images of 350-µm thick NiFe annulus inlayed in Si. The scratches in the surface are from dicing/polishing.

Two issues were never solved to enable the integration of rotors within a fusion-bonded silicon stack. First, polishing of the overplated rotor material roughed and contaminated the silicon surface. The protective SiO_2 on the surface tended to be eroded irregularly during the polishing. To remedy this, it was thought that a thick SiO_2 layer could be used as an "etch stop" if suitable selectivity could be achieved between the electroplated metal and SiO_2. Several attempts were made using various polishing slurries/conditions and oxides of up to 15 μm, but a suitable process was never found, using equipment readily available.

The second major issue that was discovered was that annealing of a sample with an embedded rotor at 500°C for 4 hr to emulate a wafer bond anneal (same thermal cycle used for embedding other electroplated metals) resulted in cracking in the surrounding silicon, presumably from thermal stresses. This issue certainly demands attention, but for the short term it was decided to pursue alternative fabrication methods that would enable micromachine characterization without fully embedding or monolithically integrating the rotors in silicon.

CHAPTER 3

OPTIMIZATION OF MICROFABRICATED LAMINATIONS

In a macroscopic, laminated core designed for relatively low frequencies (<10 kHz), the width of the dielectric lamination dividers are typically very small relative to the lamination width. However, for microfabricated devices designed for high-frequency operation, the thickness of the lamination dividers cannot be neglected, and the overall packing density is typically limited by various fabrication constraints. Consider a laminated core and an unlaminated core subjected to a uniform, time-varying magnetic field as shown in Figure 3.1. The laminated core, with laminations of $w_{lam} << h$, has lower eddy current losses, but with a smaller total core volume due to poor lamination packing density. This introduces a design challenge: for a given operating frequency, determine the optimal lamination width based on certain fabrication constraints.

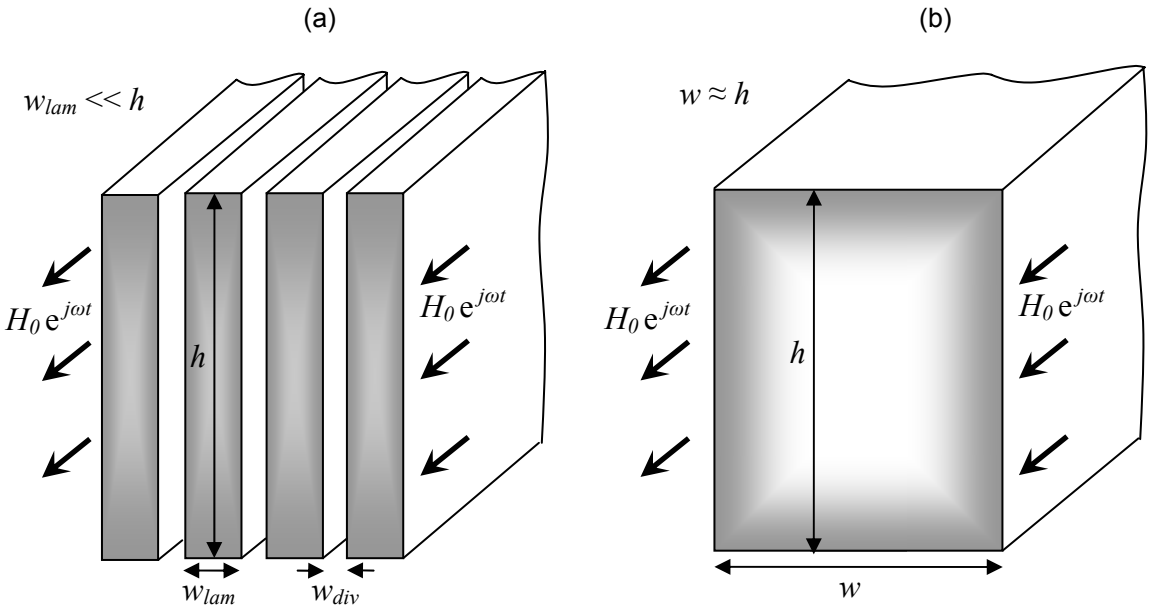

Figure 3.1. Schematic diagram of (a) low-loss laminated core and (b) lossy unlaminated core (magnetic flux depicted by shading).

3.1 Magnetic Diffusion in a Single Lamination

Before proceeding any further, the origin and implication of eddy currents must be understood. This section presents the theoretical development of eddy currents using the magnetic diffusion of a time-harmonic magnetic field in long, thin magnetic slab. The results derived here will be used in the optimization of lamination thickness.

Consider a single magnetic lamination with height, h, much larger than the width $w_{lam} = 2b$ and with infinite extent in the z-direction, as shown in Figure 3.2. Now, assume a uniform, time-varying magnetic field oriented in the z-direction.

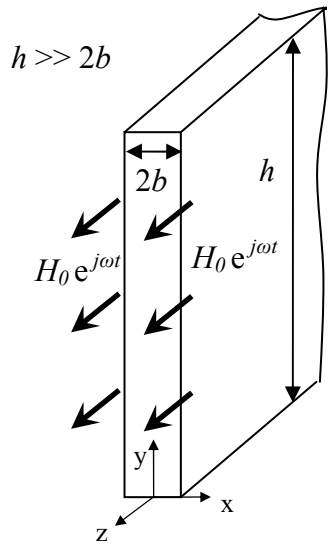

Figure 3.2. Schematic of infinitely long lamination of width $2b$ and height h, bounded both sides by uniform field of $H_0 e^{j\omega t}$.

The field within the lamination is governed by a 1-D magnetic diffusion equation,

$$\frac{\partial^2 H_z}{\partial x^2} = \mu\sigma \frac{\partial H_z}{\partial t}, \tag{3.1}$$

where μ and σ are the permeability and conductivity of the magnetic lamination, respectively. The solution for the field is assumed of the form,

$$H_z(x,t) = \mathrm{Re}\left[\tilde{H}e^{j(\omega t - kx)}\right], \tag{3.2}$$

Substituting Equation 3.2 into 3.1, yields

$$-k^2\tilde{H}e^{j(\omega t-kx)} = j\omega\mu\sigma\tilde{H}e^{j(\omega t-kx)}, \tag{3.3}$$

$$k^2 = -j\omega\mu\sigma, \tag{3.4}$$

$$k = \pm j\frac{1+j}{\sqrt{2}}\sqrt{\omega\mu\sigma} = \pm\frac{(1-j)}{\delta}, \tag{3.5}$$

where δ is the skin depth, defined as

$$\delta = \sqrt{\frac{2}{\omega\mu\sigma}} = \sqrt{\rho/\pi f\mu}\,. \tag{3.6}$$

Equation 3.5 indicates that the magnetic field is comprised of a forward and a backward traveling wave, expressed as

$$H_z(x,t) = H_+e^{j(\omega t-kx)} + H_-e^{j(\omega t-kx)}. \tag{3.7}$$

The boundary conditions on either side of the lamination are given as

$$H_z(x=\pm b,t) = H_0e^{j\omega t}. \tag{3.8}$$

Substituting the boundary conditions from Equation 3.8 into 3.7 yields

$$H_0 = H_+e^{-jkb} + H_-e^{jkb}, \tag{3.9}$$

$$H_0 = H_+e^{jkb} + H_-e^{-jkb}. \tag{3.10}$$

Solving for H_+ and H_- yields,

$$H_+ = H_- = \frac{H_0}{2\cosh(kb)}. \tag{3.11}$$

Thus, the general solution for the magnetic field is

$$H_z(x,t) = \mathrm{Re}\left[H_0e^{j\omega t}\frac{\cosh(kx)}{\cosh(kb)}\right]. \tag{3.12}$$

It follows from $\vec{B} = \mu\vec{H}$ that the magnetic flux density is

$$B_z(x,t) = \mathrm{Re}\left[\mu H_0 e^{j\omega t}\frac{\cosh(kx)}{\cosh(kb)}\right], \tag{3.13}$$

and for the magneto-quasistatic condition, $\vec{J} = \nabla\times\vec{H} = -\frac{\partial H_z}{\partial x}\hat{y}$, the current density is

$$J_y(x,t) = \mathrm{Re}\left[-kH_0 e^{j\omega t}\frac{\sinh(kx)}{\cosh(kb)}\right]. \tag{3.14}$$

Figure 3.3 shows the magnetic flux density and current density (both normalized by the value at the wall) across the thickness of the lamination for various values of the skin depth, δ. The smaller the skin depth (with respect to the lamination width), the smaller the penetration depth of the magnetic wave. When the skin depth is much smaller than the lamination width, the flux in the center region of the lamination is nearly zero, and opposing current densities (eddy currents) are seen near the surfaces. This results in a dramatic reduction in the flux-carrying capacity of the lamination.

The total flux carried in a single lamination is obtained by integrating the magnetic flux density,

$$\begin{aligned}\phi &= \mathrm{Re}\left[h\int_{-b}^{b} B_z(x,t)dx\right]\\ &= \mathrm{Re}\left[\frac{h\mu}{\cosh(kb)}H_0 e^{j\omega t}\int_{-b}^{b}\cosh(kx)dx\right]\\ &= \mathrm{Re}\left[\frac{2h\mu}{k}H_0 e^{j\omega t}\tanh(kb)\right]\end{aligned} \tag{3.15}$$

Equation 3.15 can be expanded by making use of the half-angle identity

$$\tan\left(\frac{x+jy}{2}\right) = \frac{\sinh x + j\sin y}{\cosh x + \cos y}. \tag{3.16}$$

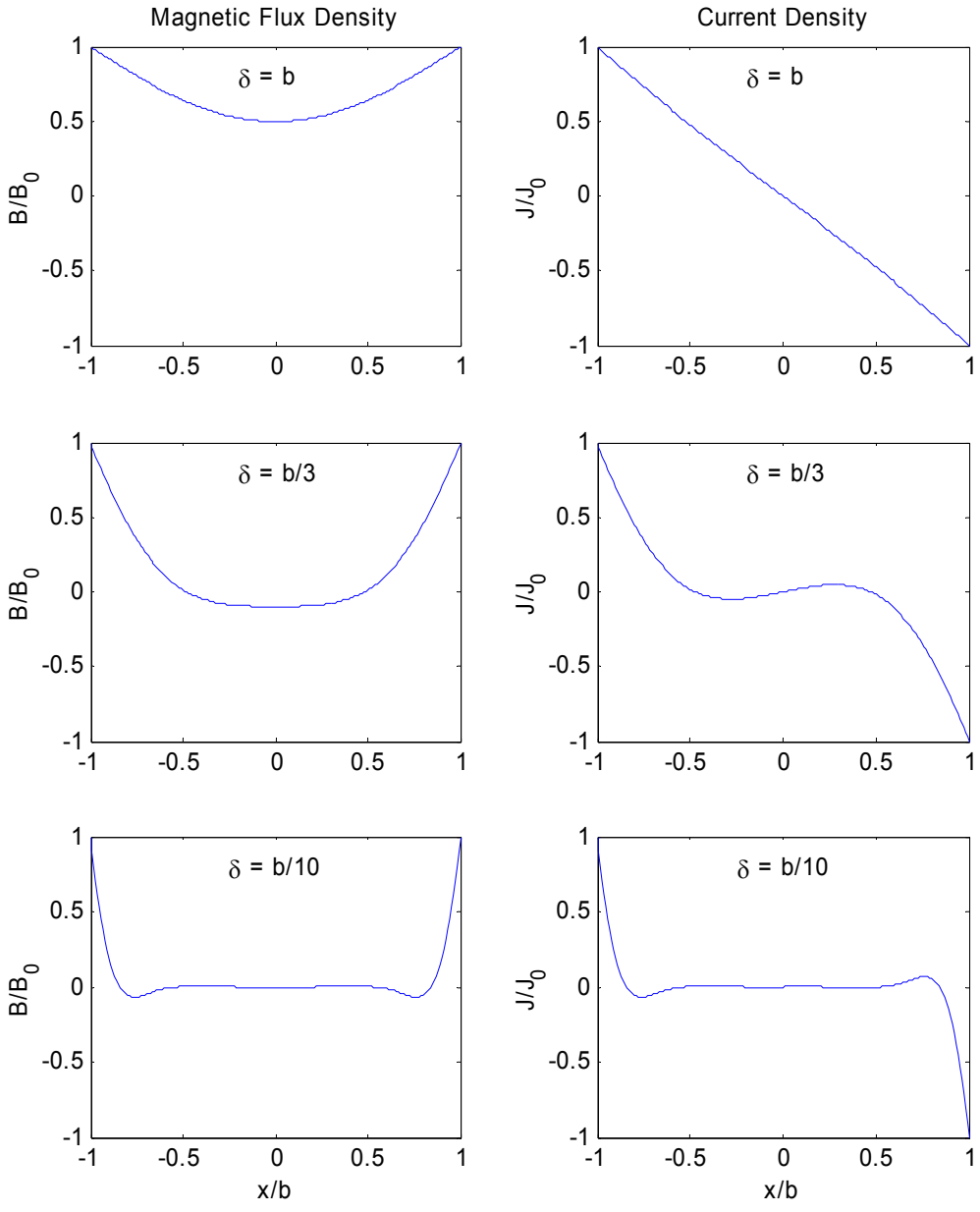

Figure 3.3. Normalized magnetic flux density, B_z, and current density, J_y, plotted as a function of the lamination width for various values of the skin depth, δ.

Thus, substituting for k (Equation 3.5) and expanding yields,

$$\begin{aligned}
\phi &= \mathrm{Re}\left[\frac{2h\mu\delta}{1-j}H_0 e^{j\omega t}\tanh\left(\frac{b}{\delta}(1-j)\right)\right] \\
&= \mathrm{Re}\left[\frac{2h\mu\delta}{1-j}H_0 e^{j\omega t}\frac{\sinh\left(\frac{2b}{\delta}\right)-j\sin\left(\frac{2b}{\delta}\right)}{\cosh\left(\frac{2b}{\delta}\right)+\cos\left(\frac{2b}{\delta}\right)}\right] \\
&= \mathrm{Re}\left[h\mu\delta H_0 e^{j\omega t}\frac{\sinh\left(\frac{2b}{\delta}\right)-j\sin\left(\frac{2b}{\delta}\right)+j\sinh\left(\frac{2b}{\delta}\right)+\sin\left(\frac{2b}{\delta}\right)}{\cosh\left(\frac{2b}{\delta}\right)+\cos\left(\frac{2b}{\delta}\right)}\right] \\
&= \mathrm{Re}\left[h\mu\delta H_0 e^{j\omega t}\frac{\sinh\left(\frac{2b}{\delta}\right)+\sin\left(\frac{2b}{\delta}\right)+j\left[\sinh\left(\frac{2b}{\delta}\right)-\sin\left(\frac{2b}{\delta}\right)\right]}{\cosh\left(\frac{2b}{\delta}\right)+\cos\left(\frac{2b}{\delta}\right)}\right] \\
&= h\mu\delta H_0 e^{j\omega t}\frac{\sinh\left(\frac{2b}{\delta}\right)+\sin\left(\frac{2b}{\delta}\right)}{\cosh\left(\frac{2b}{\delta}\right)+\cos\left(\frac{2b}{\delta}\right)} \quad . \qquad (3.17)
\end{aligned}$$

Equation 3.17 is conveniently rewritten in terms of the nondimensional lamination ratio, n, defined as

$$n = \frac{2b}{\delta} = \frac{w_{lam}}{\delta}, \qquad (3.18)$$

where w_{lam} is the lamination width, and δ is the skin depth. Thus,

$$\phi(n) = \frac{2bh\mu}{n}H_0 e^{j\omega t}\frac{\sinh(n)+\sin(n)}{\cosh(n)+\cos(n)}. \qquad (3.19)$$

3.2 Metrics for Laminated Cores

A laminated core is typically made up of alternating layers of magnetic laminations and dielectric dividers of various widths. Thus, several metrics are defined to enable a comparison of various cores.

3.2.1 Packing Density

The packing density, α, is defined as the ratio between the magnetic (e.g. NiFe) cross-sectional area, $A_{magnetic}$, and the total cross-sectional area, A_{total}, of the core. For a typical core with many alternating magnetic and dielectric layers,

$$\alpha = \frac{A_{magnetic}}{A_{total}} = \frac{w_{lam}}{w_{lam} + w_{div}}, \tag{3.20}$$

where w_{lam} is the magnetic lamination width and w_{div} is the divider width. Equation 3.20 can be non-dimensionalized by normalizing by the skin depth, δ,

$$\alpha(n,m) = \frac{w_{lam}/\delta}{w_{lam}/\delta + w_{div}/\delta} = \frac{n}{n+m}, \tag{3.21}$$

where n, defined as the lamination ratio, is

$$n = \frac{w_{lam}}{\delta} \tag{3.22}$$

and m, defined as the divider ratio, is

$$m = \frac{w_{div}}{\delta}. \tag{3.23}$$

3.2.2 Lamination Efficiency

The total flux through a single lamination, ignoring eddy current effects, is simply the magnetic flux density multiplied by the area,

$$\phi_0 = w_{lam} h \mu H_0 e^{j\omega t}. \tag{3.24}$$

However, when including the eddy currents, the flux is given by Equation 3.19, repeated here as

$$\phi(n) = w_{lam} h \mu H_0 e^{j\omega t} \frac{1}{n} \frac{\sinh(n) + \sin(n)}{\cosh(n) + \cos(n)}. \tag{3.25}$$

Thus, the lamination efficiency, β, is defined as the ratio of the actual flux divided by the flux capacity for a single lamination,

$$\beta(n) = \frac{\phi(n)}{\phi_0} = \frac{1}{n} \frac{\sinh(n) + \sin(n)}{\cosh(n) + \cos(n)}. \tag{3.26}$$

3.2.3 Total Core Efficiency

From an engineering perspective, both packing density and eddy currents limit the total flux that can be passed through a physical core volume. The packing density represents the relative physical volume loss due to the inclusion of laminations, while eddy currents represent a frequency-dependent volume loss. The combined effect can be captured by defining a total core efficiency, η, where

$$\eta(n,m) = \alpha(n,m)\beta(n). \tag{3.27}$$

The core efficiency can be interpreted as the percentage of "useful" flux-carrying volume within the total volume occupied by the laminated, lossy core, as compared to a lossless, unlaminated core occupying the same volume.

3.3 Comparison of Fully Filled vs. Partially Filled Trench Laminations

Using the framework developed in Sections 3.1 and 3.2, this section compares the two lamination fabrication methods developed in Section 2.2.

The partially filled trenches result in a structure with a repetitive lamination pattern of NiFe : Si : NiFe : Air. The packing density for this configuration is given by

$$\alpha_1 = \frac{2w_{lam}}{2w_{lam} + w_{air} + w_{div}}, \tag{3.28}$$

where w_{lam} is the width of the magnetic lamination, w_{div} is the width of the silicon divider, and w_{air} is the width of the resulting air gap. Using the fabrication constraint of $w_{air} = w_{lam}$, the packing density reduces to

$$\alpha_1 = \frac{2w_{lam}}{3w_{lam} + w_{div}} = \frac{2n}{3n + m}, \tag{3.29}$$

where $n = w_{lam} / \delta$ and $m = w_{div} / \delta$. For this lamination scheme, the packing density approaches only 2/3, even as the silicon divider width goes to zero ($m \rightarrow 0$), due to the limiting constraint of maintaining an air gap to avoid keyholing.

Conversely, the fully filled trenches result in a repetitive lamination structure of NiFe : Si. Thus, the packing density for this configuration is

$$\alpha_2 = \frac{w_{lam}}{w_{lam} + w_{div}} = \frac{n}{n + m}, \tag{3.30}$$

Here, as the divider width goes to zero ($m \rightarrow 0$), the packing density asymptotes to 1. Mathematically this is correct, but for either partially or fully filled trenches, the minimum divider width is a function of the silicon etching precision, and m can be quite large at high frequencies.

Using Equations 3.26, 3.27, 3.29, and 3.30, the lamination efficiency, flux efficiency, and total core efficiency were calculated as a function of the lamination ratio, as shown in Figures 3.4. As can be seen, there is an optimal lamination thickness to maximize the core efficiency. Very thin laminations have low packing density, but very thick laminations have large eddy current losses. These plots are for a fixed divider ratio of $m = 0.1$. Figure 3.5 shows the dependence of the total core efficiency on silicon

divider width; smaller silicon dividers result in higher packing densities and thus higher overall efficiency.

Both the partially and fully filled trench methods offer solutions for achieving high aspect-ratio vertical magnetic laminations in silicon. However, there are clearly some advantages and disadvantages to each technique. The partially filled trench method offers lower core efficiencies, but can achieve finer laminations. Also, the "sidewall-in" plating scheme requires minimal plating time. The fully filled trench method offers higher packing densities, but the minimum lamination width is limited by the minimum achievable trench (~20 μm in a 500 μm thick wafer). Also, this "bottom-up" method takes significantly more plating time. A summary comparison of the two methods is shown in Table 3.1.

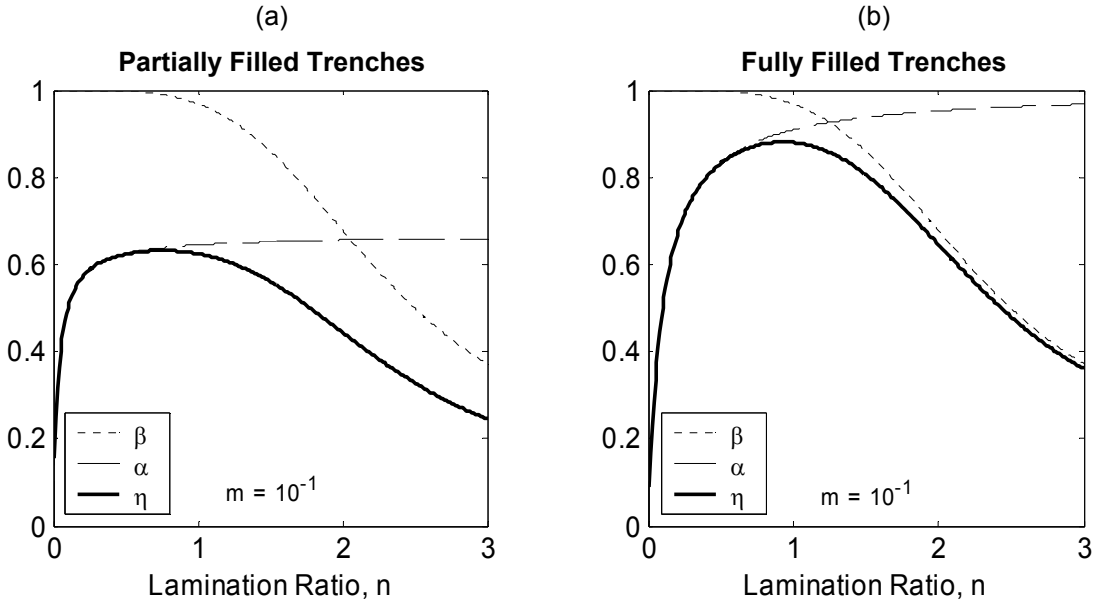

Figure 3.4. Efficiencies for (a) partially and (b) fully filled trenches: packing density, α, magnetic flux efficiency, β, and total core efficiency, η, for divider ratio $m = 0.1$. (Note: $n = w_{lam} / \delta$ and $m = w_{div} / \delta$).

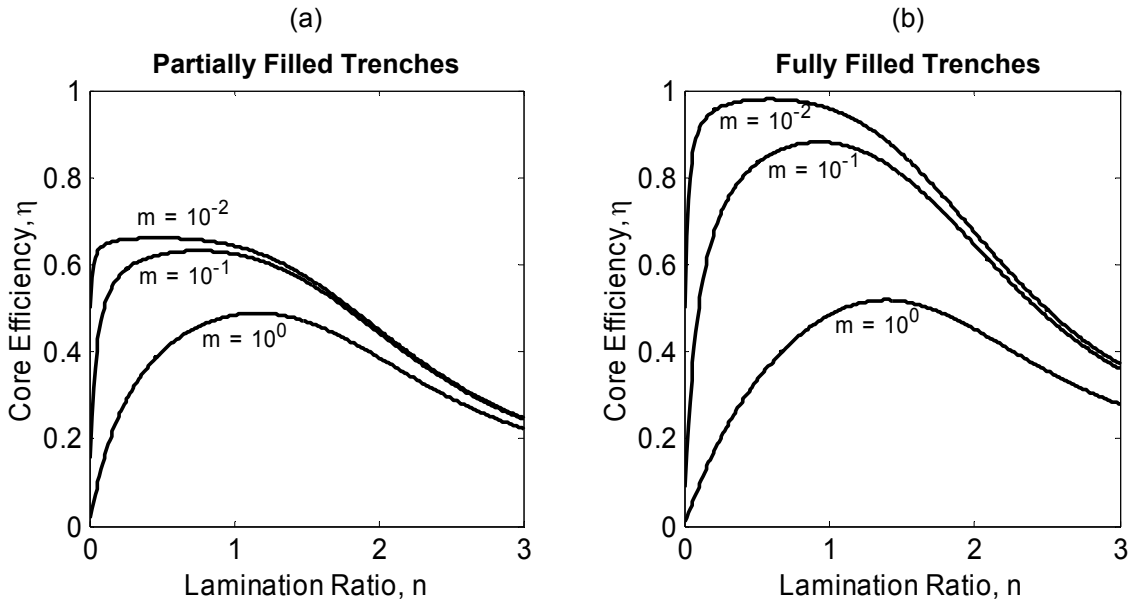

Figure 3.5. Total core efficiency, η, for (a) partially and (b) fully filled trenches for various divider ratios, m. (Note: $n = w_{lam} / \delta$ and $m = w_{div} / \delta$).

Table 3.1. Comparison of two fabrication methods for achieving vertically laminated cores.

Parameter	**Partially Filled**	**Fully Filled**
Lamination Range	< 1 μm - 500 μm	20 μm – 2000 μm
Max. Theoretical Core Efficiency (m = 0)	67%	100%
Max. Practical Core Efficiency* (m = 0.1)	63% @ n=0.75	88% @ n=0.93
Limiting Fabrication Constraints	$w_{div} > 20$ μm $w_{lam} = w_{air}$	$w_{div} > 20$ μm $w_{lam} > 20$ μm
Plating Time	hours	Tens of hours
Notes	Smaller laminations, poorer packing density, simple fab	Better packing density, larger laminations, complex fab

* Values are assumed for 20 μm silicon divider in 500 μm thick wafer.

3.4 Optimal Laminations for Magnetic Machines

This analysis is applied to the design of the proposed magnetic machines. The skin depth, given by Equation 3.6, depends on the electrical operating frequency and material properties. For the calculations, it is assumed the machine has 8-poles, μ_r =1000, and ρ = 15 μΩ·cm (e.g. NiFe or CoFeNi), and the previously discussed fabrication constraint of a minimum lamination divider width of 20 μm.

The optimum lamination width, skin depth, and total core efficiencies were computed at various synchronous operating speeds up to 1 Mrpm (f_e = 66.7 kHz). The results are plotted in Figure 3.6. At 1 Mrpm, the skin depth is 28 μm. The partially filled method has an estimated total core efficiency of 52% for 30 μm laminations, while the fully filled predicts 59% for 36 μm laminations. As expected, the partially filled method requires finer laminations because it has a poorer packing density.

As for the laminations to be implemented in the proposed magnetic machines, there are several factors to consider. The fully filled method would require silicon through etches of 38 μm ($w_{etch} = w_{lam}$), whereas the partially filled method requires only 90 μm wide silicon etches ($w_{etch} = 3 \times w_{lam}$), which are much easier to fabricate. Also, the fully filled method offers only a modest improvement in flux efficiency with the drawback of much longer deposition times. For all of these reasons, the partially filled method was selected for implementation in the induction machines, as discussed in Chapter 4.

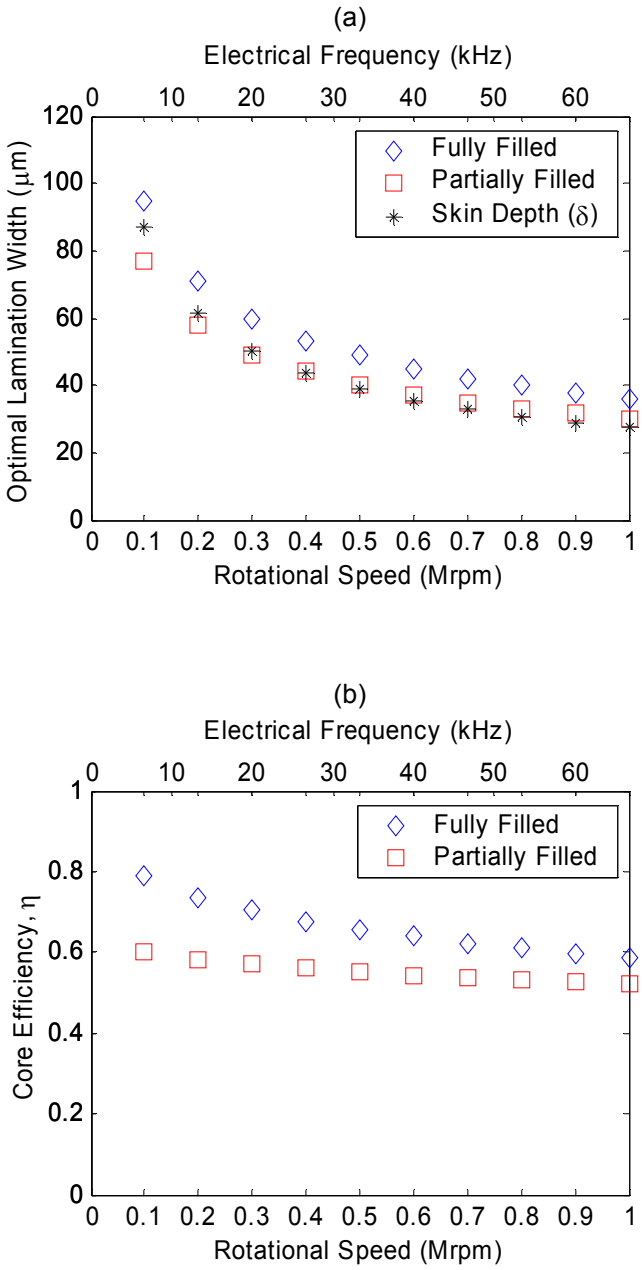

Figure 3.6. (a) Optimal lamination thickness and total core efficiency (b) for proposed magnetic machines, assuming w_{div} = 20 μm, μ_r =1000, ρ = 15 μΩ·cm.

CHAPTER 4

MAGNETIC INDUCTION MACHINES

This chapter presents the design, fabrication, and preliminary characterization of silicon fusion-bonded, laminated magnetic induction machines intended for microengine power generation systems. The previously discussed fabrication techniques were used to form the machine structures entirely within etched and wafer-bonded silicon. Tethered rotor torque measurements confirmed the successful operation of the induction machines. It should be noted that most of the electromechanical analysis and design of the power electronics were performed by MIT, while the fabrication and material characterization were performed by Georgia Tech. Tradeoffs between design and fabrication were resolved by cooperation between the two institutions, and the machine characterization was conducted as a joint effort.

The induction machines were developed for maximum power density and efficiency in the context of interoperability with a microengine system. The turbine-generator system is expected to operate with a ~10-mm OD rotor spinning at ~1 Mrpm (500 m/s tip speed). Temperatures in the "cool" section of the microengine are expected to be ~300°C. As discussed previously, multi-wafer fusion bonding is the desired method for fabrication and integration of the microengine components.

These system-level design and fabrication requirements imposed certain constraints on the design of the magnetic machine. For example, only materials that could withstand the high operating temperatures were considered. In addition, the machine geometry and size was governed by the space allocated within the proposed

silicon microengine. Lastly, efforts were made to use fabrication methods that could ultimately be integrated into a multi-wafer fusion bonding process.

4.1 Induction Machine Design

An induction machine operates through the interaction of a traveling magnetic wave in the rotor-stator air gap and induced magnetic fields in the rotor [70,71]. Consider a stator with multiphase windings and a rotor wound with similar windings that are electrically closed (short-circuited). The stator is appropriately energized to induce a traveling magnetic wave in the air gap that rotates at the synchronous speed,

$$\omega_s = \frac{2\pi f_e}{(p/2)} = \frac{4\pi f_e}{p}, \tag{4.1}$$

where f_e is the electrical frequency of the voltages applied to the windings and p is the number of poles. Now consider the rotor rotating in the same direction as the magnetic wave but at some different angular speed $\omega_m \neq \omega_e$. The rotor "sees" a traveling magnetic wave at angular frequency

$$\omega_r = \omega_s - \omega_m. \tag{4.2}$$

It is convenient to normalize the rotor frequency by the synchronous frequency, resulting in a non-dimensional parameter known as slip, s, where

$$s = \frac{\omega_r}{\omega_s} = \frac{\omega_s - \omega_m}{\omega_s}. \tag{4.3}$$

From the rotor's perspective, the magnetic wave appears as a time-varying field at the frequency, f_r, denoted as the rotor frequency or slip frequency,

$$f_r = \frac{\omega_r}{2\pi} = sf_s. \tag{4.4}$$

This time-varying magnetic field induces currents in the rotor windings and, as a result, establishes magnetic poles in the rotor. These induced poles are the source of the name "induction machine" and form the basis for electromechanical interaction. The two magnetic fields, the applied mmf from the stator, F_s, and the induced mmf, F_r, from the rotor, tend to align their poles in the same way as two bar magnets.

The net torque, T, acting on the rotor, and for any magnetic machine for that matter, can be expressed as [70]:

$$T \propto pF_s F_r \sin \delta_{sr}, \tag{4.5}$$

where p is the number of poles and δ_{sr} is the phase angle between the stator and rotor mmfs. For the induction machine, the torque is a function of the stator current, I_s, and slip frequency, s, as described below.

First, the rotor and stator mmfs are proportional to the stator and rotor currents, respectively,

$$\begin{aligned} F_s &\propto I_s \\ F_r &\propto I_r \end{aligned}, \tag{4.6}$$

Now the rotor current is determined by the induced rotor voltage, E_r, and rotor impedance, Z_r, both at the slip frequency,

$$I_r = E_r / Z_r. \tag{4.7}$$

The induced voltage is governed by the magnetic circuit, and assuming unsaturated ferromagnetic stator and rotor materials, is proportional to the stator current and slip frequency, f_r (which is proportional to slip, s),

$$E_r \propto I_s s \quad \text{(linear regime)}. \tag{4.8}$$

Upon saturation, the flux remains nearly constant, even with increasing stator current, so

$$E_r \propto s \quad \text{(saturated regime).} \tag{4.9}$$

The rotor impedance also varies with the slip frequency. At low slip, the rotor impedance is nearly purely resistive, so the rotor current is nearly proportional to and in phase with the rotor voltage. Also, the rotor mmf lags ~90° behind the stator mmf , so sin $\delta_{sr} \approx 1$. Therefore in the low-slip regime the torque is proportional to slip and either linearly or quadratically related to the stator current,

$$\begin{aligned} T\big|_{s\to 0} &\propto pI_s^{\,2}\, s \quad \text{(unsaturated regime)} \\ T\big|_{s\to 0} &\propto pI_s s \quad \text{(saturated regime)} \end{aligned} . \tag{4.10}$$

Of course, at the synchronous speed, $s = 0$, so $I_r = 0$, and no torque is generated. As the slip frequency increases, the rotor impedance grows (due to the inductive component) and adds additional phase lag between the rotor current and voltage. This results in additional lag between the rotor mmf and voltage, causing sin δ_{sr} to decrease. Thus, as slip is increased, the torque grows linearly until a maximum, followed by a gradual decline. It is interesting to note that torque production is independent of the actual mechanical rotational speed, ω_m; it is solely governed by the slip frequency, ω_r.

It should be noted that the description of the mechanisms above described magnetic induction in a rotor with discrete conductive windings. In most macroscale machines, this is accomplished using a squirrel-cage design, where many conductive bars are connected in parallel via end rings. In operation, currents circulate through the bars and end rings, effectively forming a rotor with the same number of poles as the stator with a large number of phases [71]. Extending this concept to an infinite number of infinitely thin parallel conductors, a thin conductive layer can be used on the surface of a solid ferromagnetic rotor, commonly employed in small, high-speed machines [71]. In

this case, magnetic induction relies on inducing circulating eddy currents, as opposed to currents that flow in discrete conductors.

Thus, induction machines were designed with planar geometry, consisting of a two-phase, eight-pole, stator and a composite, annular rotor, as shown in Figure 4.1. The stator contains two planar 35-μm thick, 300-μm wide embedded Cu coils wound in a three-dimensional, vertically laminated, electroplated ferromagnetic core, all supported by a silicon frame. The core (10 mm OD, 6 mm ID) is formed by onion-like concentric laminations, where the lamination thickness is approximately one skin depth (~30 μm) to limit eddy current losses at the proposed maximum operating frequency of 66.7 kHz (see Chapter 3).

Machines were designed using either electroplated $Ni_{81}Fe_{19}$ or $Co_{52}Fe_{26}Ni_{22}$ as the ferromagnetic material. As compared to NiFe, the CoFeNi alloy has similar permeability (~300-1000) and resistivity (~15-30 μΩ·cm), but offers higher saturation magnetization (~1.8 T vs. ~0.8 T), for higher power density, at the expense of an increase in coercivity (~100 A/m vs. ~50 A/m), resulting in a larger hysteresis loss. Also, the CoFeNi alloy has a higher Curie temperature (~850 °C vs. ~550 °C) [72], permitting higher operating temperatures.

Also, besides fabrication compatibility within the silicon-based microengine, the use of silicon offers several design advantages over the previous SU-8 based machines [29-35]. First, the high thermal conductivity of silicon should enable higher coil current densities, translating to higher power density. Second, deep silicon etching may permit improved dimensional tolerances to enable finer magnetic laminations for higher frequency operation and/or higher lamination packing densities in the machine core.

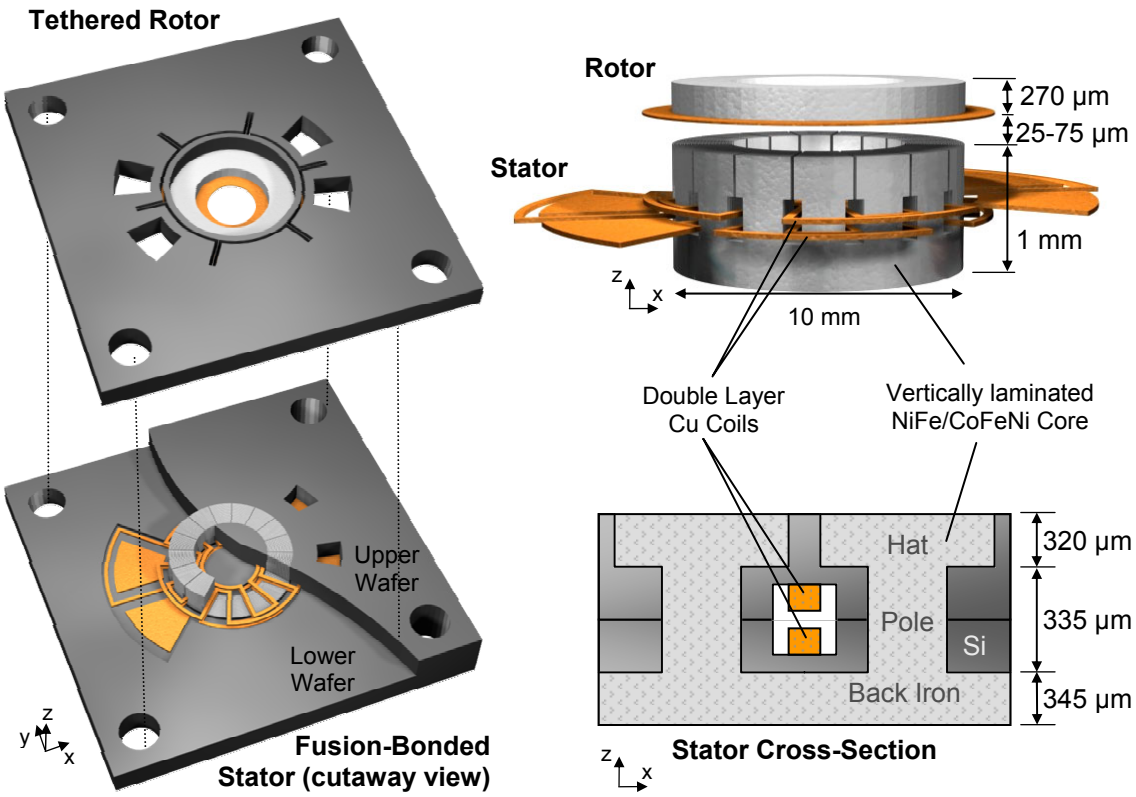

Figure 4.1. Renderings of the magnetic induction machine (z-axis expanded by 4x and air gap exaggerated). The cutaway view of the stator shows the machine components embedded within the bonded silicon.

The rotor is a 250-μm thick ferromagnetic annular ring (10-mm OD, 6-mm ID) with a thin overlayer of Cu. This type of structure simplifies the fabrication of the rotor and maximizes mechanical symmetry for eventual high-speed rotation. The 20-μm thick Cu (12-mm OD, 4-mm ID) layer serves as a distribute rotor conductor to enhance eddy current generation to maximize torque. The Cu region extends beyond the ferromagnetic region of the rotor to serve as electrical end turns for the eddy currents.

For initial characterization purposes, the rotor was designed to be suspended above the stator using flexible silicon tethers that permitted angular rotation and a controllable air gap while avoiding the difficulties of supporting a spinning rotor. This situation simulates a blocked rotor condition (rotor frequency equals the synchronous frequency ($f_r = f_s$) and no mechanical losses), commonly used to test macroscale machines, [71]. The details of the design and analysis of the tethered rotor test stand is discussed in Section 4.3.

4.2 Induction Machine Modeling

Extensive machine modeling was performed by colleagues at MIT, the details of which can be found in [30,31,33,35]. The general concept is depicted in Figure 4.2. The fields in a 2-D model are evaluated at a discrete radius, and the total output is achieved by integrating the results across all radii. The stator is modeled as a reluctance circuit, while the air gap and rotor are modeled using 2D Maxwell equations, with the B- and H-fields matched at the interface. Inputs and outputs to the model include the time-varying currents in the stator, and the velocity and torque in the rotor. The models incorporate the measured B-H characteristics of the electroplated materials used and capture eddy current, saturation, and hysteresis effects.

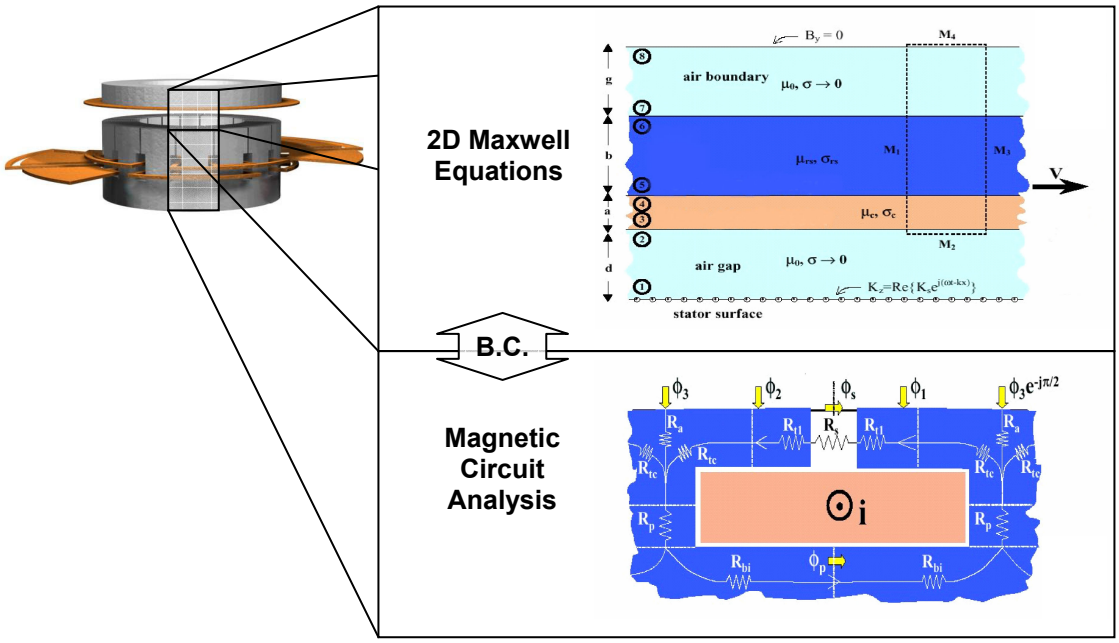

Figure 4.2. General modeling concept of induction machines performed by MIT [30,31,33,35].

The induction machine can also be represented by an equivalent circuit model [71], as shown in Figure 4.3. The device takes a form similar to a transformer with input electrical power applied across the terminals and output mechanical power measured across a variable load resistor. The circuit model parameters would generally be extracted from two experimental measurements: (1) no-load test, corresponding to a transformer open-circuit measurement and (2) blocked-rotor test, corresponding to a transformer short-circuit test [71]. Obviously, these measurements are not possible during the design stage, but the circuit model can be used to illustrate the operation of the machine.

The mechanical-to-electrical power conversion is represented by the slip dependent resistance,

$$R_2 \frac{1-s}{s}. \tag{4.11}$$

For $\omega_s > \omega_m$, the slip is positive, resulting in a positive load resistance. Physically, the traveling magnetic wave is spinning faster than the rotor, effectively pulling the rotor around. The machine is operating in motoring mode and electrical power is converted to mechanical power in the form of shaft torque. In the opposite case, for $\omega_s < \omega_m$, the slip is negative, resulting in a negative load resistance. Physically, the rotor is spinning faster than the magnetic wave, and the machine is operating as a generator. Excess mechanical power is converted to electrical power, resulting in a net electrical current flowing back into the electrical circuit.

To better illustrate the power losses in the machine, the power flow in motoring mode is illustrated in Figure 4.4. Electrical power, P_i, flows into the terminals of the device, but some power, P_{cond}, is dissipated due to the finite resistance of the stator coils, R_1. Also, some power is lost in the core, P_{core}, as a result of hysteresis and eddy currents. What power is left, P_g, is transferred across the air gap into the rotor. Some of this power is dissipated across R_2 as conduction loss within in the rotor, P_{rotor}. What remains is converted into mechanical power, P_m. The percentage of the power transferred across the gap, P_g, that is converted into mechanical power, P_m, is precisely 1-s. Finally, the net output shaft power, P_o, is that which remains after the mechanical losses, P_{rot}, are accounted for.

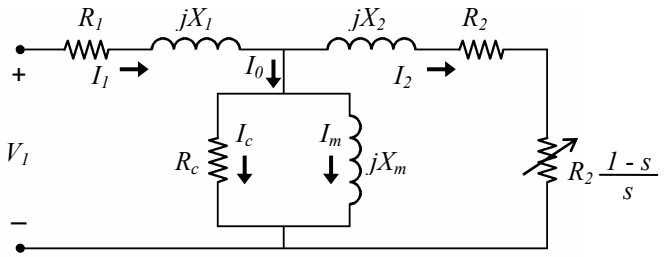

Figure 4.3. Equivalent per-phase circuit of an induction machine.

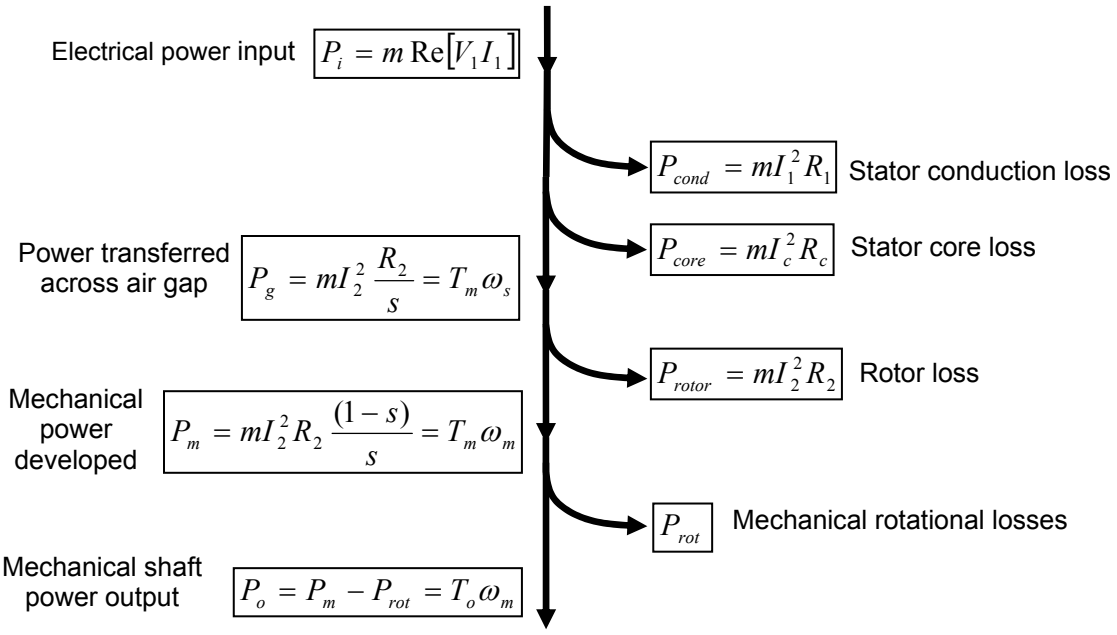

Figure 4.4. Power flow for *m*-phase induction machine in motoring mode.

4.3 Tethered Rotor Test Stand

For characterization of the induction machines, a tethered rotor test stand was assembled. The setup enabled blocked rotor torque measurements, and avoided the difficulties of supporting and stabilizing a spinning rotor.

4.3.1 Experimental Setup

The tethered rotor test stand was developed to permit measurements of the blocked-rotor motoring torque, as previously demonstrated for the electric and magnetic induction machines [23,29,31-34]. In practice, the rotor was suspended above the stator with flexible silicon tethers. The stator and tethered rotor structure were clamped together and mounted on a water-cooled chuck, as shown in Figures 4.5 and 4.6. Nominal air gaps of 25-75 μm were maintained between the stator and rotor by using appropriate spacers made of Kapton.

Power electronics supplied a balanced current excitation in quadrature to the two stator phases, creating a motoring torque. The drive signals were routed through a circuit that could swap the phases to cyclically alternate the torque direction. Using this setup, the tethered rotor was excited into mechanical oscillation at a frequency (<1 kHz), the "torque reversal frequency," much lower than the electrical coil frequency (tens of kHz).

A microvision image analysis system [73] was used to dynamically measure the displacement of the outer most radius of the rotor silicon ring under the influence of the oscillating torque input. This dynamic measurement offered two primary benefits over static measurements. First, larger deflections could be obtained near the mechanical resonant frequency, which were easier to measure. Second, the spring stiffness could be extracted from the measurements, rather than estimated from the geometry of the tethers. This is important, considering the spring coefficient has 3^{rd}-order dependence on geometrical lengths, as shown in Equation 4.18.

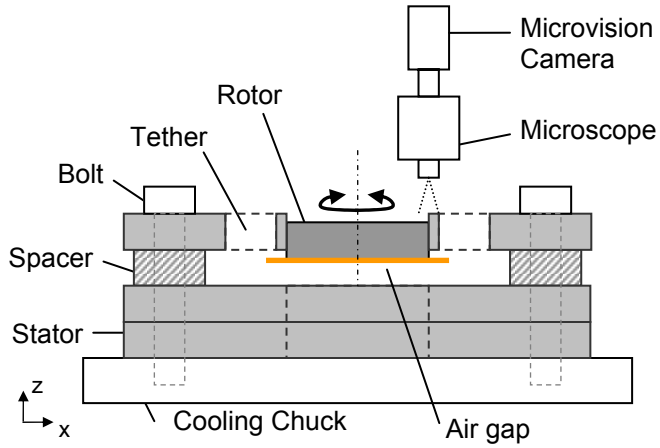

Figure 4.5. Schematic of the induction machine tethered rotor torque measurement test stand showing the tethered rotor structure clamped to the stator on the cooling chuck.

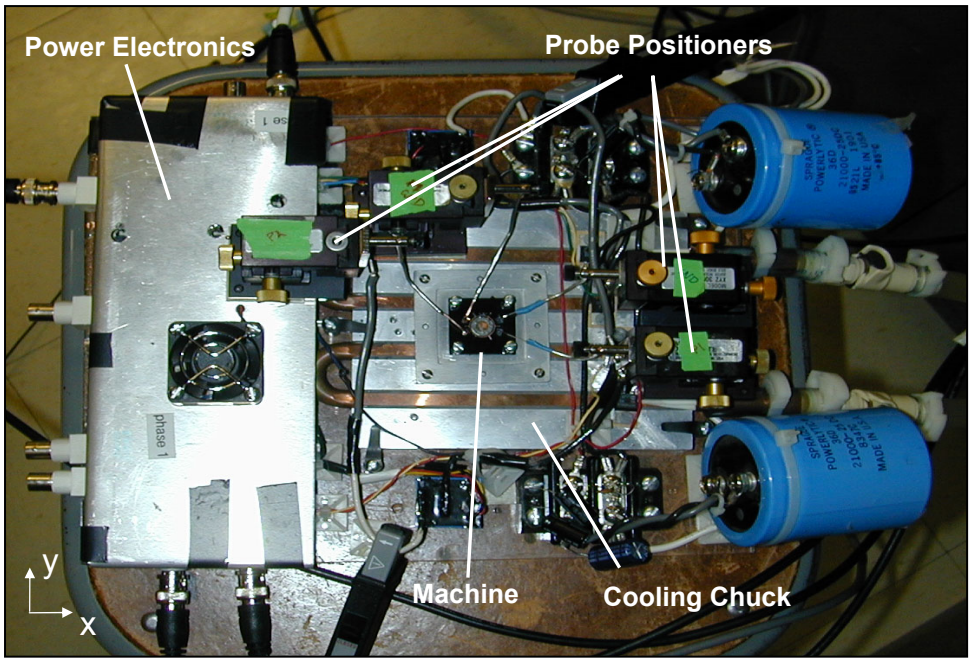

Figure 4.6. Top-view photograph of tethered rotor test stand.

4.3.2 Tethered Rotor Dynamics

The tethers for the tethered rotor were designed to permit angular rotation in the θ-direction while maintaining sufficient strength in the z-direction to counteract the magnetic pull-in forces (the tendency of the rotor to close the magnetic gap with the stator). This section presents the analysis of the dynamics in both the angular (θ-axis) and axial (z-axis) directions.

Angular Deflections

The rotational forces acting on the tethered rotor are shown in Figure 4.7 A torque balance about the center of the rotor (ignoring damping) gives,

$$\sum \vec{M} = J\ddot{\theta}\,, \tag{4.12}$$

$$T - NaF_{tether} = J\ddot{\theta}\,, \tag{4.13}$$

where J is the rotor moment of inertia, T is the magnetically induced torque, a is the radius of the rotor, F_{tether} is the θ-directed reaction force from a single tether, and N is the number of tethers.

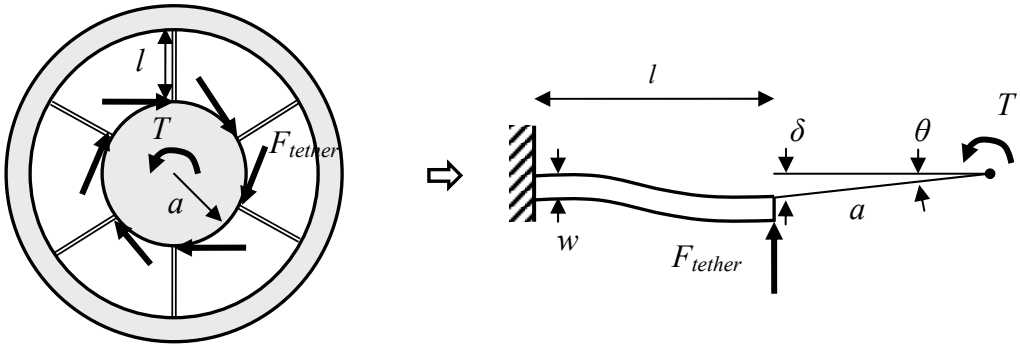

Figure 4.7 Rotational forces in tethered rotor system.

For small deflections, the force from a single tether, F_{tether}, is modeled as a reactionary force from a beam with one clamped end and one guided end (slope=0). The force for a deflection, δ, is given by [74]

$$F_{tether} = \frac{12EI_\theta}{l^3}\delta, \tag{4.14}$$

where E = 166 GPa is the elastic modulus of silicon and l is the length of the tether. The moment of inertia of a tether for deflection in the θ-direction, I_θ, is given by

$$I_\theta = \tfrac{1}{12}tw^3, \tag{4.15}$$

where t and w are the thickness and width, respectively, of a silicon tether. For small deflections, the deflection, δ, can be linearized with the angular rotation of the rotor,

$$\delta = a\sin\theta \approx a\theta. \tag{4.16}$$

Substituting Equations 4.14-4.16 back into Equation 4.12 yields

$$T = J\ddot{\theta} + k_\theta\theta, \tag{4.17}$$

where k_θ is a stiffness coefficient based on the geometry of the tether and rotor, and

$$k_\theta = a^2 NEt\left(\frac{w}{l}\right)^3. \tag{4.18}$$

Taking the Laplace transform of Equation 4.17 yields the following transfer function between the rotation angle, θ, and the electromagnetic torque, T,

$$T(s) = [Js^2 + k_\theta]\theta(s), \tag{4.19}$$

$$\frac{\theta(s)}{T(s)} = \frac{1}{Js^2 + k_\theta}, \tag{4.20}$$

$$\frac{\theta(j\omega)}{T(j\omega)} = \frac{\theta(s)}{T(s)}\bigg|_{s=j\omega} = \frac{1}{k_\theta - J\omega^2}, \tag{4.21}$$

which is a simple undamped, second-order system. Two key figures of merit are the DC (zero-frequency) compliance and the resonant frequency. The compliance, g_θ, given by

$$g_\theta = \left.\frac{\theta(s)}{T(s)}\right|_{s=0} = \frac{1}{k_\theta} = \frac{1}{a^2 NEt}\left(\frac{l}{w}\right)^3, \tag{4.22}$$

represents the angular change for a given electromagnetic torque, and is simply the inverse of the spring coefficient. At resonance, the real part of the transfer function is infinite. Thus, the resonant frequency, $f_{0\theta}$, can be solved by setting the denominator of Equation 4.21 equal to zero, or

$$k_\theta - J\omega^2 = 0, \tag{4.23}$$

$$\omega_0 = \sqrt{\frac{k_\theta}{J}}, \tag{4.24}$$

$$f_{0\theta} = \frac{1}{2\pi}\sqrt{\frac{k_\theta}{J}} = \frac{1}{2\pi}\sqrt{\frac{a^2 NEt}{J}\left(\frac{w}{l}\right)^3}. \tag{4.25}$$

Axial Deflections

Assuming a symmetric distribution of N tethers and a rigid rotor, no net in plane forces or moments will be induced in the rotor. Therefore, the rotor can be replaced by a point mass, m, with applied electromagnetic normal force, F, and reactionary forces from tether pairs, $F_{tether\text{-}pair}$, as shown in Figure 4.8 Each tether pair is modeled as a clamped-clamped beam of length $2l$, and there are $N/2$ pairs. A force balance in the z-direction yields,

$$\sum F_z = m\ddot{z}, \tag{4.26}$$

$$F - \frac{N}{2}F_{tether-pair} = m\ddot{z}. \tag{4.27}$$

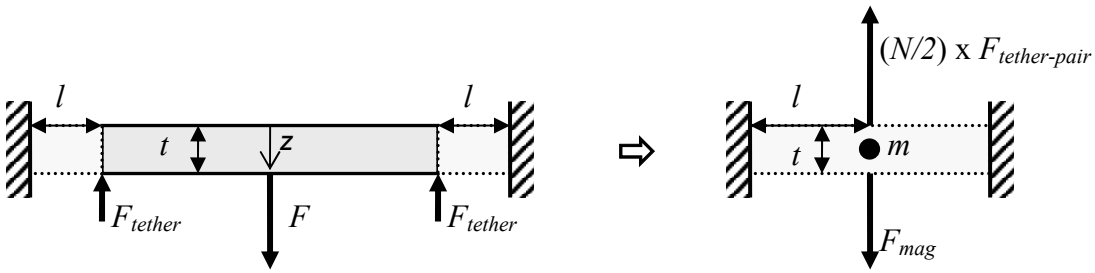

Figure 4.8 Axial forces in tethered rotor system.

The force necessary to deflect the center of a clamped-clamped beam, $F_{tether\text{-}pair}$, a distance, z, is [74],

$$F_{tether-pair} = \frac{192EI_z}{(2l)^3} z \tag{4.28}$$

where E = 166 GPa is the elastic modulus of silicon and l is the length of each tether. The moment of inertia for deflection of the beam in the z-direction, I_z, is given by,

$$I = \tfrac{1}{12} wt^3 , \tag{4.29}$$

where w and t are the width and thickness, respectively, of a silicon tether. Combining Equations 4.27-4.29 yields,

$$F = m\ddot{z} + k_z z . \tag{4.30}$$

The combined reaction forces of the tethers form a stiffness, k_z, where

$$k_z = NEw\left(\frac{t}{l}\right)^3 . \tag{4.31}$$

Applying Laplace transforms to Equation 4.30 yields the transfer function between the normal electromagnetic force, F, and the displacement, z,

$$F(s) = [ms^2 + k_z]Z(s), \tag{4.32}$$

$$\frac{Z(s)}{F(s)} = \frac{1}{ms^2 + k_z}, \tag{4.33}$$

$$\frac{Z(j\omega)}{F(j\omega)} = \left.\frac{Z(s)}{F(s)}\right|_{s=j\omega} = \frac{1}{k_z - m\omega^2}. \tag{4.34}$$

The DC compliance, g_z, and resonant frequency, f_{0z}, derived as shown previously, are

$$g_z = \left.\frac{Z(s)}{F(s)}\right|_{s=0} = \frac{1}{k_z} = \frac{1}{NEw}\left(\frac{l}{t}\right)^3 \tag{4.35}$$

and

$$f_{0z} = \frac{1}{2\pi}\sqrt{\frac{k_z}{m}} = \frac{1}{2\pi}\sqrt{\frac{NEw}{m}\left(\frac{t}{l}\right)^3}. \tag{4.36}$$

Rotor Mass and Angular Moment of Inertia

Until now, the rotor has been assumed to be rigid body with mass, m, and angular moment of inertia, J. In reality, the tethered rotor is a composite structure containing a ferromagnetic annulus, conductive overlayer, and silicon retaining ring, as shown in Figure 4.9

The total mass and inertia are simply the algebraic sums of the mass and inertia, respectively, of each of three rotor pieces. For a simple annulus with density, ρ, thickness, t, outer radius, r_o, and inner radius, r_i, the mass is given by

$$\begin{aligned} m_{annulus} &= \int_V \rho \, dV \\ &= \int_{z=0}^{t}\int_{\theta=0}^{2\pi}\int_{r=r_i}^{r_o} \rho r dr d\theta dz, \\ &= \rho t \pi (r_o^2 - r_i^2) \end{aligned} \tag{4.37}$$

and the corresponding moment of inertia is given by

$$\begin{aligned} J_{annulus} &= \int_V \rho r^2 dV \\ &= \int_{z=0}^{t} \int_{\theta=0}^{2\pi} \int_{r=r_i}^{r_o} \rho r^3 dr d\theta dz \,. \\ &= \tfrac{1}{2} \rho t \pi (r_o^4 - r_i^4) \end{aligned} \tag{4.38}$$

Thus, for the composite rotor, as shown in Figure 4.9 the mass and moment of inertia are

$$\begin{aligned} m &= \pi \left[\rho_{ring} t_{ring} (a^2 - b^2) + \rho_{mag} t_{mag} (b^2 - c^2) + \rho_{cond} t_{cond} (e^2 - d^2) \right] \\ &= 145\,\text{mg} \end{aligned} \tag{4.39}$$

and

$$\begin{aligned} J &= \tfrac{1}{2} \pi \left[\rho_{ring} t_{ring} (a^4 - b^4) + \rho_{mag} t_{mag} (b^4 - c^4) + \rho_{cond} t_{cond} (e^4 - d^4) \right] \\ &= 2.7 \times 10^{-9}\ \text{kg} \cdot \text{m}^2 \end{aligned} \,. \tag{4.40}$$

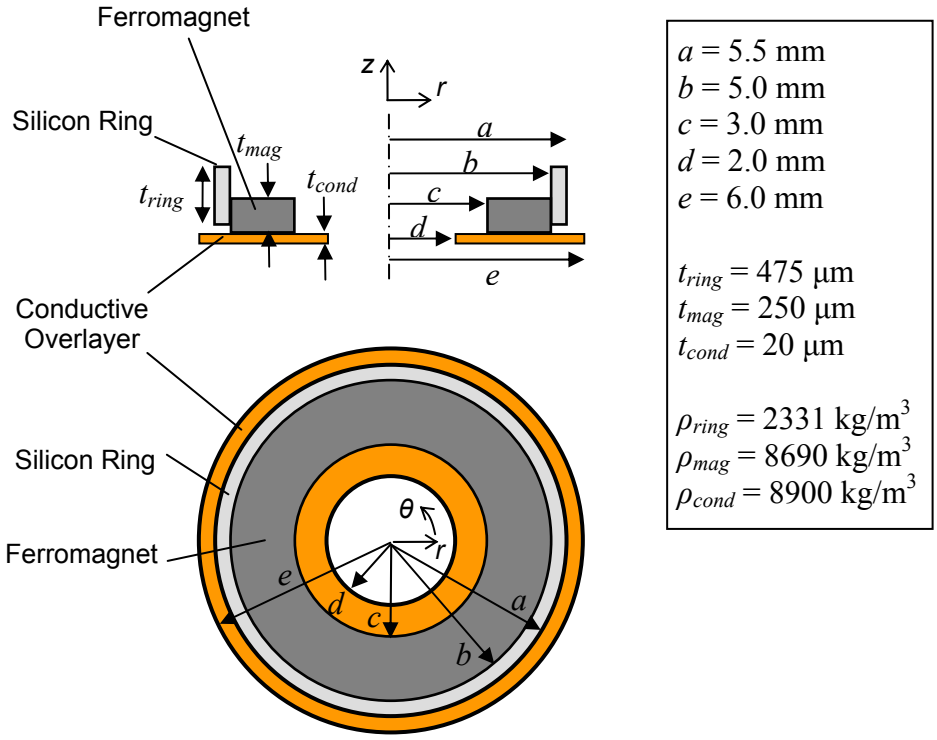

Figure 4.9 Top view and cross-section of tethered rotor.

4.3.3 Parametric Analysis

As can be seen from Equations 4.22, 4.25, 4.35, and 4.36, the stiffness coefficients, k_θ and k_z, are the critical parameters in the design of the tethers. The stiffness is dominated by the aspect ratio (height/width) of the beam. In general, a higher aspect ratio results in more compliant structure with a lower resonant frequency. On the other hand, a lower aspect ratio results in a stiffer structure with a higher resonant frequency. This indicates the need for long (l large), thin (w small), and tall (t large) tethers. However, the design space was limited by two fabrication constraints.

First, the tethers and silicon ring were to be etched from the thickness of one silicon wafer, and thus the tether thickness was fixed at t = 475 μm. Second, achieving tether widths, w, smaller than 20 μm (aspect ratio of >23) using DRIE posed a significant fabrication challenge. Thus, the only free parameters in the design of the tethered rotor are the number, width, and length of the tethers, N, w and l, respectively.

At maximum performance, the machine was estimated to generate electromagnetic torques on the order of 10 μN·m and pull-in forces of up to 1 N. Ideally, the machine should rotate at least several micrometers for accurate detection by the video capture/analysis system, but less than a tether width to avoid nonlinear dynamic behavior. Thus, a linear displacement of 0.1 μm per μN·m of torque seemed like a suitable design goal. At the silicon ring outer radius, a = 5.5 mm, this translated to an angular deflection of 1.8 x 10^{-5} rad per μN·m of torque, or a minimum compliance, of $g_\theta \geq 18$ rad/N·m (maximum stiffness of $k_\theta \leq 0.056$ N·m/rad). At resonance, $f_{0\theta}$, the effective spring stiffness would be considerably lower, and the angular displacement would be amplified by the quality factor, Q, which was expected to be between 10-100.

Additionally, to maintain a constant stator-rotor air gap and prevent rotor pull-in, the displacement in the z-direction should be minimized. The nominal air gap was designed to be from 25-75 μm, and deviations of up to 5 μm were considered tolerable. Thus, the compliance, g_θ, should have been less than 5 μm/N, or alternatively, $k_z \geq 0.2$ N/μm. Because the system was inherently much stiffer in the z-direction than in the θ-direction, the resonant frequency in the z-direction would be much higher, and resonant amplification was not expected to pose a problem.

Using Equations 4.22, 4.25, 4.35, and 4.36, the DC-compliance and resonant frequency in θ- and z-directions were plotted for various values of w (20-100 μm) and L (0-5 mm) for four-, six-, and eight-tether designs. Figure 4.10 shows an example plot for a six-tether design. From the plot, a design consisting of six, 40-μm wide, 2.5 mm-long tethers was selected to provide a radial compliance of 25 rad/N·m with an axial stiffness of 4.2 μm/N to prevent rotor pull-in. For small angular deflections, the rotation at the outer radius of the silicon ring could be approximated as a linear displacement with an effective linear compliance of 0.14 μm/μN·m. Table 4.1 summarizes the design and tabulates the projected mechanical properties.

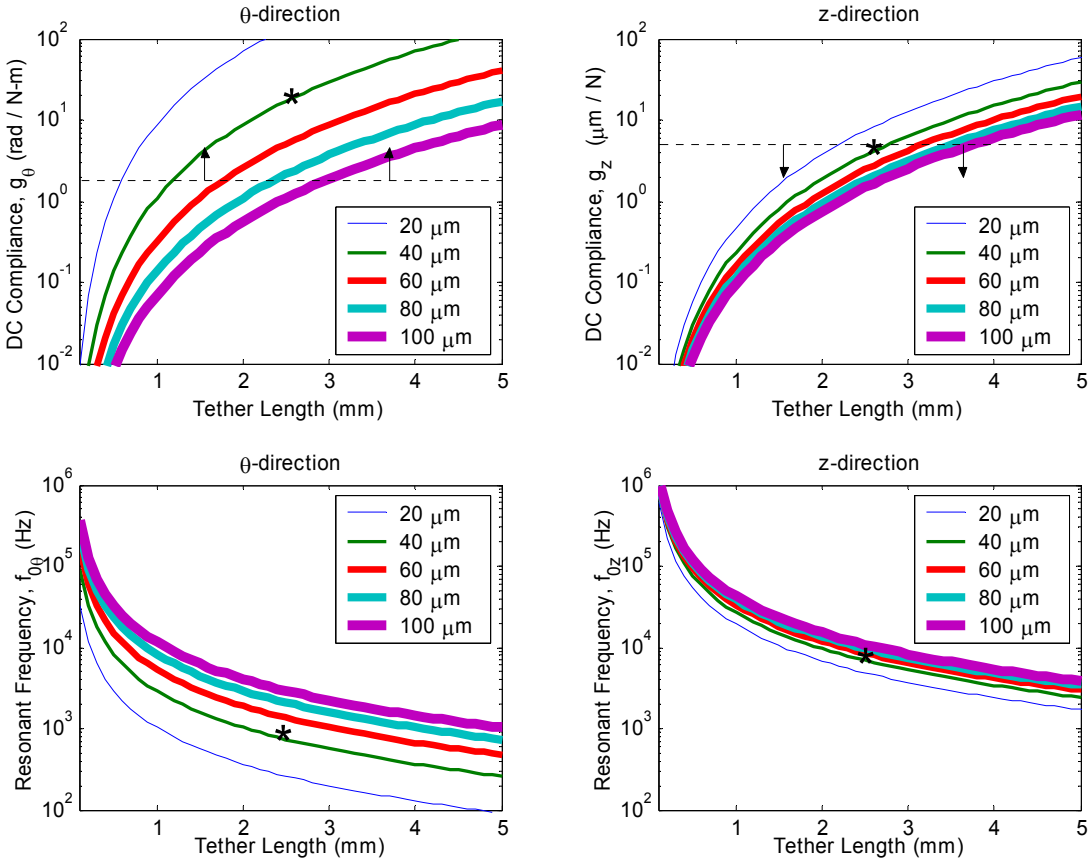

Figure 4.10 Projected DC-compliance and resonant frequency in θ- and z-directions for a six-tether design as a function of tether width, w (20-100 μm) and tether length, L (0-5 mm). The arrows indicate the desired performance range, and the asterisks indicate the selected design.

Table 4.1. Summary of mechanical tether design.

Parameter	**Symbol**	**Value**
Tethered rotor mass	m	145 mg
Tethered rotor moment of inertia	J	2.72 x 10^{-9} kg·m^2
No. of tethers	N	6
Tether height	t	475 μm
Tether length	L	2.5 mm
Tether width	w	40 μm
Outer radius of tethered ring	a	5.5 mm
θ-direction DC compliance	g_θ	25.5 rad/N·m
θ-direction resonant frequency	$f_{0\theta}$	605 Hz
z-direction DC compliance	g_z	4.18 μm/N
z-direction resonant frequency	f_{0z}	6450 Hz

4.4 Induction Machine Fabrication

The stators and tethered rotor structures were fabricated separately and ultimately clamped together for testing. All electrodeposition parameters can be found in Appendix A, and the mask layouts are shown in Appendix B.

4.4.1 Stator Fabrication

Stators were fabricated by embedding coils inside fusion-bonded silicon wafers and then building the magnetic core around the coils, as depicted by Figure 4.11. Processing began with two 500-μm thick, 100-mm diameter, low-resistivity (0.001 Ω·cm), n-type, <100> silicon wafers. Using the embedded metal process described in Section 2.1, electroplated Cu coils 300-μm wide and 35-μm thick were patterned into 70-μm deep cavities in two separate silicon wafers, as detailed in Figure 4.12. The coils were isolated from the silicon by a 400 nm Ta diffusion barrier and a 200 nm dry thermal SiO_2. Next, the two wafers were aligned and fusion bonded at 500ºC for 4 hr under vacuum ($<2x10^{-6}$ torr) with 200 kPa clamping pressure.

At this point the coils were totally encapsulated, and processing of the core was begun. First, a 3-μm PECVD oxide was deposited on both the top and bottom surfaces of the bonded pair. Using this oxide layer and photoresist as masks, nested deep silicon etches were performed from the bottom and top sides to form a silicon skeleton for the laminated core. The etches formed the hat, pole, and back iron layers with 100-μm wide trenches separated by 20-μm wide dividers, as shown in Figure 4.13 Then, using the partially filled lamination scheme described in Section 2.2, NiFe or CoFeNi was selectively electroplated onto the conductive silicon sidewalls to form the magnetic

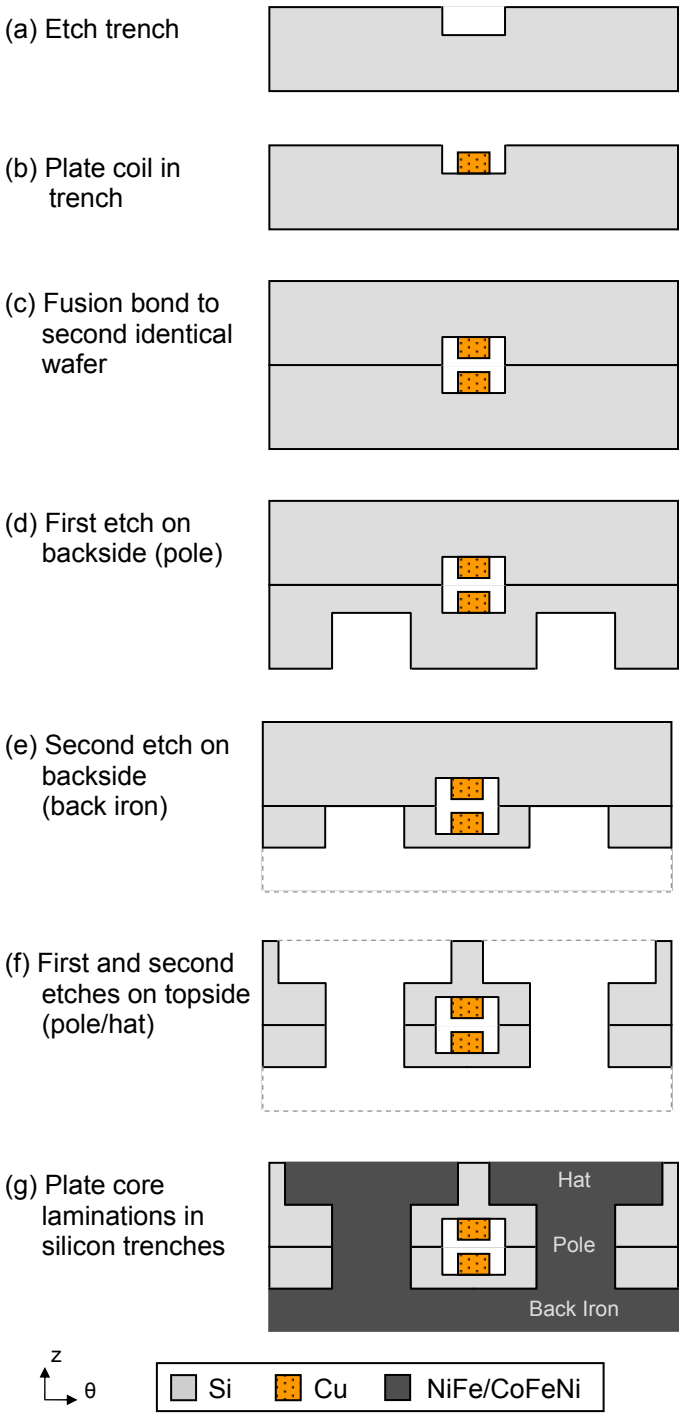

Figure 4.11. Simplified fabrication process flow for wafer-bonded induction machine stator, depicting cross-sections in θ-z plane: two coil conductors pass radially through the laminated core structure (laminations not shown).

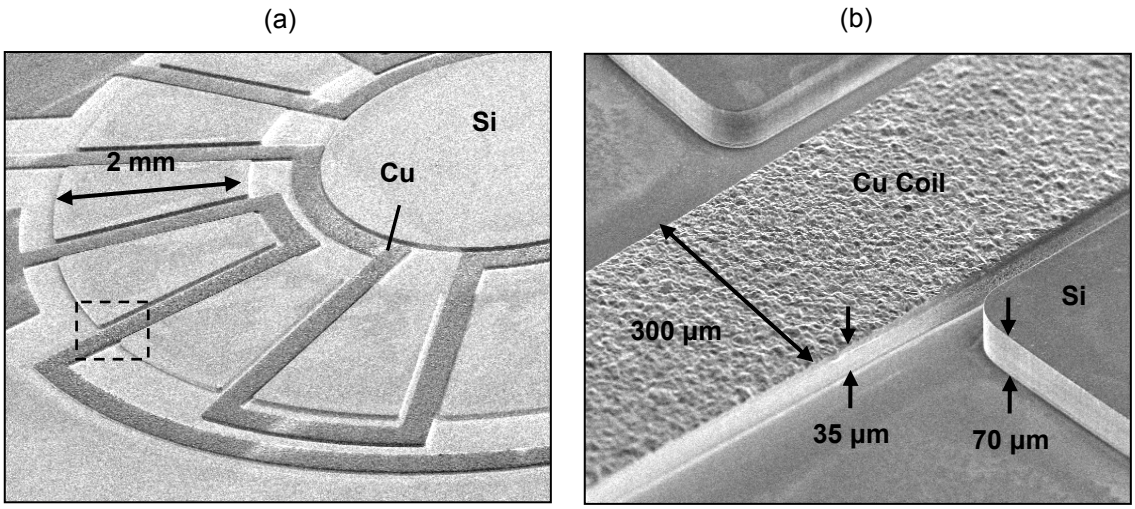

Figure 4.12. (a) SEM of 35 µm thick, 300 µm wide, copper coil recessed in 70 µm deep silicon cavity before wafer bonding to a second identical wafer; (b) Detail.

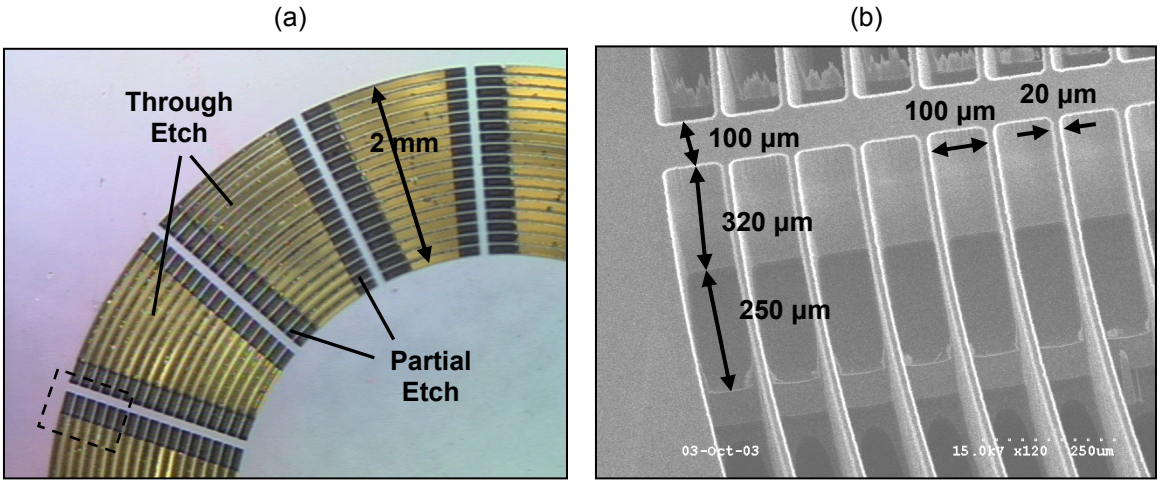

Figure 4.13. (a) Top-view image and (b) detail SEM of nested core etch, showing the partial etch for the hats and the through etch for the poles.

laminations. The metals plated only on the etched silicon regions, with the SiO_2 layer on the top and bottom surfaces acting as a mask.

Finally, contact openings were made from the top side by etching the silicon down to the buried coil contacts. The contact etch for the bottom coil opened a window permitting access to the top of the bond pads. Conversely, the etch for the top coil stopped on the SiO_2 on the backside of the bond pad, and the SiO_2 and Ta layers were subsequently removed to permit direct electrical contact to the Cu. The devices were then diced, resulting in a die measuring 30 mm x 30 mm x 1 mm.

Figure 4.14 shows images of the completed NiFe stator. From the external appearance, the lamination scheme seemed to have worked as expected. However, after all testing had been completed, both types of stators were cross-sectioned at an angle slightly off of the radial direction (along line A-A' in Figure 4.14b) in order to examine the etch and lamination profiles, as shown in Figure 4.15.

The hat, pole, and back iron layers measure 320 ± 5 μm, 335 ± 5 μm, and 345 ± 5 μm in thickness, respectively. The NiFe stator has reasonably uniform laminations of ~20 μm; the CoFeNi stator has poorer uniformity, with laminations of ~10 μm and pronounced keyholing at the top and bottom surfaces. In both cases, the uniformity is worse than previously observed (see Section 2.2), possibly due to the deeper trench depth (1 mm vs. 0.5 mm) and the highly three-dimensional nature of the stator core. Also, EDS analysis revealed nearly constant compositions of $Ni_{75}Fe_{25}$ and $Co_{34}Fe_{24}Ni_{42}$ when measured at various locations in the cross-section. However, it should be noted that the CoFeNi contains significantly less Co and more Ni than the expected composition of $Co_{52}Fe_{26}Ni_{22}$.

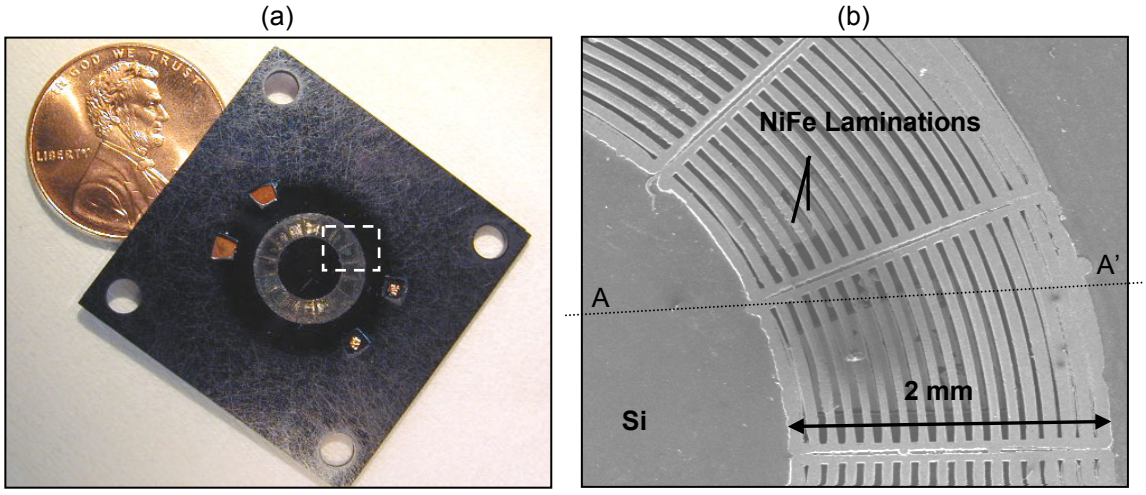

Figure 4.14. (a) Fabricated wafer-bonded, induction machine stator; (b) SEM of highlighted region showing 30 μm wide, 1000 μm tall, NiFe vertical magnetic laminations.

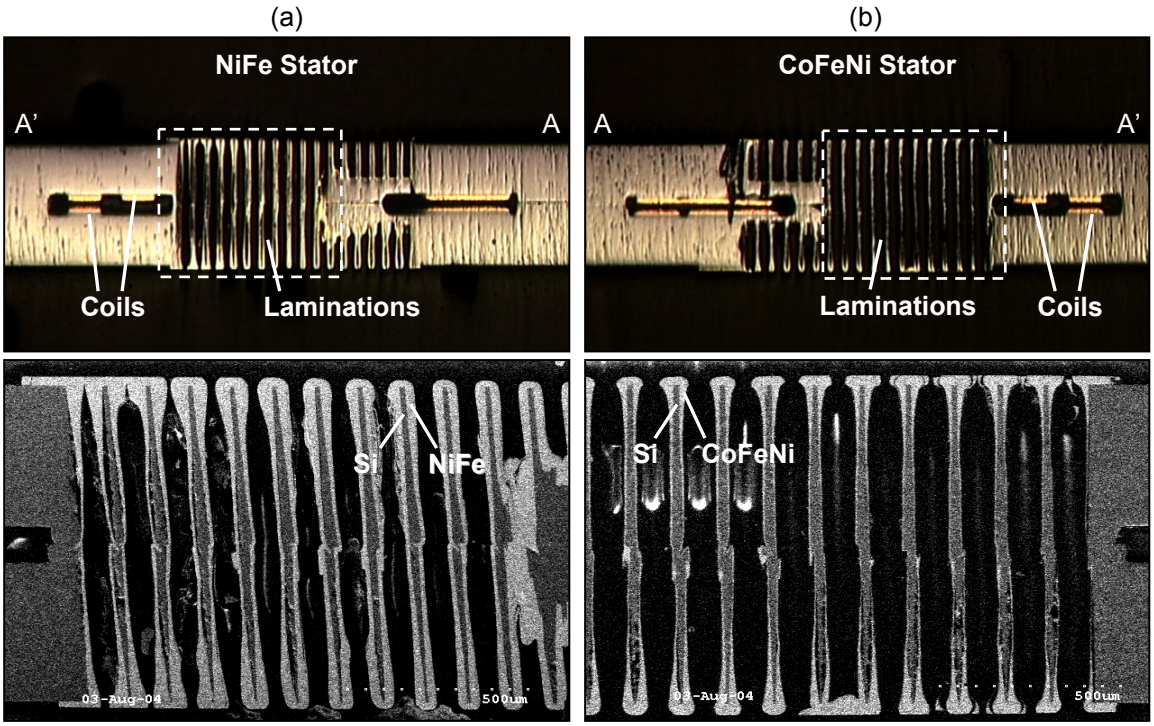

Figure 4.15. Cross-sections along A-A' (as shown in Figure 4.14b) for (a) NiFe and (b) CoFeNi induction machine stators.

4.4.2 Rotor Fabrication

For rapid prototyping, the rotors and silicon tether structures were fabricated separately and hand assembled. Rotors were built on a silicon substrate using multilevel electrodeposition in photodefined SU-8 molds [75], as shown in Figure 4.16. After sputtering a Ti/Cu seed layer, a 20-μm thick Cu annulus was plated, followed by a 250-μm thick NiFe or CoFeNi annulus, resulting in the structure shown in Figure 4.17. The SU-8 was then mechanically removed (peeled away), and the silicon substrate was etched away using KOH. The silicon tether structures, consisting of the radial tethers and central retaining ring, were formed separately by through-etching a wafer using DRIE, as shown in Figure 4.18. The rotors were subsequently glued into the ring for testing.

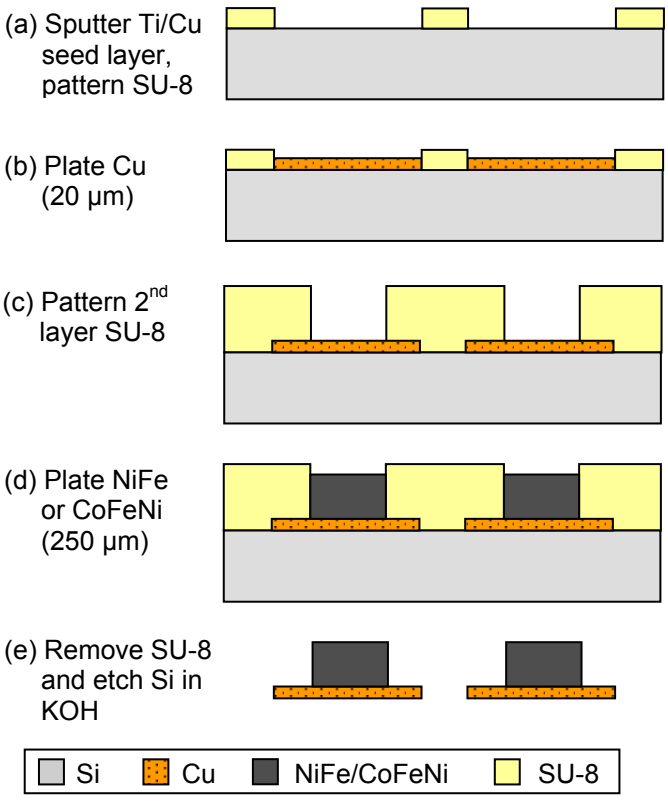

Figure 4.16. Process flow for induction machine rotors.

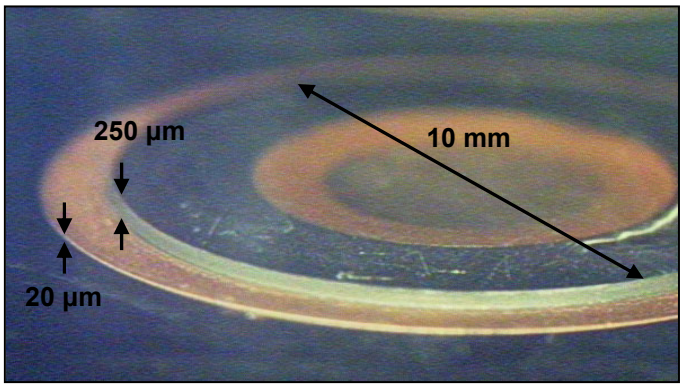

Figure 4.17. Photograph of electroplated induction machine rotor on Si substrate before release.

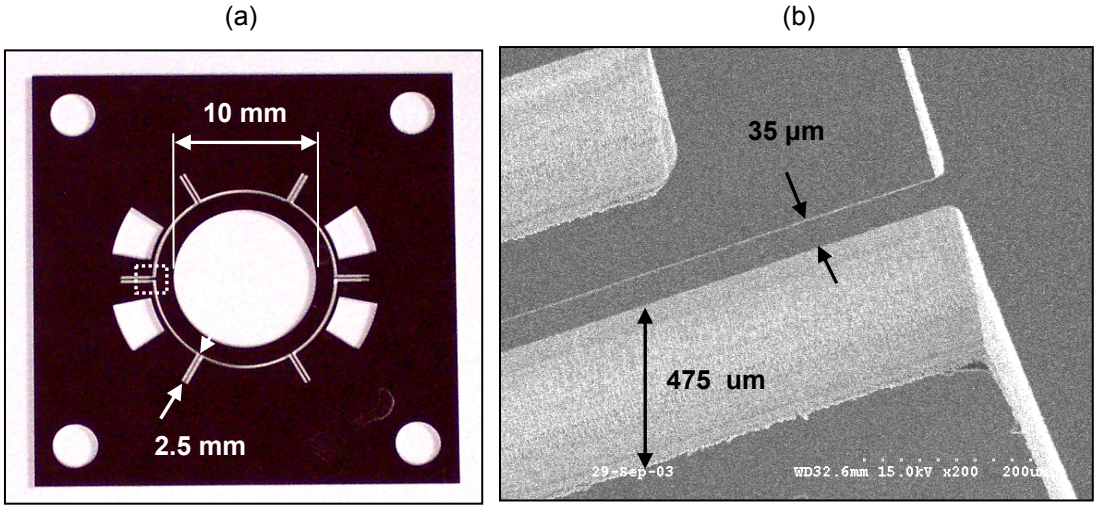

Figure 4.18. Induction machine (a) silicon tether structure and (b) detail of tether connection to central ring.

4.5 Induction Machine Characterization

After fabrication, the induction machines were characterized in three stages: (1) electrical measurements of the stators, (2) ferrofluid tests of the stator, and (3) tethered rotor torque measurements.

4.5.1 Stator Electrical Characterization

Resistance

The induction machine stators were initially characterized with electrical measurements. Four point resistance measurements of the coils indicated an average coil resistance of 0.20 Ω. With a cross-section of A = 35 μm x 300 μm, a total length of L = 110 mm, and an ideal resistivity of ρ = 1.7 μΩ·cm, the predicted resistance was

$$R = \frac{\rho L}{A} = \frac{(1.7\times10^{-8})(110\times10^{-3})}{(35\times10^{-6})(300\times10^{-6})} = 0.18\Omega\,. \tag{4.41}$$

Considering some variability in the conductivity and dimensions of the plated coils and that current crowding effects in the serpentine winding were not considered, the measurements agree reasonably well with the predicted values.

Inductance

Inductance measurements were also made from 1 kHz – 1 MHz using an HP4194 impedance analyzer. Figure 4.19 shows the frequency-dependence of each coil for both the NiFe and CoFeNi machines. The solid curves indicate the inductance of the stator alone, while the dashed curves indicate the inductance of the stator when the rotor was placed on the stator using a 25-μm thick Kapton spacer to simulate an operational air gap. Note that these measurements were conducted at low voltage/current, and did not capture saturation effects.

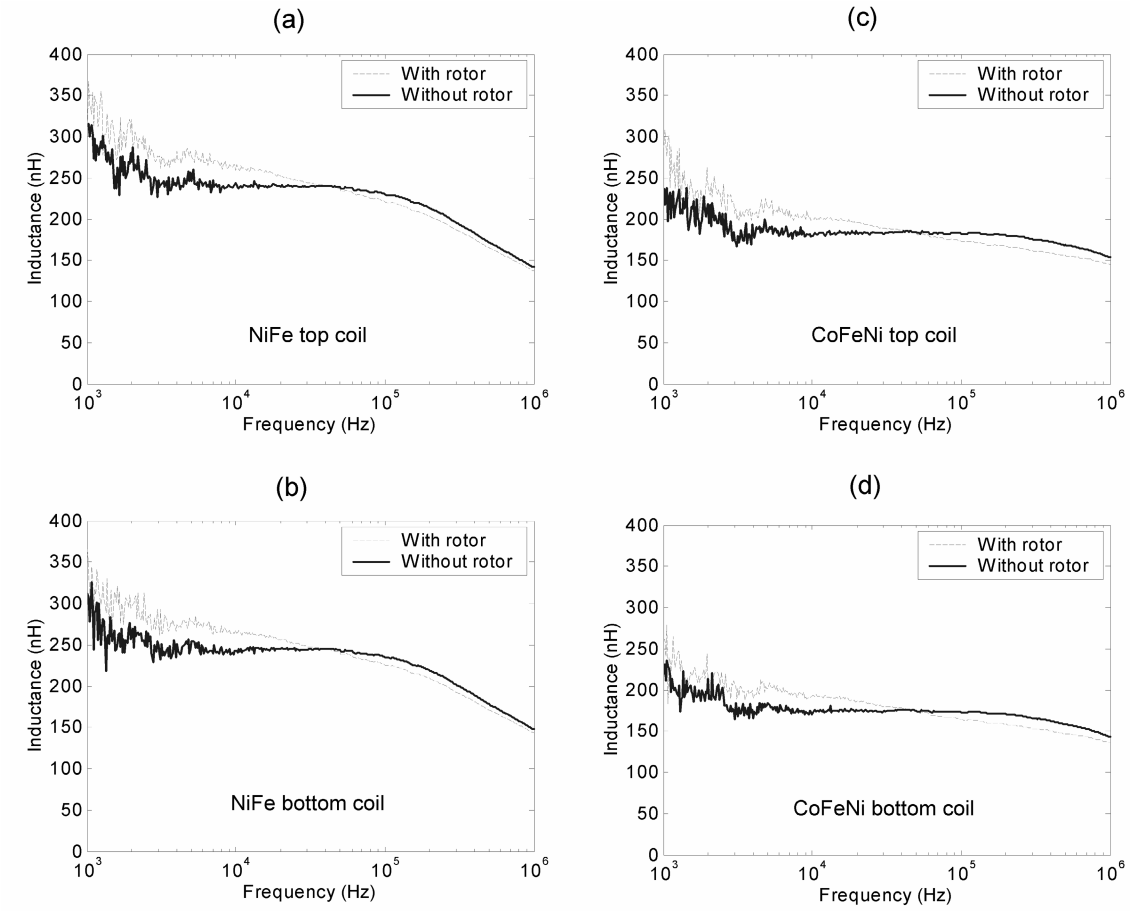

Figure 4.19. Inductance of induction machine stator coils with and without rotor. (a) and (b) are the NiFe top and bottom coils, respectively, and (c) and (d) are the CoFeNi top and bottom coils, respectively.

For both machines, the inductance without the rotor is seen to be fairly constant until ~100 kHz, upon which eddy currents induce a roll off. The roll off for the NiFe machine occurs at a slightly lower frequency than the CoFeNi machine, presumably because it has slightly thicker laminations, as noted from Figure 4.15. The addition of the rotor results in an increase in the low-frequency inductance, caused by an overall decrease in the total reluctance. In this case, the eddy current roll off occurs earlier because the rotor is not laminated. These measurements seem to indicate that the lamination scheme was working as expected.

4.5.2 Ferrofluid Tests

Before proceeding with the tethered rotor torque measurements, a ferrofluid—a colloidal suspension of sub-domain magnetic particles in a liquid (oil) carrier—was used to verify the full functionality of the stator. A small tub was constructed from a 500-μm thick ring of silicon glued to a 500-μm thick Kapton film. This tub was placed over the stator and filled with a thin layer of ferrofluid (Ferrotec Corp., Nashua, NH), as shown in Figure 4.20. The ferrofluid would react to the magnetic field gradients produced by the stator, similar to using iron filings.

By exciting the stator coils at low frequency (f_e = 1.5 Hz), both standing and traveling magnetic waves could be visualized by the naked eye. Standing waves were achieved by applying currents in-phase or 180° out of phase, and traveling waves were achieved by applying currents at ±90°. This technique enabled a simple and effective demonstration of the magnetic waves produced by the stator and verified the full functionality of the stator.

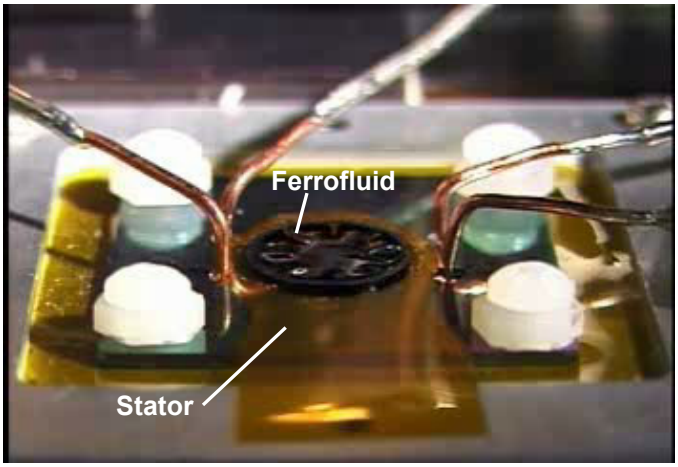

Figure 4.20. Ferrofluid tests showing traveling magnetic wave on the surface of the induction machine stator.

4.5.3 Tethered Rotor Torque Measurements

Using the tethered rotor test stand described in Section 4.3, machines were analyzed in motoring mode by varying the amplitude (2-8 A_{pk}) and frequency (2.5-55 kHz) of the excitation currents as well as the air gap (25-75 μm). A typical frequency response of the angular displacement from the microvision system is shown in Figure 4.21. The data is seen to closely follow a standard 2nd-order system, as expected.

For each test condition (i.e. current amplitude/frequency and air gap), the motoring torque was extracted as described in [23,29,31-34], by fitting a curve to the measured data and using the second-order response

$$T = J\ddot{\theta} + b\dot{\theta} + k\theta, \tag{4.42}$$

where T is the torque, θ is the angular displacement, J is the moment of inertia, b is the damping factor, and k is the spring coefficient. The resolution of the image analysis system was ~4 nm, corresponding to an angular resolution of 7.3 x 10^{-7} rad at a radius of

5.5 mm ($\theta \approx$ 4 nm / 5.5 mm). Based on a radial compliance of 25 rad/N·m, this corresponds to a torque resolution of 30 nN·m.

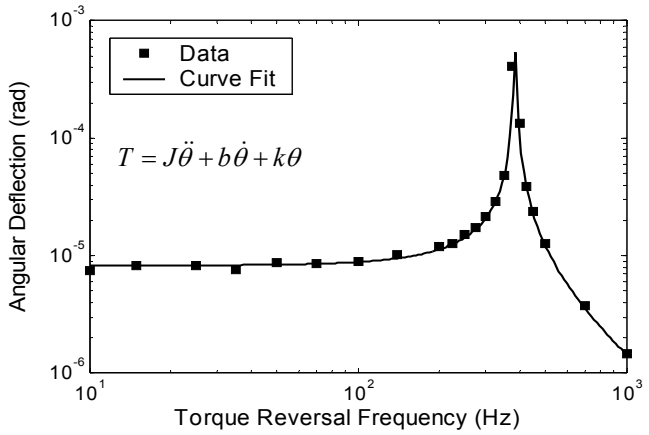

Figure 4.21. Example dynamic response of the tethered induction machine rotor as a function of the torque reversal frequency, showing measured data and a 2nd-order curve fit used to extract torque (T) from the angular deflection (θ).

The measured torques are plotted in Figure 4.22 as a function of excitation frequency and current for an air gap of 50 μm. The error bars indicate plus and minus one standard deviation, based on the accuracy of the curve fit to the dynamic response data. Corresponding theoretical curves, produced by MIT, are shown for reference. These plots represent torque-slip curves, as the machines were tested under blocked-rotor conditions ($\omega_m = 0 \rightarrow s = 1 \rightarrow f_r = f_s$). The data shows characteristic induction machine behavior. As the frequency increases, the torque rises fairly linearly to a maximum and then slowly tapers off. For both machines, the transition occurs around f_e = 20 kHz, corresponding to a slip frequency of f_r = 5 kHz.

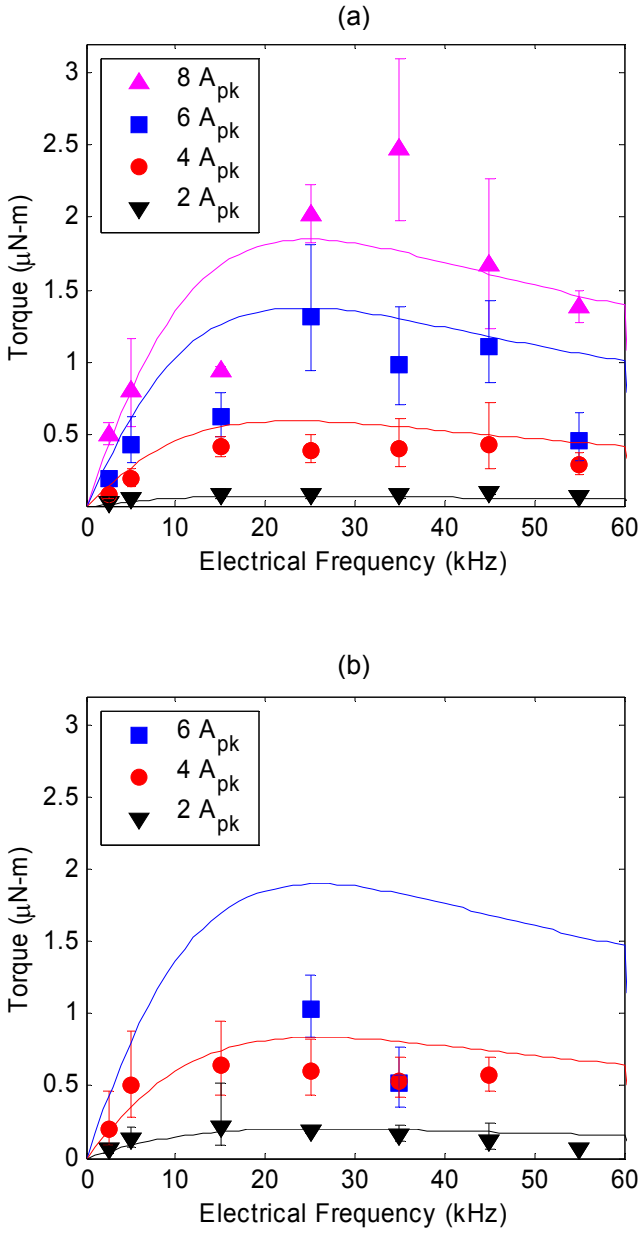

Figure 4.22. Torque vs. electrical frequency for (a) NiFe and (b) CoFeNi induction machines at 50 μm air gap. Measurements are indicated with points, and theory, with solid curves.

The NiFe machine shows a maximum torque of 2.5 μN·m at 8 A_{pk}, 35 kHz. Tests of the CoFeNi machine were corrupted at high currents by broken tethers, and only two valid data points were collected above 4 A_{pk}. Regardless, the CoFeNi machine demonstrated 1.0 μN·m at 6 A_{pk}, 25 kHz. In both cases, testing was limited to 8 A_{pk} (approximately 6.4 W per phase, for 0.2-Ω coil resistance) only because the displacement of the rotor became nonlinear and out-of-plane (pull-in and tilting) motion was noted, causing large inaccuracies in the torque extraction.

At low currents, where no magnetic saturation occurs, the torque should show a quadratic dependence with current; upon saturation, the torque should increase linearly, as predicted by Equation 4.10. Figure 4.23 plots the measured torque vs. the *square* of current. The data shows a quadratic relation, indicating that neither machine had fully saturated, even at 8 A_{pk} for the NiFe machine. Thus, higher currents may have been used to achieve more torque without saturation. At 8 A_{pk}, the current density in a coil was only ~8 x 10^8 A/m^2, well below the maximum current of 32 A_{pk} (3 x 10^9 A/m^2 current density). However, simulations from MIT [78] predicted that the NiFe machine should begin to saturate at ~6 A_{pk}, and the CoFeNi machine should not saturate until >8 A_{pk}.

Figure 4.24 shows the torque for the NiFe machine as a function of the air gap for three different current amplitudes at 35 kHz. Torque is seen to be maximized for the 50 μm air gap, and is explainable from MIT simulations as follows. As the air gap is increased, the inductive coupling between the stator is reduced, and the magnitude of the rotor eddy currents and the resulting torque are lessened. However, as the air gap is reduced, higher-order spatial harmonics from the traveling magnetic wave couple into the stator. These harmonics act as braking torques and reduce the net torque.

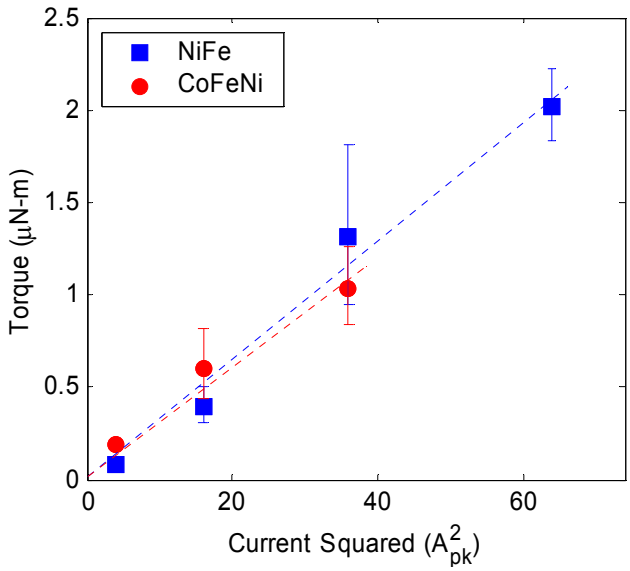

Figure 4.23. Measured torque vs. square of stator current for NiFe and CoFeNi induction machines at 25 kHz and 50 μm air gap.

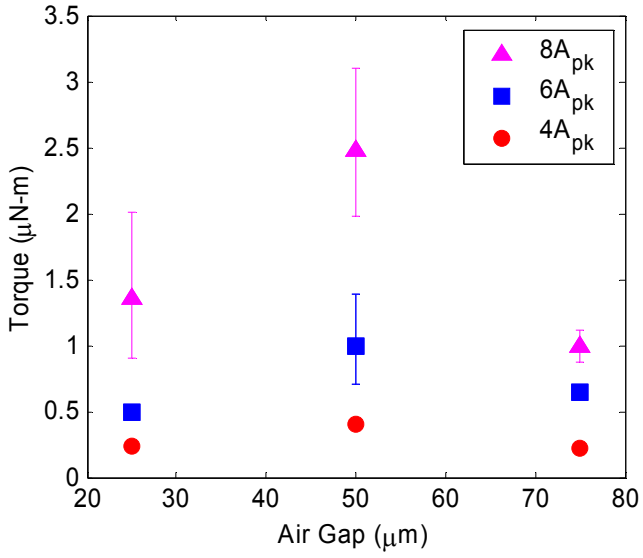

Figure 4.24. Measured torque vs. air gap for NiFe induction machine at 35 kHz.

4.6 Induction Machine Summary

The successful development of laminated, fusion-bonded, Si-based magnetic machines represent significant progress toward a fully integrated microengine system. The materials, structure, and fabrication processes used are compatible with the microturbine devices and offer the potential for much higher operating temperatures. Thus, direct integration of a magnetic machine with a microturbine now seems feasible.

The machines were characterized using tethered rotor torque measurements, and maximum torques of 2.5 and 1.0 μN·m were achieved for the NiFe and CoFeNi machines, respectively. For active machine volumes of 75 mm^3 (10 mm, 6 mm ID, 1.5 mm thick), this corresponds to measured torque densities of 33 and 13.2 $N{\cdot}m/m^3$, respectively. The torque measurements were made under a blocked rotor condition, so technically no steady mechanical power was produced. However, if the machines produced the same 2.5 and 1.0 μN·m torques at the design speed of 1 Mrpm ($\omega_m \approx 1 \times 10^5$ rad/s), this would correspond to motoring powers of 0.25 and 0.1 W, respectively.

Also, while not measured, the coils should support currents of at least 32 A_{pk}, (3×10^9 A/m^2 current density), four times the experimental data. At this level, and assuming no saturation, the machines would exhibit a 16x improvement in torque, ~40 μN·m and potentially 4 W of mechanical power if 1 Mrpm were achievable. Even in the worst case, assuming the machine cores saturated at 8 A_{pk}, the torque would still grow linearly with current, and at 32 A_{pk}, the machines would exhibit ~10 μN·m. These numbers are in line with the system design goals and represent improvement over previous induction machine designs [31,32,34,35].

It was also believed that the machines were limited by several fabrication issues. First, the teeth gaps between adjacent poles on the upper surface of the stator core are partially closed over due to overplating of the laminations. This partially shorts out the magnetic flux path between the stator and rotor and limits torque production. Second, as can be seen from the cross-sections in Figure 4.15, the laminations were quite thin, resulting in a poor core packing density and poor overall torque production. An attempt was made to divide the overplating in between the stator teeth using an infrared laser cutting system, but the laser inadvertently cut too deep and damaged the embedded coils, ruining the machines. The cut is actually clearly shown on the left side of Figure 4.15b.

Rebuilding the system with higher lamination packing densities, larger coils, and, in general, more aggressive fabrication could improve the torque and overall performance, however the potential performance improvement must be weighed against the complexity of the fabrication. This led to the investigation of alternative machine configurations, as discussed in Chapter 5.

CHAPTER 5

PERMANENT MAGNET MACHINES

As an alternative to induction machines, permanent magnet (PM) generators were investigated for potential use in the silicon microengine. One major advantage of a PM machine is the inherently "free" source of magnetic flux. As compared to an induction machine, which requires some initial input electric power to create the induced fields in the rotor, a PM rotor contains a permanent source of flux and requires no electrical power for creation of fields in the rotor. Thus, a microscale induction machine must be designed with great care in order to exceed the "break even" point for net power generation, whereas even a crudely built PM machine is capable of net power generation.

One potential disadvantage of a PM machine is that more complex power electronics may be required to support synchronous operation under varying loading conditions, as compared to the asynchronous induction machine. Also, the power density of a PM machine is primarily limited by the magnetic field strengths of the PM materials used, whereas an induction machine is limited by the saturation densities of the ferromagnetic materials and maximum current densities in the windings. However, as the size of machine is reduced, scaling laws indicate more favorable power densities for PM machines rather than induction machines [76].

PM machines were not originally considered for the microengine concept, because the high temperatures were expected to be beyond the useful operating range for many PM materials (e.g., ferrites and NdFeB). Also, there were significant fabrication concerns for integrating and magnetizing PM materials such as alnicos or SmCo. Another concern was the brittle nature of high-performance PM materials, considering

the mechanical strength requirements needed for high-speed rotation. However, it has since been shown that integrating any metallic material (hard or soft magnet) in the silicon turbine presents a substantial design challenge. Thus, the potential payoff in performance for PM power generation could not be overlooked, and the decision was made to investigate PM machines in parallel with the induction machines, while continuing to tackle the integration challenges.

Thus, this chapter presents the design, fabrication, and characterization of high-speed PM generators. A spinning rotor test stand was built using an air-driven spindle and was used to successfully demonstrate watt-level electric power generation. It should be again noted that the design, fabrication, and characterization were a joint effort between MIT and Georgia Tech.

5.1 PM Machine Design

PM machines operate by direct magnetic induction governed by Faraday's Law,

$$\oint_C \vec{E} \cdot d\vec{l} = -\iint_S \frac{\partial \vec{B}}{\partial t} \cdot d\vec{S} . \tag{5.1}$$

A multi-poled PM rotor provides time-varying magnetic flux that induces a voltage, E, on each winding of the stator. The voltage is proportional to several design parameters [71],

$$E \propto pN\phi\omega_m , \tag{5.2}$$

where p is the number of poles, N is the number of winding turns per pole, ϕ is the flux in a single pole, and ω_m is the mechanical speed. A planar layout, with axially directed flux and similar in size to the previously discussed induction machines, was thus investigated. High power and efficiency were the top priorities, but, like the induction

machines, the PM machines were designed with consideration for eventual integration within a silicon microengine (fabrication, materials, geometry, etc.).

The magnetic flux within a PM machine is dependent on the reluctance of the equivalent magnetic circuit and can be maximized by using highly permeable ferromagnetic back irons and/or a small air gap. From initial analyses by MIT, it was determined that the fields from suitably sized permanent magnets were strong enough to permit air gaps of several hundred microns. This enabled the examination of surface wound stators, which are similar to the previous induction machine stators, but the windings occupy space in the air gap on the surface of the stator rather than in stator slots. This design change eliminated the need for embedding the coils within the stator teeth, and in fact, eliminated the stator hats or poles altogether, greatly simplifying the fabrication process. This permitted the fabrication of much more complex, interleaved windings, similar to those used in conventional macroscale machines [71]. Multi-phase, multi-turn windings could be constructed using only two metallization layers patterned on the flat stator surface. These complex coils, with small inter-conductor gaps and variable width geometry, were, in fact, a key enabler for high power output.

Thus, PM generators were designed as three-phase, eight-pole, synchronous machines, each consisting of a surface-wound stator and a multi-poled PM rotor. The stator, with an active area of 9.525 mm OD and 5.525 mm ID, consists of three Cu surface windings on a 1-mm thick $Ni_{80}Fe_{15}Mo_5$ (Moly Permalloy) ferromagnetic substrate. The coils were dielectrically isolated from the substrate by a 3 μm spin-on-glass layer and/or 5 μm polyimide layer. NiFeMo was selected as the substrate material for its combination of high permeability ($\mu_r > 1x10^4$) to minimize reluctance of the stator,

low coercivity (H_c ~ 0.16 A/m) to minimize hysteresis losses, and commercial availability in sheets of suitable thickness [72].

As shown in Figure 5.1, three different winding patterns (1-turn, 2-turn, and 4-turn per pole) were developed to explore tradeoffs in performance and fabrication complexity. The 1- and 2-turn designs use simple single-layer windings with "crossovers" on the inner and outer end turns, while the 4-turn design uses a full double-layer winding with more complicated end turns. For all three winding types, the radial conductors vary in width from 225 μm at the inner radius to 550 μm at the outer radius, with a 130 μm gap between adjacent radial conductors. The end turns of the 1- and 2-turn designs have a minimum feature size of 100 μm and a minimum gap of 160 μm, while the end turns of the 4-turn machine have a minimum feature size of 40 μm and a minimum gap of 40 μm. The number of vias required is proportional to the number of turns; the 1-, 2-, and 4-turn designs use 16, 32, and 64 vias per phase, respectively.

The rotor was designed using an annular multi-poled rare-earth Sm_2Co_{17} PM and a ferromagnetic $Fe_{49}Co_{49}V_2$ (Hiperco 50) back iron, each 9.525 mm (3/8 in.) OD, 3.175 mm (1/8 in.) ID, and 500 μm thick. The 3.175 mm ID of the rotor is slightly smaller than the 5.525 mm ID of the stator, because that was the size of commercially available SmCo magnets. The use of a solid rotor annulus will ultimately permit higher rotational speeds as compared with discrete pole pieces, as demonstrated in low-speed microgenerators [46]. However, this required the development of a method for selectively patterning magnetic poles onto the rotor, as discussed in Section 5.4. For characterization, the rotor components were mounted to an adaptor on a 1.6-mm shaft, as shown in Figure 5.2, and spun using an air-driven spindle, as discussed in Section 5.3.

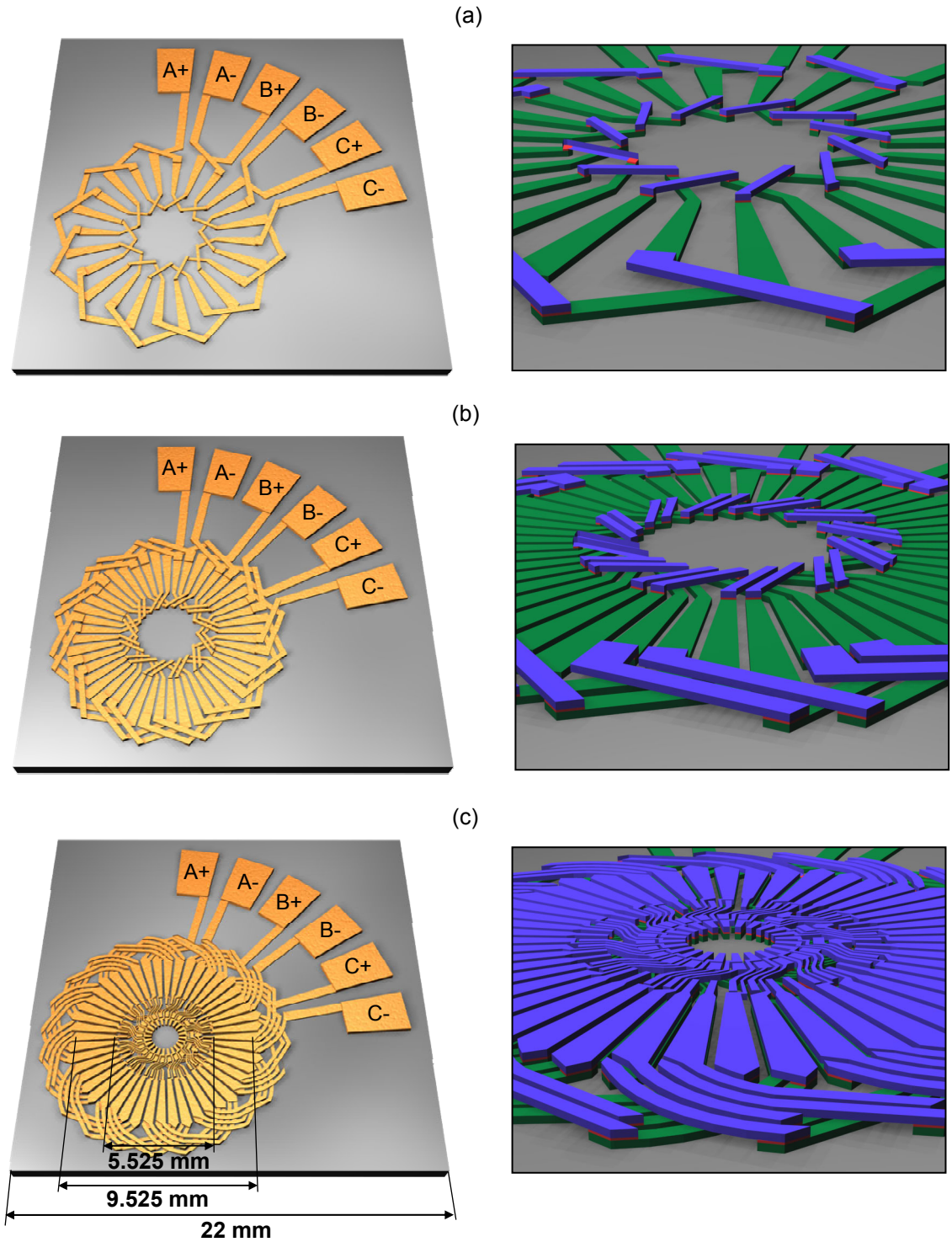

Figure 5.1. Conceptual drawings of (a) 1-turn, (b) 2-turn, and (c) 4-turn per pole surface wound PM machine stators.

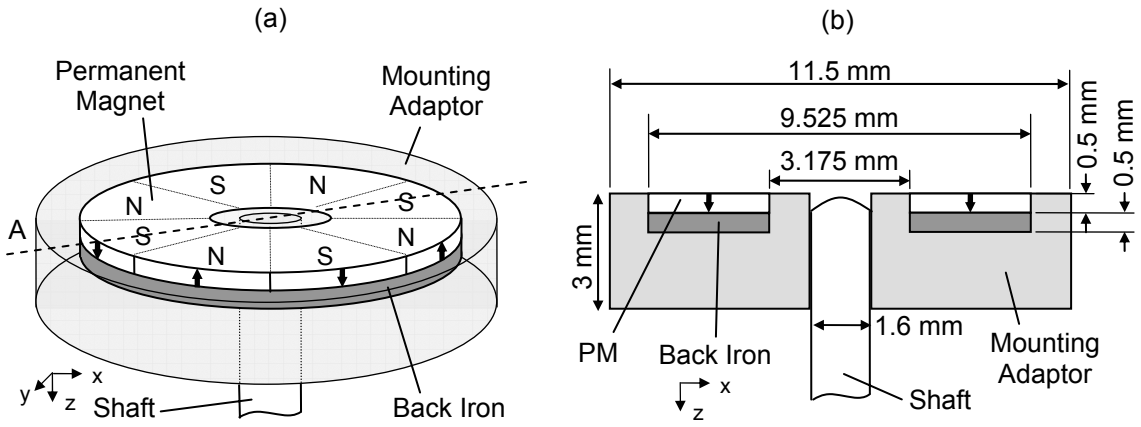

Figure 5.2. Schematic (a) perspective view and (b) cross-section of permanent magnet machine rotors. Note rotor is shown upside down.

SmCo was selected as the PM for its combination of high operating temperatures (T_c > 700°C, T_{max} > 300°C); large remanence (B_r ~ 1.1 T), coercivity (H_c ~ 840 A/m), and maximum energy product (BH_{max} ~ 240 kJ/m^3), for high energy conversion; and corrosion resistance [77]. NdFeB could have been used, offering higher remanence (B_r ~ 1.4 T), coercivity (H_c ~ 820 A/m), and maximum energy product (BH_{max} ~ 400 kJ/m^3), but it does not provide high enough operating temperatures (T_c ~ 300°C, T_{max} ~ 150°C) for eventual integration within a combustion-driven microengine [77]. FeCoV was selected as the back iron material for its combination of high saturation flux density (B_s ~ 2.4 T) to prevent saturation and reasonably high permeability (μ_r > 3000) to minimize reluctance [72]. Hysteresis was of little concern since the fields in the rotor are nearly constant.

5.2 PM Machine Modeling

Like the induction machines, extensive modeling was performed for the PM machines by colleagues at MIT [78], and only the key results are included here. The

machines were analyzed at a given radius by solving 2-D Maxwell's equations in the magneto-quasistatic regime for the angular distribution of vector magnetic potential and resulting incremental flux. The incremental fluxes were then integrated over the radial span of the machine to determine the total flux produced by the rotor and consequently the induced emf in the windings. Then, using the induced emfs as sources, PSpice circuit models were used to model the machine and power electronics.

A general per-phase circuit model for the synchronous generator [71] is shown in Figure 5.3, and the corresponding power flow diagram shown in Figure 5.4. The total mechanical input power, P_i, drawn from the turbine is distributed three ways. First, some power is lost due to frictional losses, P_{rot}. Second, some power, P_{core}, is lost due to hysteresis and eddy currents induced in the stator. The power that remains is converted to electrical energy via magnetic induction, denoted by P_e. The remainder of the losses are electrical losses, dependent on the current, I_l, flowing in the winding. First, is the conduction loss, P_{cond}, due to the finite resistance, R_{cond}, of the machine winding. Second, are the losses due to the finite contact resistances and other losses in any intermediate power electronics, $P_{circuit}$, accounted for by resistor $R_{circuit}$. Finally, what power remains, P_o, is delivered to the load, R_l.

Note the core loss, P_{core}, is due to the time-varying magnetic field in the stator, primarily from the permanent magnets, and that this loss is present even in an open circuit condition. It should also be noted that the magnetic field varies slightly as a function of the current flowing in the winding due to the opposing armature reaction fields. However, for the machines geometries of interest, simulations by MIT [78] show that the relative reduction in the total field due to this effect is quite small, and thus core

loss can be considered independent of the current. A corollary implication is that, at a constant speed, the fields, and hence winding emfs, do not decay as a function of current.

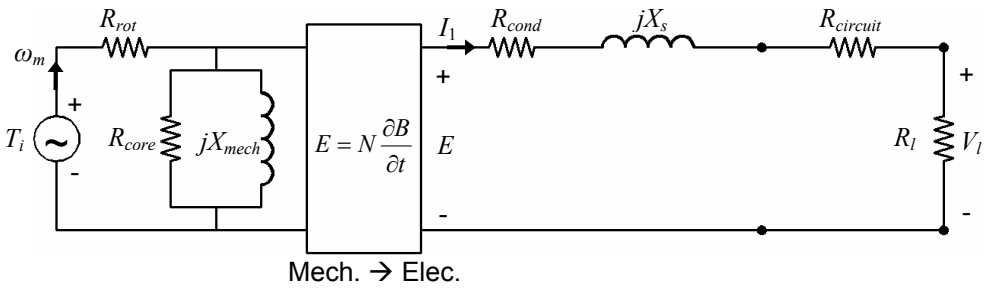

Figure 5.3. Per-phase synchronous PM generator circuit model.

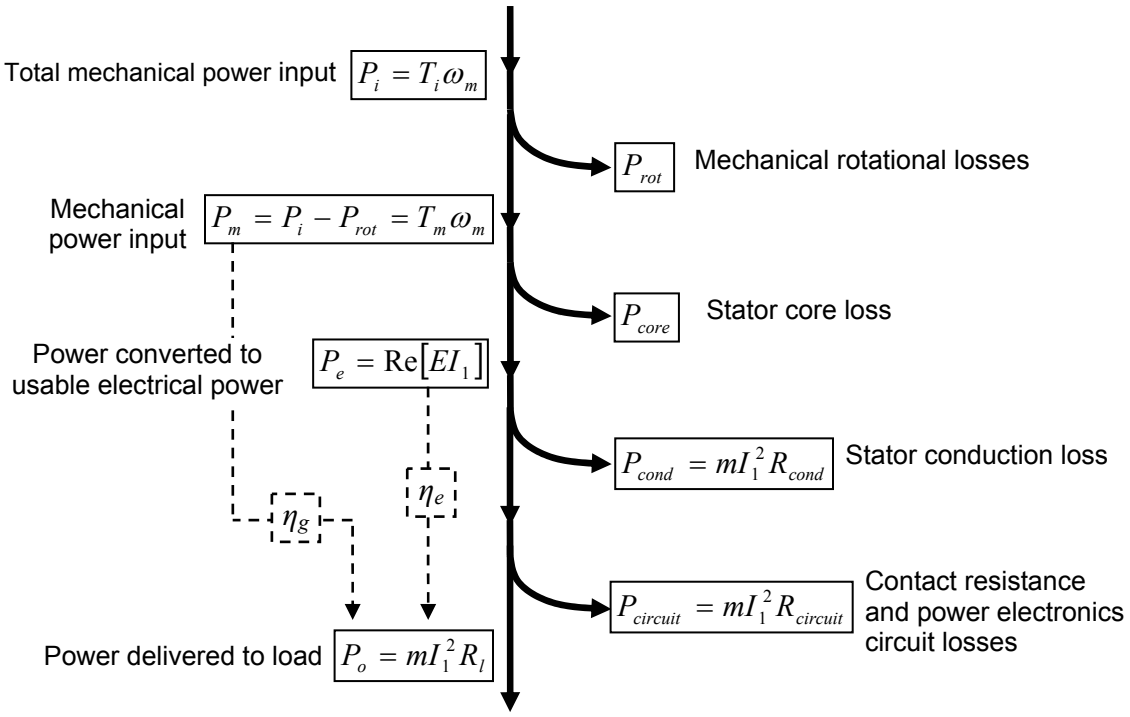

Figure 5.4. Power flow for *m*-phase PM machine in generating mode.

In the system level microengine design, the mechanical losses, P_{rot}, due to windage, bearing losses, etc. are assumed as part of the mechanical turbine design and are accounted for in the mechanical power budget. Thus, the generator power budget starts from the mechanical shaft power input, P_m. Thus, core loss, P_{core}, and the overall electrical efficiency are important to the design. The overall generator mechanical-to-electrical efficiency, η_g, is given by

$$\eta_g = \frac{P_o}{P_m}. \tag{5.3}$$

The corresponding electrical efficiency, η_e, given by

$$\eta_e = \frac{P_o}{P_e}, \tag{5.4}$$

excludes the stator core loss and only addresses the electrical efficiency of the machine.

To first order, the electrical efficiency can be analyzed by simplifying the electrical portion of the circuit shown in Figure 5.3. By assuming $R_{circuit} = 0$, and ignoring all imaginary components, the machine can be modeled by a per-phase equivalent Thevenin circuit consisting of a source voltage, V_s, and source resistance, R_s, connecting to a resistive load, R_l, as shown in Figure 5.5. For compactness, let $R_l = kR_s$.

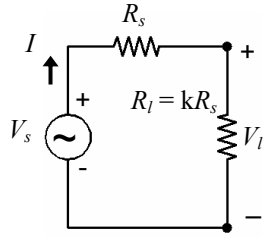

Figure 5.5. Simplified per-phase Thevenin equivalent PM machine model.

Thus, the input electrical power is given by

$$P_e = \frac{V_s^2}{(R_s + R_l)} = V_s^2 \frac{1}{(R_l + R_s)} = \frac{V_s^2}{R_s} \frac{1}{(k+1)}, \tag{5.5}$$

and the output power is

$$P_o = \frac{V_l^2}{R_l} = V_s^2 \frac{R_l}{(R_l + R_s)^2} = \frac{V_s^2}{R_s} \frac{k}{(k+1)^2}, \tag{5.6}$$

with electrical efficiency given by

$$\eta_e = \frac{P_o}{P_e} = \frac{k}{(k+1)}. \tag{5.7}$$

Maximum power transfer occurs for $k = 1$ at 50% efficiency, and

$$P_{o_{\max}} = \frac{V_s^2}{4R_s}. \tag{5.8}$$

Finally, output power normalized by the maximum power is given by

$$\frac{P_o}{P_{o_{\max}}} = \frac{4k}{(k+1)^2}, \tag{5.9}$$

The normalized output power and efficiency from Equations 5.5 and 5.7 are plotted in Figure 5.6, and represent the normalized machine performance as function of the load resistance. As can be seen, there is a tradeoff between output power and efficiency. Higher load resistances improve efficiency, but reduce output power. For example, a generator required to operate at 90% efficiency (k=9) can only output 36% of its theoretical maximum power. This concept is important for the successful future implementation of a microengine system, where both efficiency and output power are critical design requirements. To better illustrate the tradeoff, the product of output power

and efficiency is also shown in Figure 5.6. From the curve, a load resistance of ~2R_s is shown to yield the best tradeoff between efficiency (67%) and power (89% of P_{max}).

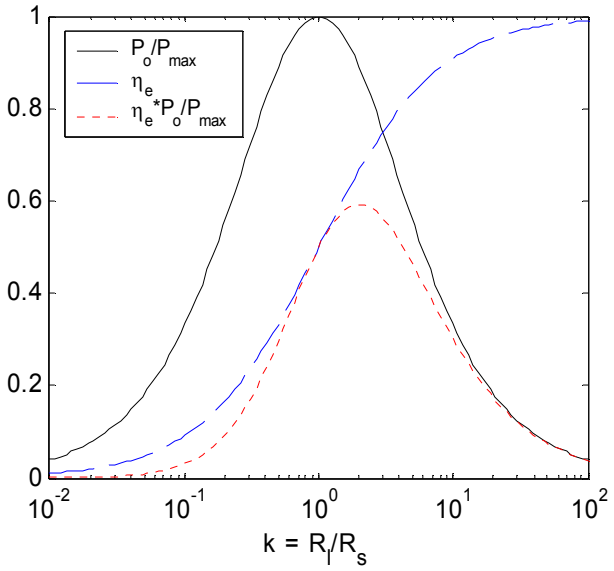

Figure 5.6. Normalized output power, P_o/P_{max}, and electrical efficiency, η_e of PM generator as a function of load resistance, R_l.

5.3 Spinning Rotor Test Stand

For characterization of the PM machines, a test stand that supported spinning, rather than tethered, rotors was developed to enable mechanical-electrical power generation while avoiding the design and fabrication complexities of air bearings and integration within an all-silicon microengine structure. This temporarily decoupled the magnetic generator design from the complex microengine system level design and integration issues.

The test stand incorporated a high-speed air-driven spindle to spin rotors with a controllable air gap over the surface of the stators, as depicted in Figure 5.7. A commercially available hobbyist carving tool, known as the Turbocarver (High Speed

Carving and Engraving Products, Federal Way, WA), was selected for use. Powered by compressed nitrogen, the spindle provided rotational speeds in excess of 350 krpm (>1/3 of microengine design speed). The device was designed to accept 1.6 mm (1/16 in.) diameter friction-grip burs (bits); thus, rotors were designed for attachment to shafts for mounting in the spindle. The rotational speed was found by monitoring an optical shaft encoder or, in the case of electrical machine tests, by the frequency of the generated output.

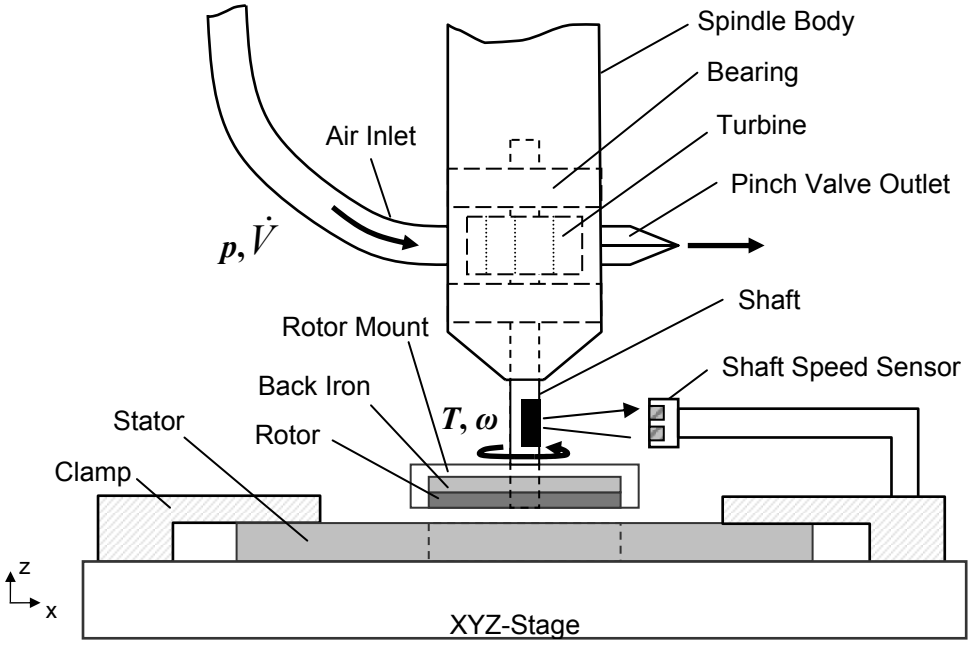

Figure 5.7. Schematic of spinning rotor test stand.

The shaft speed encoder was implemented by marking half of the shaft black and using a GP2L22 reflective photointerrupter (Sharp Microelectronics, Osaka, Japan). The photointerrupter is an infrared photoemitter-phototransistor pair, configured in the circuit shown in Figure 5.8. V_{cc} was set to ~6.7 V to achieve the maximum rated current (50 mA) through the emitting diode. The alternating high and low reflectance created an

output signal with frequency dependence on shaft speed. The signal was monitored using a frequency counter or spectrum analyzer. This scheme minimized the sensitivity to sensor range or position, which would cause a change in signal amplitude, but not frequency. The frequency of the photointerrupter signal at a maximum rotational speed (400 krpm) corresponded to a signal of 6.7 kHz, well within the 10 kHz bandwidth of the sensor. However, the output signal was seen to vary from 1.1 V_{p-p} at 1 kHz (60 krpm) to 0.68 V_{p-p} at 5.8 kHz (350 krpm).

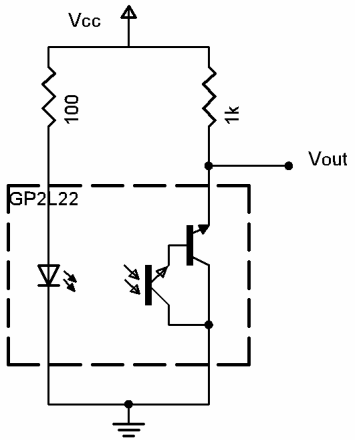

Figure 5.8. Spinning rotor shaft speed detection circuit.

One challenge with this system was the ability to precisely position the rotor over the surface of the stator while maintaining a uniform air gap. This required not only good registration between the rotor and stator, but also fine control over the angle between the rotor and stator. Registration of the rotor and stator in the x-y plane was not too critical, considering the machine has annular radial span of 2 mm and small misalignments were not expected to have a significant effect. The more critical alignment was achieving a uniform air gap, which, assuming a rigid rotor, was corrupted by three sources of

misalignment. As shown in Figure 5.9, these include rotational axis misalignment, rotor-to-shaft mounting misalignment, and runout ("play" at the end of the shaft) caused by bearing play and dynamic loads.

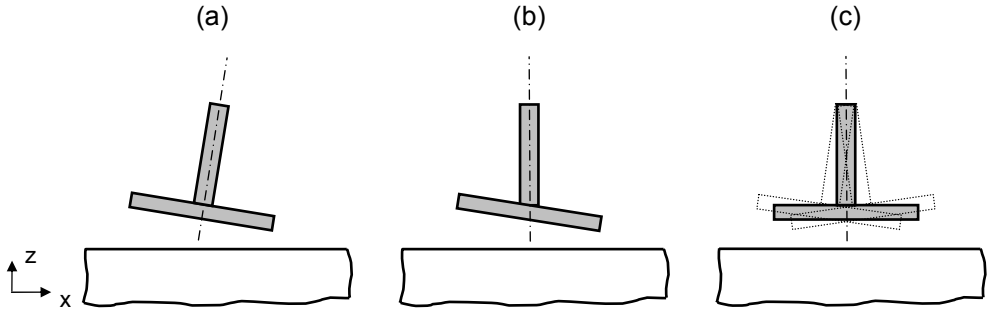

Figure 5.9. Three idealized sources for non-uniform rotor-stator air gap: (a) rotational axis misalignment, (b) rotor-to-shaft mounting misalignment, and (c) runout caused by bearing play and dynamic loads.

The angle between the rotor and stator, is given by $\alpha = \tan^{-1}(d / D)$, where d is the total non-uniformity and D is the rotor diameter, as depicted in Figure 5.10. To achieve ±25 μm uniformity (d = 50 μm) across an interface of D = 10 mm, required a cumulative misalignment angle of less than $\alpha_{max} = 0.3°$. Obviously, efforts were made to minimize rotational axis misalignment and rotor-to-shaft misalignment during mounting of the rotor to the shaft. The dynamic misalignment caused by tip runout was expected to be small—the runout for the Turbocarver was specified at <0.5 mil (12.7 μm) for a 10 mm long shaft, corresponding to $\alpha = 0.07°$. Thus, efforts were focused on developing a mounting scheme that permitted precise control of registration and incident angle between the rotor and stator.

In practice, the stator was clamped to an xyz-micropositioner stage, having ±5 μm resolution in all three directions, as shown in Figure 5.11. Rotors were mounted to a

shaft and inserted into the spindle, which was attached to an articulating arm providing translation and rotation in all directions.

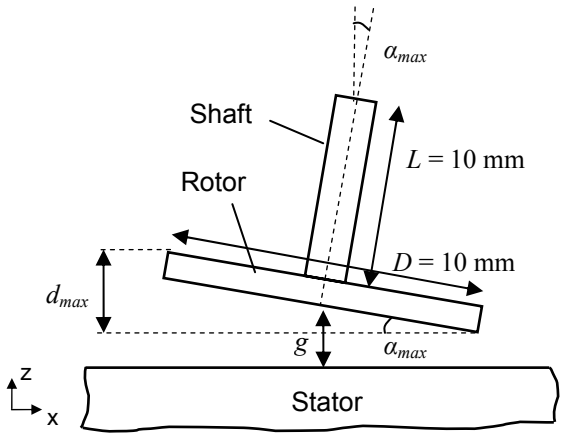

Figure 5.10. Schematic of rotor-stator air gap misalignment.

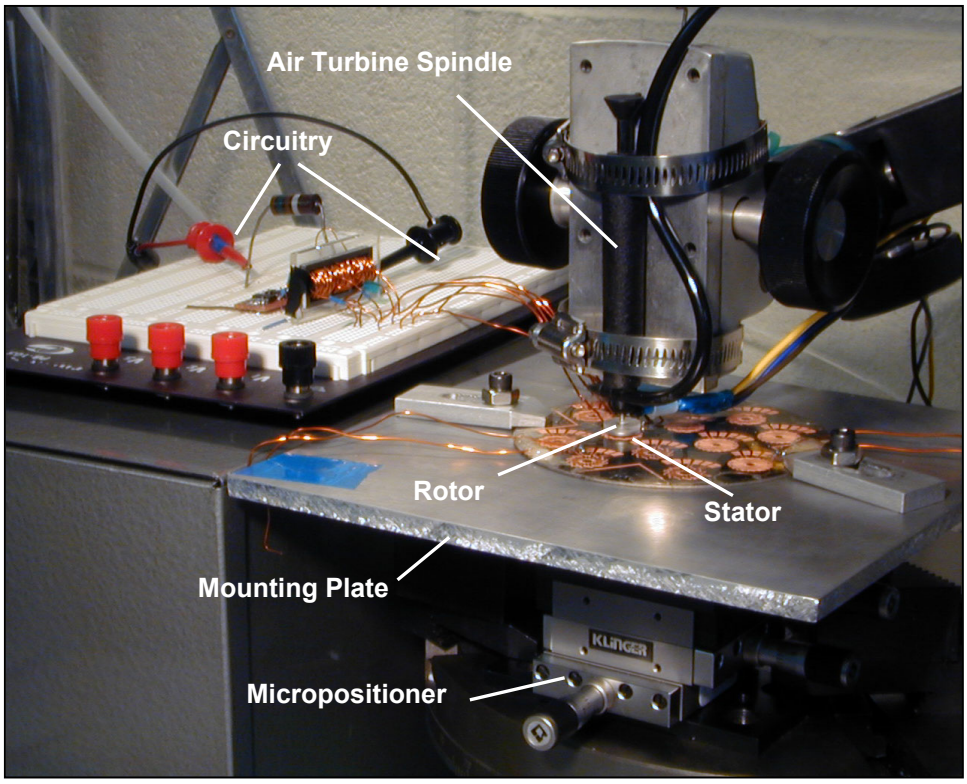

Figure 5.11. Photograph of spinning rotor test stand.

The alignment procedure was as follows. First, the angle between the rotor and stator was set by eye by adjusting the incident angle spindle. Then, a zero air gap was determined by bringing the stator up into contact with the rotor using the z-axis micropositioner. Due to small angular misalignments and/or irregularities in the surface of the stator or rotor, the absolute air gap is estimated to be within ±25 μm of the true value. The stator was then retracted to a 250 μm gap, and the rotor was spun at a moderate speed. Alignment in the x- and y-directions was achieved by monitoring the open-circuit output voltage waveforms during initial generation tests. The position of the stator was adjusted such that a symmetric and maximal output wave was indicated. Once this alignment procedure was completed, only adjustments to the air gap were made using the z-axis micropositioner control.

The air-driven spindle displayed a highly non-linear relationship between pressure and shaft speed, including hysteresis for increasing and decreasing pressure, as shown in Figure 5.12. Also, the speed-pressure dependence was significantly influenced by the dynamic mechanical loads imparted on the bearings during operation. For example, a rotor with high eccentricity would result in higher dynamic loads, more frictional bearing losses, and slower speeds as compared to rotor with similar mass, but lower eccentricity. Typical operating fluidic requirements for the spindle were 1 ft^3/min (4.72 x 10^{-4} m^3/s) at 45 psi (310 kPa) corresponding to 146 W of fluidic power.

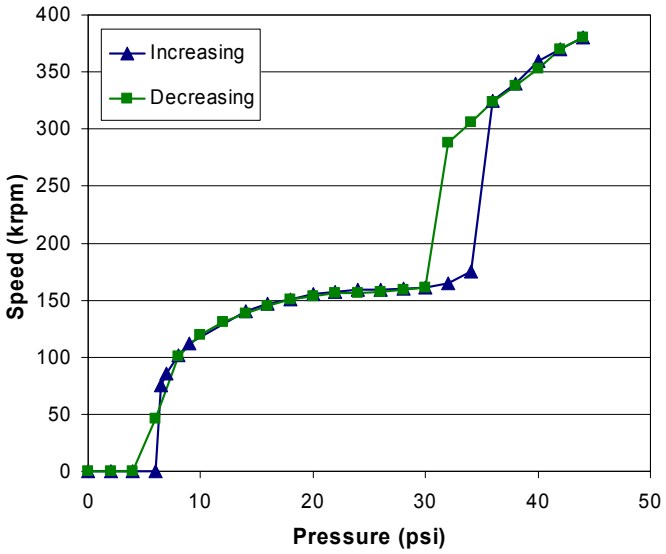

Figure 5.12. Example air-turbine spindle rotational speed vs. pressure.

5.4 PM Machine Fabrication

As has been stated previously, the PM generators were intended as first-generation, proof-of-concept devices. Thus, many of the integration challenges, particularly the requirement for a silicon-based, wafer-bonded fabrication process, were relaxed. Thus, stators were built using electroplated windings (the most critical aspect) on magnetic substrates. The rotors were conventionally machined and hand assembled for attachment to the spinning rotor test stand for rapid characterization. This process, like many of the previously researched micromotors/microgenerators [33-46], is a hybrid combination of microfabrication and assembly.

5.4.1 Stator Fabrication

First, 100-mm and 75-mm diameter substrates were cut from 1-mm thick sheets of $Ni_{80}Fe_{15}Mo_5$ (Moly Permalloy), purchased from Tech Metals & Materials (Holbrook,

NY). The substrates were then wet polished with increasingly finer grit SiC sandpapers up to 2400 grit, to provide a smooth, flat surface for patterning of the surface windings.

The complete winding fabrication process flow is shown in Figure 5.13, and the masks are shown in Appendix C. First, to isolate the coils from the substrate, a dielectric layer was deposited (Figure 5.13a). Initial attempts were made using a spin-on-glass (SOG) process. A 1-μm PECVD SiO_2 adhesion layer was deposited, followed by ~2 μm of Accuglass T-12 SOG (Honeywell Electronic Materials, Sunnyvale, CA), and finally, another 1-μm capping layer of PECVD SiO_2 was deposited. It was later found that this layer suffered from cracking and/or pin-hole defects that resulted in shorts from the coils to the substrate. Therefore, this process was supplemented or replaced by the deposition of ~5 μm of PI-2611 polyimide (HD Micosystems, Cupertino, CA).

The windings were constructed using a two-layer electroplating process that was identical for the 1-, 2-, and 4-turn per pole designs. First, a Ti/Cu seed layer was sputter deposited, and Futurrex NR9-8000P (Franklin, NJ) was used to pattern a mold for Layer 1 (Figure 5.13b). Cu was then electroplated using the bath listed in Appendix A (Figure 5.13c). Next, the resist was stripped using Futurrex RR4 (Franklin, NJ) and the seed layers removed using "blue etch" (NH_4OH saturated with $CuSO_4$) followed by 1:20 $HF:H_2O$ (Figure 5.13d).

The Via layer was then patterned using SU-8 2025 (Microchem, Newton, MA), encapsulating Layer 1 and opening vias for Layer 2 (Figure 5.13e). Then, a new Ti/Cu seed layer was sputter deposited, and Layer 2 was patterned using Futurrex NR9-8000P (Figure 5.13f). Cu was again plated to form Layer 2, with vias connecting to Layer 1

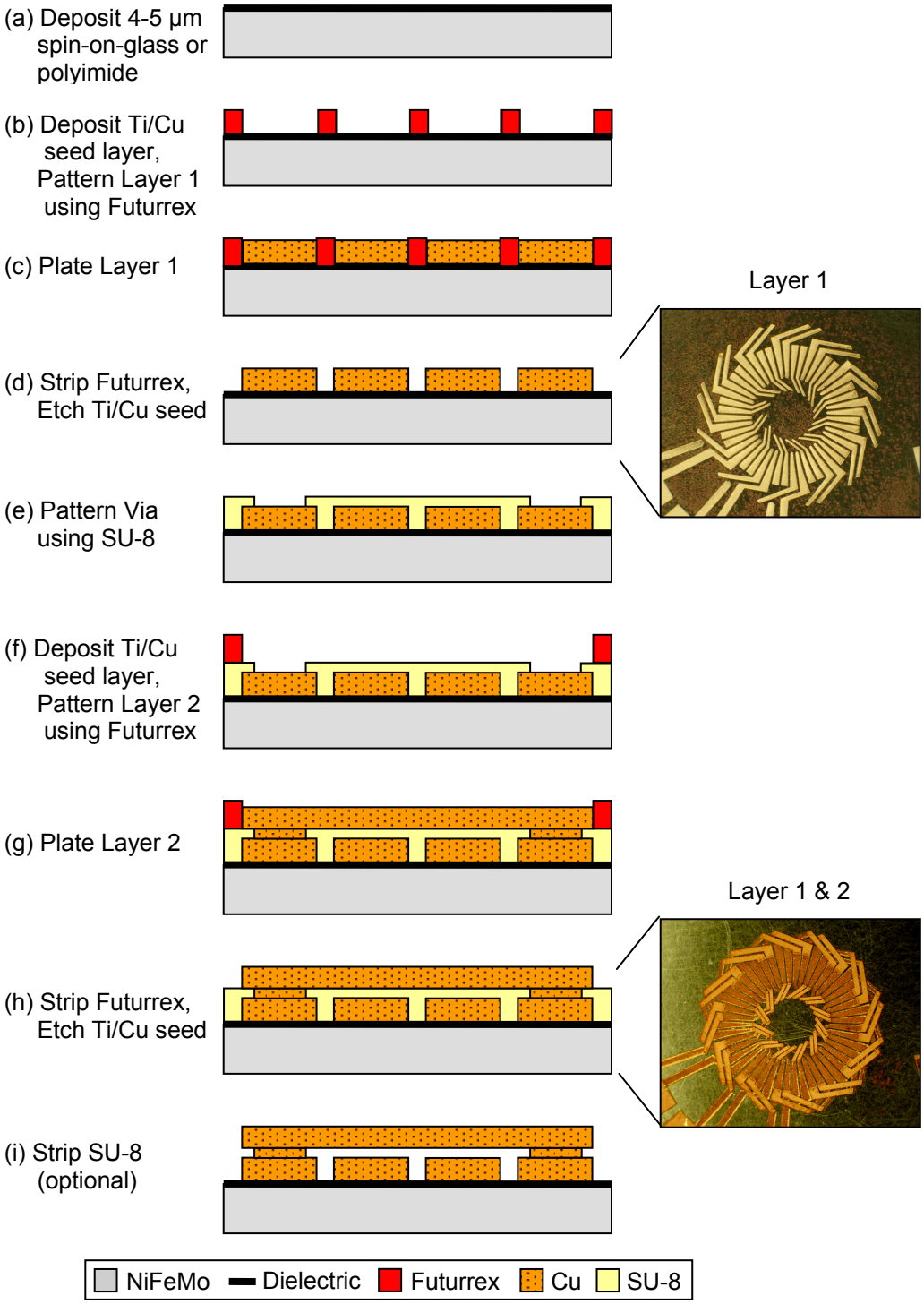

Figure 5.13. Fabrication process for PM machine stators, with example images of 2-turn per pole device.

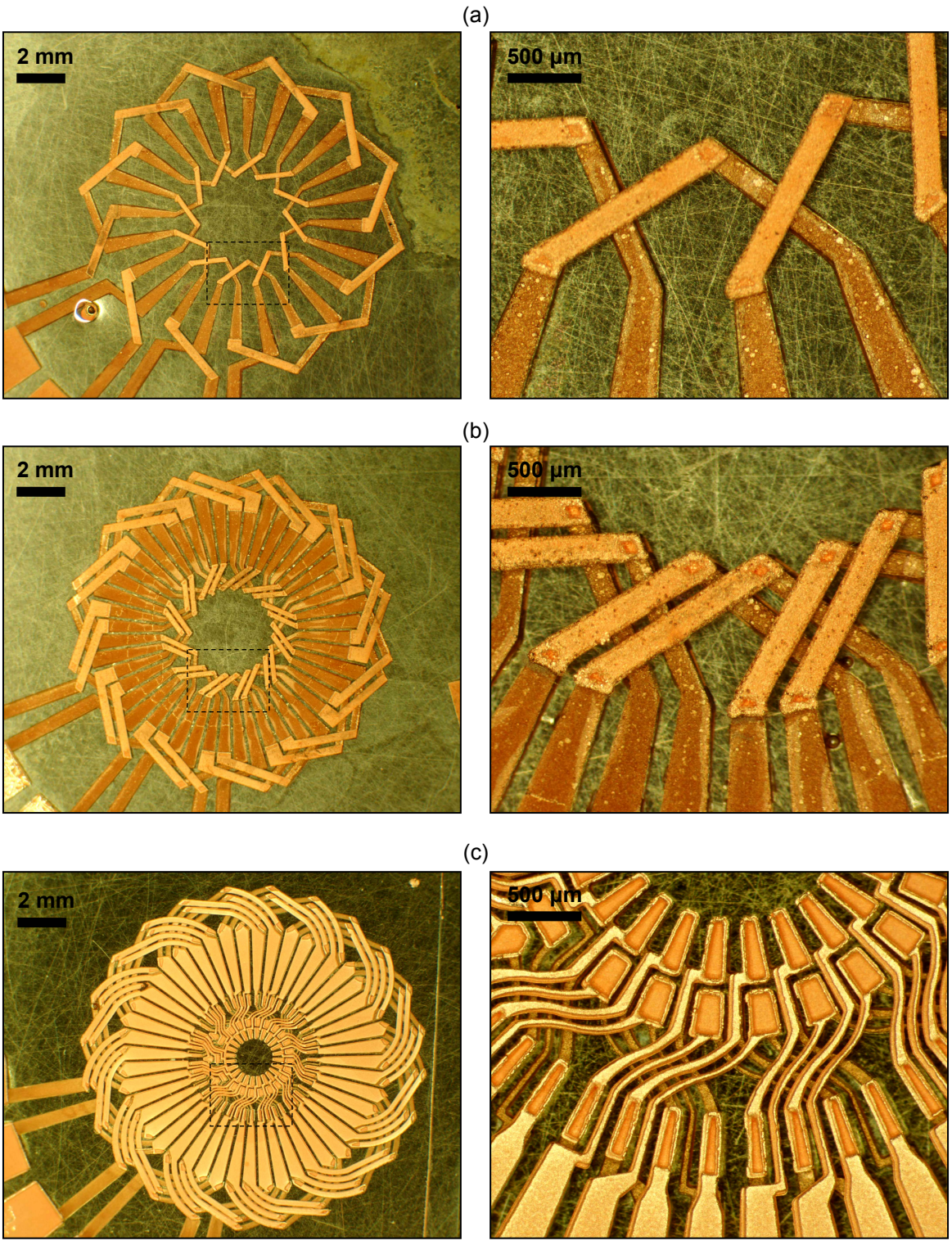

Figure 5.14. Images of fabricated (a) 1-turn, (b) 2-turn, and (c) 4-turn per pole PM machine stator windings showing wide view and detail of inner end turns.

(Figure 5.13g). Finally, the Futurrex resist was stripped and the seed layers etched as before (Figure 5.13h). The SU-8 was kept to provide additional mechanical support, but if needed (e.g. for high temperature compatibility), it could have been removed using RIE, resulting in free-standing coils (Figure 5.13i).

Figure 5.14 shows examples of the three types of windings after fabrication. Note that with an increasing number of turns, the winding patterns, particularly the inner end turns, become quite complex, and hence more difficult to fabricate. The thicknesses of the final windings were measured optically by ablating some of the SU8 using an excimer laser sysetm. Only the thickness of Layer 1, t_1, and the total thickness, t, were measured, as shown in Figure 5.15.

Device	t_1	t
1-turn	~125 μm	~245 μm
2-turn	~100 μm	~190 μm
4-turn	~80 μm	~170 μm

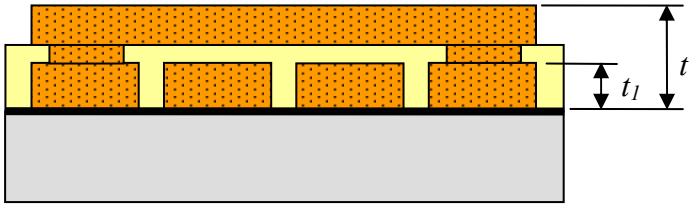

Figure 5.15. Measured winding thicknesses for various PM machines.

5.4.2 Rotor Fabrication

Rotor Magnetization

For use in the rotor, annular pressure-formed (sintered) Sm_2Co_{17} magnets were purchased from Eneflux Armtek Magnetics (Bethpage, NY), having 9.525 mm (3/8 in.)

OD, 3.175 mm (1/8 in.) ID, and 500 μm thickness. While having a slightly smaller ID than the stator, these magnets were selected because they were readily available in small quantities, without the need for custom (and costly) manufacturing. The units were delivered in a uniformly magnetized state along the central axis ("in thickness").

The required alternating poles of the SmCo were formed using a selective pulse magnetization method, as shown in Figure 5.16. A conventional pulse magnetizer (Model 340B, Oersted Technology, Troutdale, OR) was used, consisting of a high-voltage pulse discharge circuit connected to a ~160-mm long, ~120-mm diameter, solenoid coil magnetizing fixture. In operation, a bank of charged capacitors were rapidly discharged through the coil, creating a spatially uniform, high-amplitude, magnetic pulse within the coil. The magnitude and time of the pulsed field were controlled by the initial voltage and capacitance of the capacitor bank.

The rotor magnet was first uniformly magnetized to saturation using a high intensity pulse (Figure 5.16a). Next, selected regions were reversed using a magnetizing head with 4 poles (Figure 5.16b). The head, machined out of Hiperco 50 (Ed Fagan, Inc., Franklin Lakes, NJ), acted to collect and concentrate the magnetic fields only across the areas between the pole pieces, while shielding the other areas from the high-intensity reversal fields. Because of the field concentration, the reversal pulse was performed at a lower intensity.

In practice, this method required careful selection of the magnitude of the field reversal pulse. A very small pulse would not overcome the coercivity of the already magnetized structure, resulting in little or no reversal, while a very large pulse would reverse all areas of the magnet, presumably due to field fringing in the gap between the

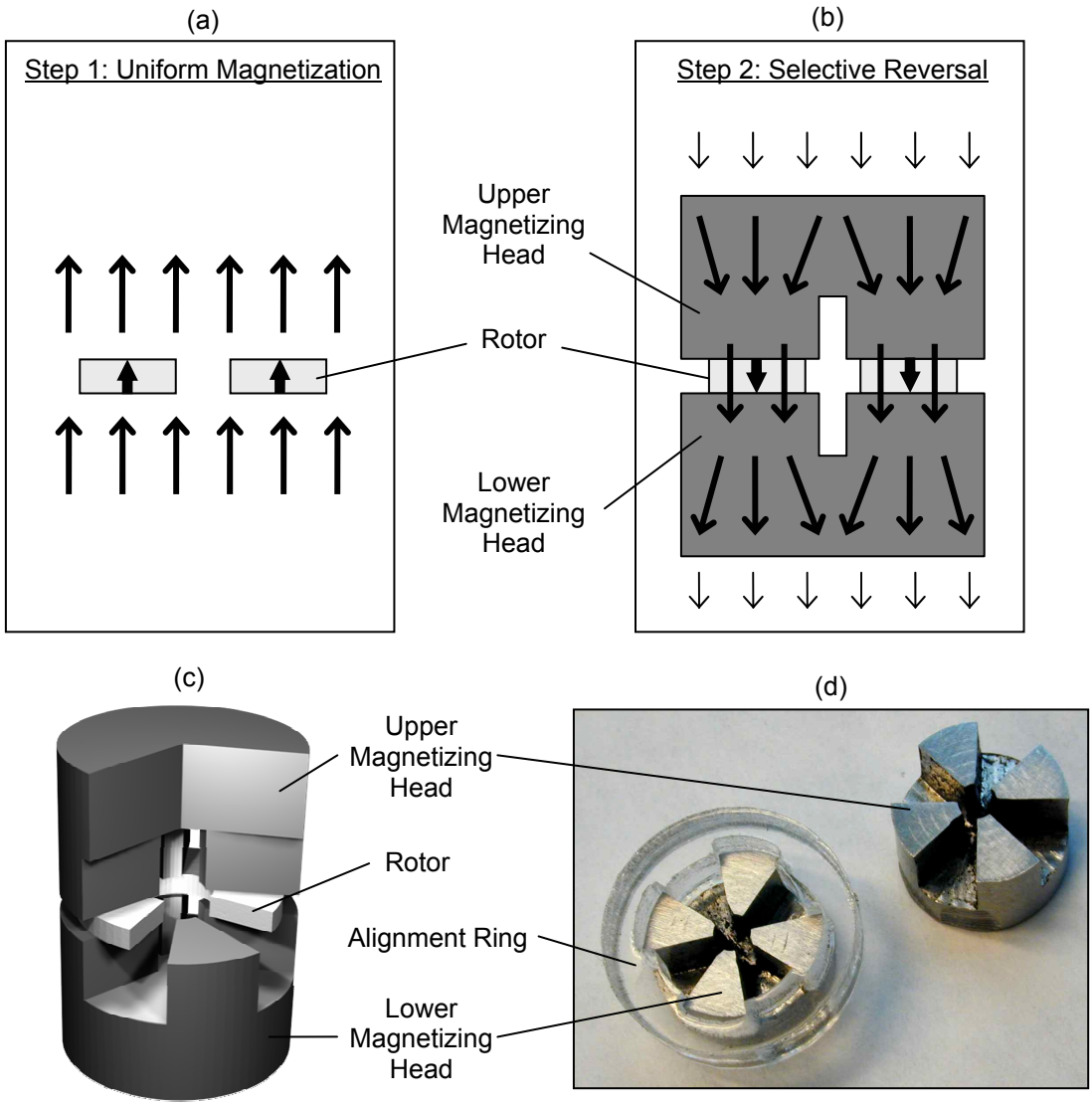

Figure 5.16. Method for magnetic patterning of multi-pole PM rotor: (a) initial uniform magnetization; (b) selective pole reversal using magnetizing head; (c) cutaway view of magnetizing head; (d) photograph of magnetizing heads.

two magnetizing heads. For the 500-μm thick SmCo magnetic, the uniform magnetization was performed using settings of 800 V and 79 mF. After uniform magnetization, an open-circuit *B*-field of +0.06 T was measured 250 μm above the magnet surface using a Hall-effect Gauss probe (F. W. Bell Model 9550, Sypris Test & Measurement, Orlando, FL). The reversal pulse was performed at 260 V and 39 mF, and resulted in equal but opposite poles of ±0.04 T, as measured by the Hall probe. Figure 5.17 shows the resulting magnetic pole pattern.

Figure 5.17. Magnetic pole pattern of 8-pole rotor, viewed using magnetic viewing paper.

As indicated by the measurements, the *B*-field of the magnet after poling (±0.04 T) is significantly lower than the uniform case (+0.06 T). This could be a real effect or the result of an inexact measurement. The Hall probe has a ~2 mm^2 measurement area, only slightly smaller than the pole itself, resulting in some spatial averaging. Also, the probe measures only the z-component of the fields 250 μm above the rotor surface due to the actual position and orientation of the Hall sensor within the probe casing. Thus, the

Hall probe may not be capturing the flux that leaks laterally between adjacent poles. Regardless of the results, the poling procedure was considered suboptimal because the purchased magnets were purchased in a premagnetized state. It would be preferred to start with virgin, un-magnetized rotors. Selective poling could then be achieved by magnetizing half of the poles in one direction, rotating the magnet and then magnetizing the other poles in the opposite direction, as described in [79]. Using this method, the fields would not need to overcome any existing magnetization, and may result in a significant *B*-field improvement.

Assembly

After magnetizing the SmCo PM, it and the back iron were assembled onto the shaft using a mounting adaptor. The back irons were fabricated by conventional milling of Hiperco 50, purchased from Ed Fagan, Inc. (Franklin Lakes, NJ), to the same dimensions of the PM: 9.525 mm (3/8 in.) OD, 3.175 mm (1/8 in.) ID, and 500 μm thick. The adaptor was conventionally machined from Poly(methyl methacrylate) (PMMA) to be 11.5-mm OD and 3-mm thick, with a 1 mm recess. The PM and back iron were glued using cyanoacrylate adhesive into the adaptor, which was aligned and glued onto a 1.6-mm diameter shaft. The design of the adaptor, machined with tight tolerances, permitted good concentricity and angular alignment between the rotor components and the shaft. The final assembly is shown in Figure 5.18.

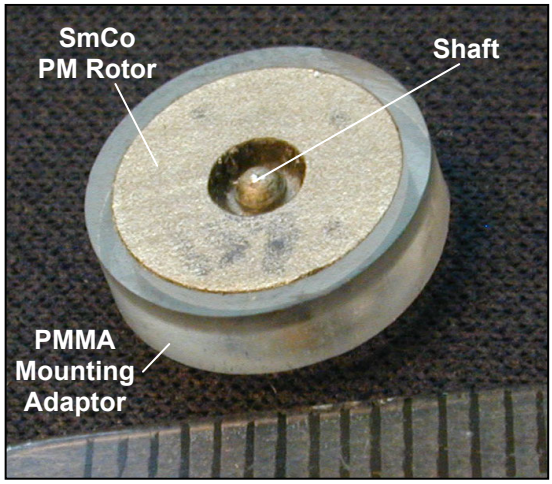

Figure 5.18. Perspective botrom view of 500-μm thick PM rotor and 500-μm thick FeCoV back iron assembled in a mounting adaptor on a 1.6-mm shaft.

5.5 PM Machine Characterization

The three different PM machine designs were characterized in three stages: (1) stator electrical characterization, (2) spinning rotor open-circuit voltage measurements, and (3) power generation using a three-phase voltage rectification circuit.

5.5.1 Stator Electrical Characterization

After fabrication, the phase resistances and inductances of the three machines were measured using a Keithley 3322 LCZ-meter (Cleveland, OH). Measurements were taken with the rotor as a function of air gap, but showed only ~2% variation for air gaps from 100-1000 μm. Thus, the resistances and inductances of the 1-, 2-, and 4- turn machines for a 100-μm air gap are tabulated in Table 5.1.

As can be seen, the resistance nearly doubled between the 1-turn and 2-turn machines as expected; the 2-turn machine winding has the same cross-section, but is twice as long. However, the resistance of the 4-turn machine is dramatically more than

double the 2-turn machine. This is due to the significantly smaller cross-sections of the inner end turns. The inductance is seen to increase with an increasing number of turns, but does not show the expected quadratic trend (the inductance should quadruple for each doubling of the number of windings). This may be due to a large leakage inductance for the wires connecting to the winding terminals. Regardless, the winding resistances are quite low (41, 98, and 690 mΩ), and the inductive reactances at the frequencies of interest (f_e < 10 kHz) are quite small. In fact, even at 10 kHz, the phase angles of the impedances are 15°, 12°, and 5°, respectively. Thus, all machine power generation characterization was performed using purely resistive loads.

Table 5.1. Measured phase resistances and inductances of 1-, 2-, and 4-turn per pole machines at 1, 10, and 100 kHz.

Machine	**R_φ (mΩ)**			**L_φ (μH)**		
	1 kHz	10 kHz	100 kHz	1 kHz	10 kHz	100 kHz
1-turn	40.9	41.2	50.0	0.18	0.177	0.165
2-turn	97.5	98.2	119	0.34	0.332	0.301
4-turn	690	693	764	0.98	0.965	0.860

5.5.2 Open-Circuit Voltages

Using the spinning rotor test stand, single-phase, open-circuit voltages were measured for the three different types of stators at speeds up to 150 krpm and air gaps from 100-1000 μm. Example waveforms and corresponding power spectral densities (PSD's) for the 1-, 2-, and 4-turn machines at 100 krpm (f_e = 6.67 kHz) and 100 μm air gap are shown in Figure 5.19. The waveforms exhibit good symmetry and low harmonic content, with over 1 V_{peak} for the 4-turn device.

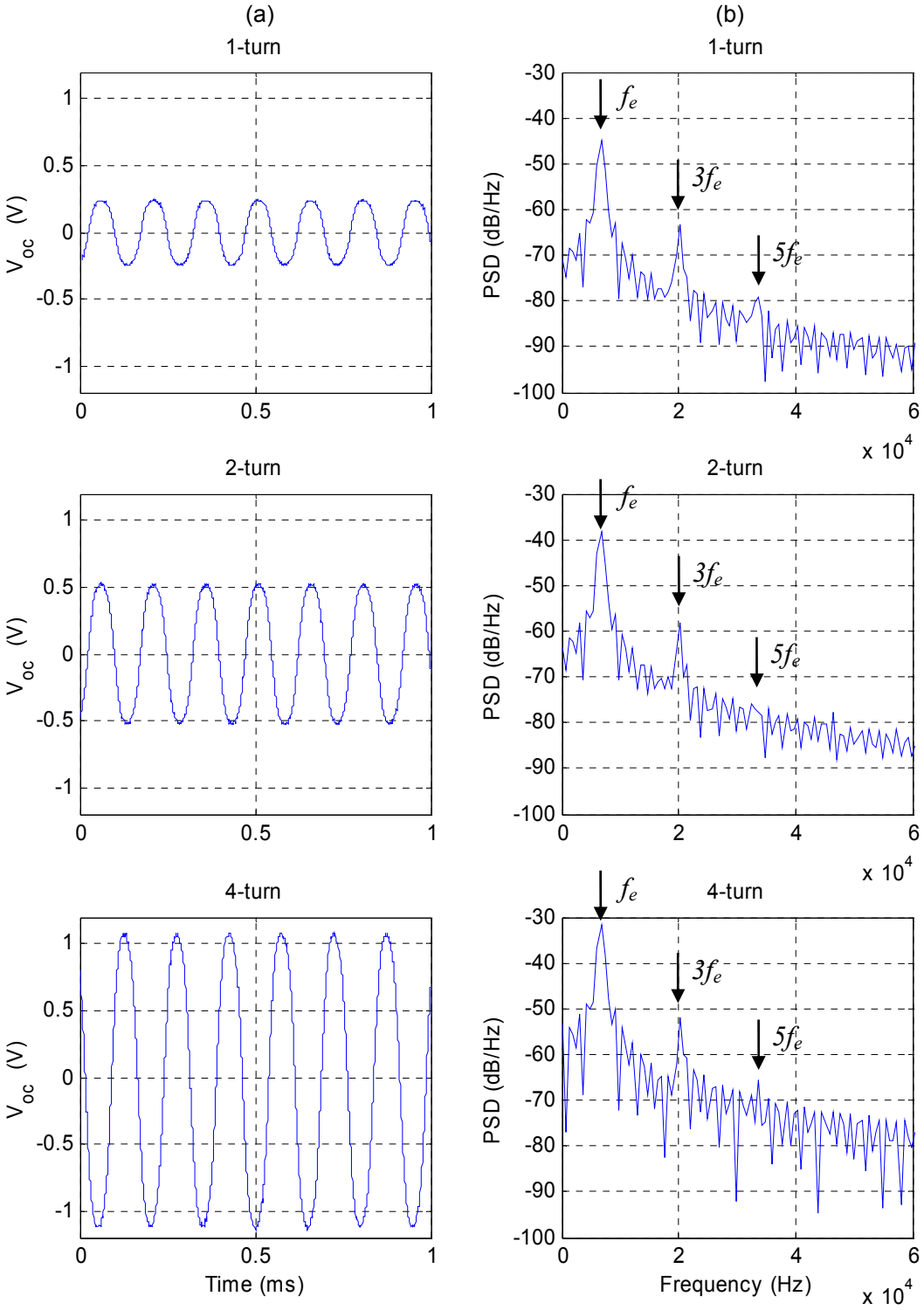

Figure 5.19. Single-phase open-circuit voltage (a) time waveforms and (b) power spectral densities for 1-, 2-, and 4-turn per pole PM machines at 100 krpm (f_e = 6.67 kHz) and 100 μm air gap.

Figure 5.20 shows the open-circuit voltage variation as a function of rotational speed for a fixed air gap of 100 μm. The open-circuit voltages exhibit a linear dependence on both speed and number of turns, as predicted by Equation 5.2. There is some scatter for the dependence with the number of turns because, while the machines were all tested at a 100 μm air gap, there are slight variations in the magnetic gap due to difference coil thicknesses (see Figure 5.15). Figure 5.21 shows the open-circuit voltage as a function of the air gap for a fixed speed of 100 krpm. The data indicates an exponential decay with increasing air gap, due to the decrease in the magnetic flux density as the magnetic gap increases. For both figures, the error bars indicate the possible range due to uncertainty in the absolute air gap, and the theoretical curves were generated by models from MIT [78].

Based on the measured open-circuit voltage and measured winding resistance, the theoretical maximum output power can be calculated using Equation 5.6. Doing so, the theoretical three-phase maximum output powers are plotted as a function of gap and speed in Figures 5.22 and 5.23, respectively. Note, that the 2-turn machine indicates the best performance, with a predicted maximum power over 3 W at 150 krpm and 100 μm air gap. While the 4-turn machine exhibited higher open-circuit voltages, the large coil resistance, a result of the small end turns, limits its maximum output power.

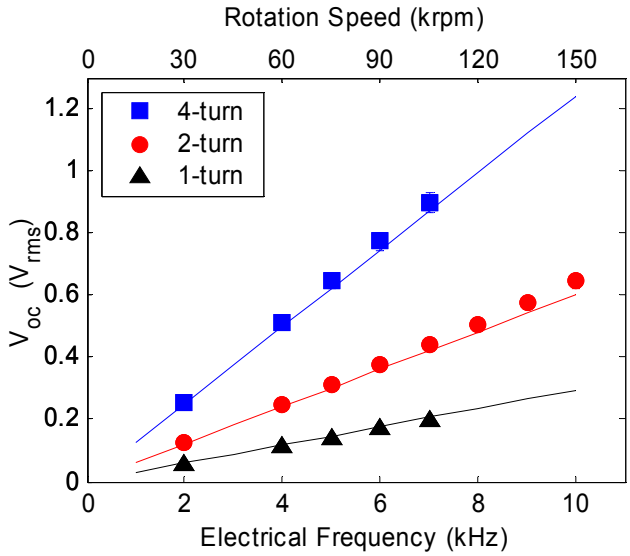

Figure 5.20. PM machine single-phase RMS open-circuit voltages as a function of speed, for a fixed air gap of 100 μm. Measurements are indicated with points, and theory, with solid curves.

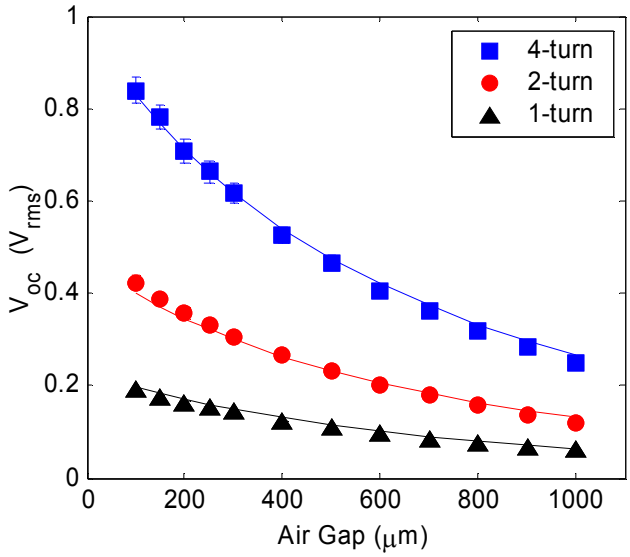

Figure 5.21. PM machine single-phase RMS open-circuit voltages as a function of air gap, for a fixed speed of 100 krpm (f_e = 6.67 kHz). Measurements are indicated with points, and theory, with solid curves.

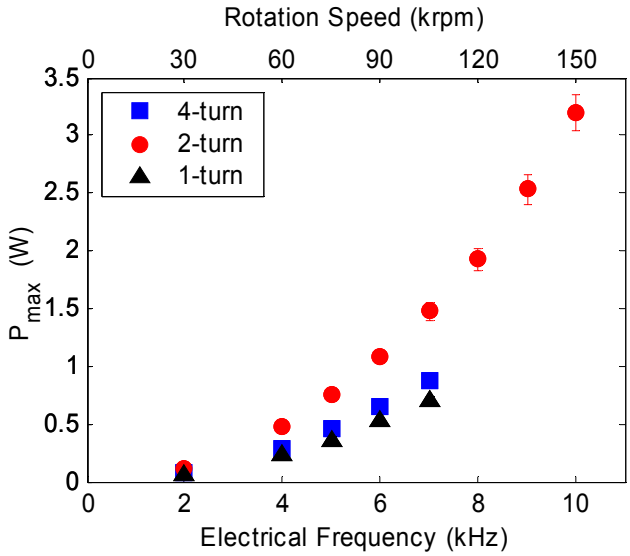

Figure 5.22. PM machine theoretical maximum three-phase output power as a function of speed, for a fixed air gap of 100 μm.

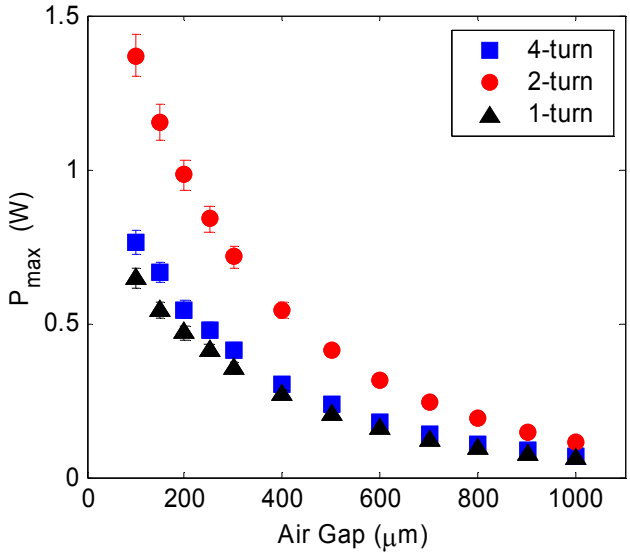

Figure 5.23. PM machine theoretical maximum three-phase output power as a function of air gap, for a fixed speed of 100 krpm (f_e = 6.67 kHz).

5.5.3 DC Power Generation

After the open-circuit voltages were measured, various tests were performed to demonstrate power generation. First, various load resistances were connected to a single phase of the machine in order to confirm the curves shown in Figure 5.23. These tests demonstrated AC power generation and confirmed that the 2-turn per pole machine yielded the highest output power. However, AC power is not desirable in a portable micropower system because almost all modern portable electronic devices require a DC source. Thus, a power conversion circuit was implemented to enable DC power generation as described below.

Power Electronics

To enable DC power generation, a simple three-phase passive voltage rectification circuit was considered. The machine output voltages were relatively small compared to a typical diode drop, so a three-phase, step-up transformer was designed and built (1:6 turn-ratio). The transformer and a three-phase, Schottky diode bridge were used to rectify the output voltage for DC power generation across a load resistor, as depicted in Figures 5.24 and 5.25. The transformer was built from three ferrite E-cores (Part#: PC40EI16-Z, MH&W International, Mahwah, NJ) and hand wound using magnet wire, with relevant properties summarized in Table 5.2. The diode bridge was assembled using 20 V, 3 A, Schottky diodes (Part# B320ADICT-ND, Digikey, Thief River Falls, MN) to minimize the diode voltage drops.

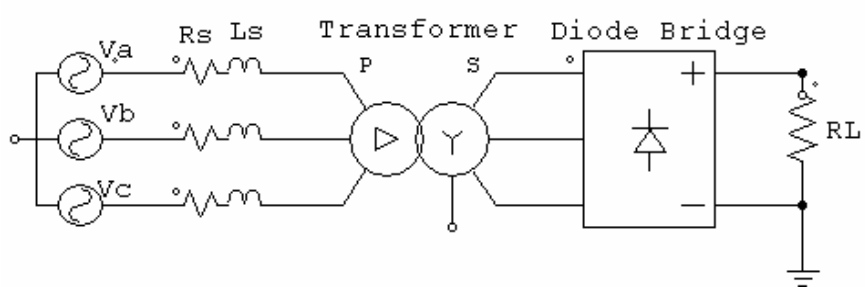

Figure 5.24. Three-phase rectification circuit for DC power generation tests.

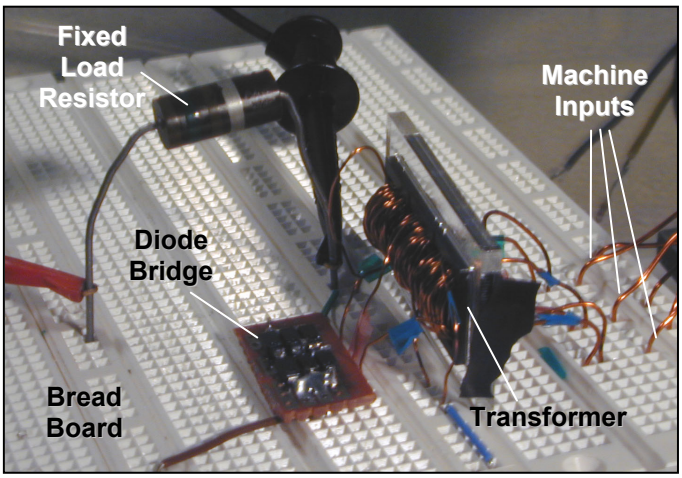

Figure 5.25. Photograph of PM machine passive power electronics circuit.

Table 5.2. Three-phase transformer properties.

Property	Primary	Secondary
Num. turns	10	60
Wire gage	22	25
R_x	18 mΩ	225 mΩ
R @ 6.67 kHz	18.3 mΩ	250 mΩ
Magnetizing Inductance, X_m	A: 56 µH B: 67 µH C: 114 µH	A: 2.0 mH B: 2.4 mH C: 4.1 mH
Leakage Inductance, X_l	A: ~0.01 µH B: ~0.01 µH C: ~0.01 µH	A: 16 µH B: 8.8 µH C: 17 µH

In addition to the turn-ratio of the transformer, the Δ–Y connections to the transformer and the Y–Δ connections to the diode bridge, result in net gain of 18 ($\sqrt{3} \times 6 \times \sqrt{3}$) between the machine phase voltage and the voltage ultimately applied across the diodes. Thus, the load resistance, reflected to each machine phase, is $(18)^2$ = 324 times smaller. This permitted the use of Ω-scale load resistors to match the mΩ-scale machine source impedances. Also note that the reflected secondary transformer winding impedances are $(\sqrt{3} \times 6)^2$ = 108 times smaller on the machine side. Thus, 50 Ω and 500 Ω wire-wound 12.5W rheostats (Part# RES50R-ND, RES500-ND, Digikey, Thief River Falls, MN) were used for the loads, expediting the characterization. For both rheostats, the imaginary reactances were <5 % of the real resistance for the frequencies of interest (<10 kHz), so they were treated as purely resistive loads.

DC Power Generation

Using the circuit described above, the machines were characterized using resistive loads under a variety of operating conditions. Only the results from the 2-turn per pole machine are presented here, because it demonstrated the highest output power. The load voltage waveforms were measured using an oscilloscope, and power was computed by dividing the square of the mean voltage by the resistance of the load, as measured via a 4-point probe using a Keithley 3322 LCZ-meter (Cleveland, OH). Figure 5.26 shows the measured waveforms for several different load resistances at 100 krpm. The open-circuit waveform is somewhat irregular, attributed to the unbalanced magnetizing inductances of the transformer (see Table 5.2). However, under load, the waveform exhibits six fairly uniform peaks within the span of one electrical cycle, $T = 1 / f_e$, corresponding to the rectified peaks of each of the three phases.

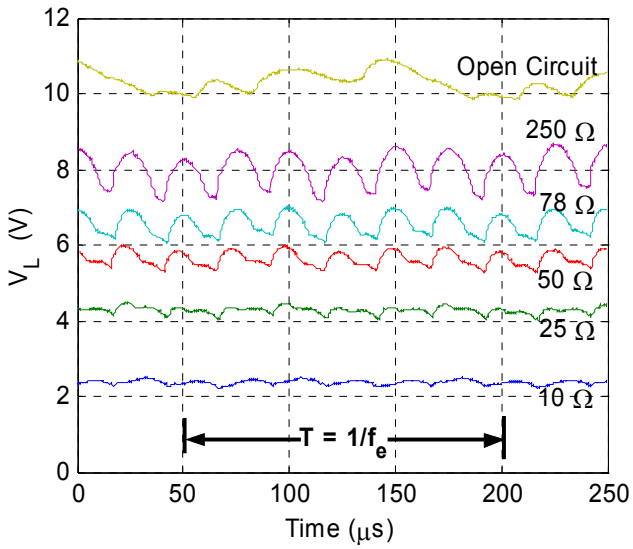

Figure 5.26. 2-turn PM machine load voltage waveforms for various load resistances at 100 krpm.

Figure 5.27 shows the DC output power for a variety of loads (~10-250 Ω) at speeds of 80, 100, and 120 krpm. The measurements are indicated with 95% confidence intervals. The theoretical curves represent the output power as predicted from the PSpice model [78], using the measured open circuit voltages as the input. The machine shows the expected power transfer characteristics, with output power maximized under a matched load condition of $R_l \approx 25\ \Omega$. At the three different rotational speeds, the machine exhibited maximal powers of 0.46, 0.76, and 1.1 W, respectively. For an active machine volume of 110 mm^3 (9.5 mm OD, 5.5 mm ID, 2.3 mm thick), 1.1 W corresponds to a power density of 10 MW/m^3.

Figure 5.28 plots the DC output power as a function of the speed for a fixed load of 30 Ω, and confirms the expected quadratic dependence on speed up to 120 krpm. Comparing this curve to the theoretical maximum power curve shown in Figure 5.22, the machine falls short of the predicted maximum output power of 1.9 W. First, recall that

those predictions were computed by assuming purely resistive source and load resistances, and ignored any armature reaction core losses and losses in the power conversion circuit.

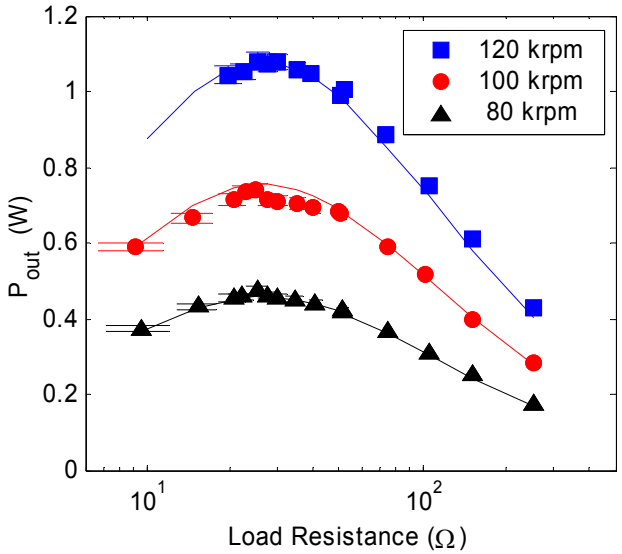

Figure 5.27. 2-turn PM machine measured DC output power versus load resistance at 80, 100, and 120 krpm for 100 μm air gap. Measurements are indicated with points, and theory, with solid curves.

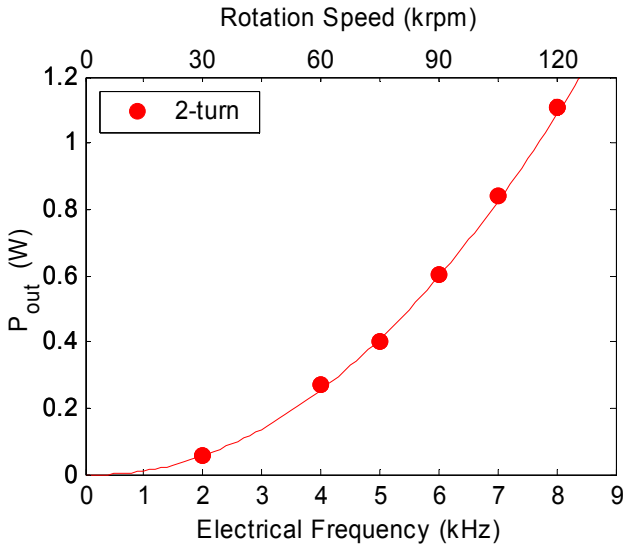

Figure 5.28. 2-turn PM machine measured DC output power as a function of speed for 100 μm air gap. Measurements are indicated with points, and theory, with solid curve.

Efficiency

In addition to the total output power, the machine efficiency is an important consideration in the machine design. Direct experimental measurement of the total generator electrical efficiency, η_g, was not possible because the input mechanical power, P_m, was not measurable. While the shaft speed, ω_m, could be accurately measured using the shaft speed sensor, measurement of the shaft torque, τ_m, required a dynamometer that could resolve ~1 μN·m torques, support rotational speeds in excess of 100 krpm, and be small enough to integrate with the spinning rotor test stand. Unfortunately, a suitable transducer or measurement system was not found.

Instead the total input mechanical power was estimated by summing the core loss and electrical power, $P_m = P_{core1} + P_e$. The core loss, P_{core1}, was extracted from the analytical MIT machine models [78], and the electrical input power, P_e, was extracted from the PSpice models [78], based on the experimentally measured load voltages.

Figure 5.29 shows the distribution of power within the machine as a function of load resistance, for the 2-turn machine at 120 krpm and an air gap of 100 μm. Recall from Section 5.2 that the core loss is nearly independent of the stator current, and thus does not change with load resistance. The total input power is seen to decrease with increasing load resistance, and asymptotes to the eddy current loss, as less power is delivered to the electrical circuit. The total converted electrical power is given by $P_e = P_m - P_{core} = P_{cond} + P_{circuit} + P_o$.

Figure 5.30 shows the electrical efficiency, $\eta_e = P_o / P_e$, and total generator efficiency, $\eta_g = P_o / P_m$, for the 2-turn machine as functions of load resistance and speed. The total efficiency is seen to be substantially lower than the electrical efficiency,

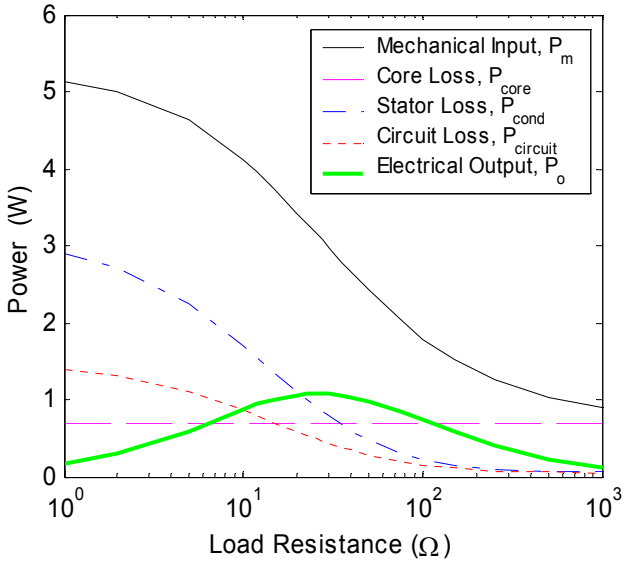

Figure 5.29. Distribution of 2-turn PM machine power as a function of load resistance at 120 krpm for an air gap of 100 μm.

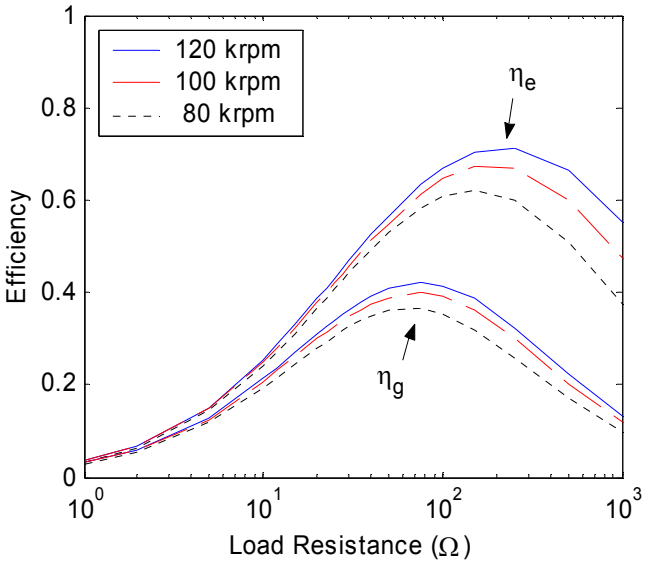

Figure 5.30. Electrical efficiency, $\eta_e = P_o / P_e$, and generator efficiency, $\eta_g = P_o / P_m$, for 2-turn PM machine for an air gap of 100 μm.

suggesting the need for stator laminations to minimize core loss. At the matched load (maximal output power) condition of $R_l \approx 25\ \Omega$, the machine at 120 krpm shows an electrical efficiency of 43% and generator efficiency 34%. Thus, it required 3.2 W of mechanical power, of which 2.6 W was converted by the machine to electrical power, to generate the 1.1 W maximal output power.

It is interesting to note the deviation of the electrical efficiency as compared to the ideal (no circuit losses) electrical efficiency curve shown in Figure 5.6. The ideal curve shows an efficiency of 50% for a matched load condition and asymptotes to 100% with increasing load resistance. The measured data falls short of these values due to the circuit losses. In fact, the electrical efficiency curves actually exhibit a maximum (71% for the 120 krpm curve), followed by a downturn with increasing load resistance. This effect is attributed to the non-linear elements in the voltage rectification circuit, such as the diodes, which exhibit a non-linear loss as a function of the stator current. The electrical efficiency is also shown to increase with increasing speed. In the ideal case, the electrical efficiency (ignoring reactive components) should be independent of the frequency. This effect is again attributed to non-linearities in the circuit, such as the nearly constant diode voltage drop and/or non-linear transformer core loss behavior as a function of voltage. In future implementations, these circuit losses can be reduced by replacing the passive voltage-rectification circuit with a more efficient, transistor-based power converter.

5.6 PM Machine Summary

To summarize, three-phase synchronous PM generators were designed and fabricated using a hybrid combination of microfabrication and precision machining/assembly. The machines were characterized using an air-driven spindle in

generating mode. At 120 krpm, the machines demonstrated 2.6 W of mechanical-to-electrical power conversion and delivered 1.1 W of DC power to a resistive load. For an active machine volume of 110 mm^3 (9.5 mm OD, 5.5 mm ID, 2.3 mm thick), this corresponds to a power density of 10 MW/m^3. Extrapolating this power to the design speed of 1 Mrpm, indicates the potential for ~76 W (690 MW/m^3).

These results convincingly prove that watt-level power production is achievable using miniaturized magnetic machines and demonstrate the viability of scaled PM machines for portable power applications. The numbers represent orders of magnitude performance improvement over the previously reported electric induction [22-28] and magnetic induction [29-35] machines. While the fabrication methods are not immediately integrable within the proposed silicon microengine concept, the machine dimensions and layout certainly are. However, the ability to measure and characterize actual mechanical-to-electrical power generation provides much more convincing results as compared to the extrapolations used to estimate the potential power from the induction machine tethered torque measurements.

CHAPTER 6

CONCLUSIONS

6.1 Comparisons of Micromachines for Microengines

This section aims to summarize and compare the various micromachines developed for use with MIT microengine in terms of measured/projected performance and integrability. The three different machine types are discussed: electric induction machine, magnetic induction machine, and permanent magnet machine.

The design of the microengine has evolved over the years of research, resulting in the gradual growth of the projected size from a rotor size of ~ 4mm OD up to ~12 mm OD. Thus, the different machines, investigated at different times during the development, are all of various sizes, so normalization is required to permit a "fair" comparison. For this comparison, only the active volume of each machine is considered, which includes the electrically/magnetically active stator core, rotor core, and air gap volume. Explicitly excluded are the conductor inner and outer end turns, external connections, surrounding mechanical structures, etc.

Each machine is considered to take an annular form as shown in Figure 6.1, with inner radius, a, outer radius, b, and total thickness, t, with active machine volume given as $V = \pi (b^2 - a^2) t$. Torque density and power density simply normalize the torque and power, respectively, by the active volume. The average shear stress normalizes the torque generated on the surface of the rotor by surface area and moment arm. Assume, in motoring mode, the torque is the result of a constant shear stress, σ, acting on the surface of the rotor. The total torque is, thus, obtained by integrating the shear stress x moment arm across the area of the rotor,

$$T = \int_a^b r\sigma 2\pi r dr = \tfrac{2}{3}\pi\sigma(b^3 - a^3). \tag{6.1}$$

Solving for the shear stress yields

$$\sigma = \frac{3T}{2\pi(b^3 - a^3)}, \tag{6.2}$$

which represents the average electromechanical surface force being generated on the rotor.

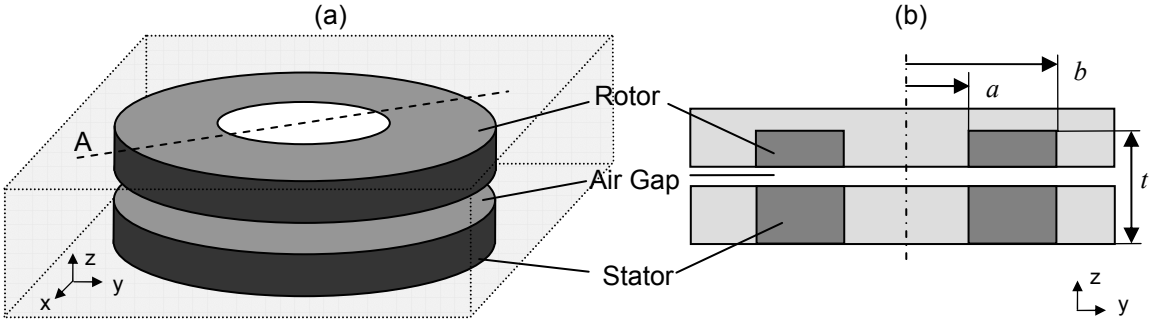

Figure 6.1. Simplified machine dimensions for performance comparisons, depicting an active annular volume of inner radius, *a*, outer radius, *b*, and thickness, *t*.

A comparison of the various machines and their respective performances is shown in Table 6.1. While the absolute motoring torques from the electric [25,26] and magnetic (Chapter 4) induction machines are comparable, when comparing torque density and surface shear stress, the electric version appears to yield better performance. However, the 0.1 mW of generated power from the electric induction machine [27,28] is a mere fraction of the 1.1 W demonstrated for the PM machine. When scaling both generators up to the design speed of 1 Mrpm, assuming a quadratic power increase with speed, the electric induction machine extrapolates to 1.7 W (0.15 MW/m^3), as compared to 76 W

(690 MW/m^3) for the PM machine. Thus, the PM machine is clearly the best candidate for maximum power density.

However, in addition to the electromechanical performance, a comparison of the various machine types must address the fabrication complexity and overall integrability within a silicon-based microengine. All potential machines must use a fabrication process compatible with multi-wafer-bonding. In addition, the machine must survive the 300°C operating temperatures expected within the microengine. One of the most difficult challenges is designing a rotor that can survive the mechanical demands of ~1 Mrpm spin speeds. Hence, there are still many lingering questions for all of these machines.

A brief comparison of the three machine types and respective pros and cons are shown in Figure 6.2. The electric induction machine is undeniably closest to full integration with the silicon microengine, having already demonstrated generation with a self-contained spinning rotor suspended on air bearings using multi-wafer silicon stack [27,28]. The magnetic induction machine has shown steps toward integration, demonstrating the viability of integrating electroplated magnetic components within fusion bonded silicon. Finally, the PM machine is currently furthest from integration; the first generation devices were constructed using various macromachined magnetic materials and without the use of silicon.

Table 6.1. Comparison of demonstrated performances of various machines developed for the MIT microengine.

Ref.	Type*	Mode†	a‡ (mm)	b‡ (mm)	t‡ (mm)	V (mm^3)	Max. Torque (μN·m)	Torque Density (N·m/m^3)	Avg. Shear Stress (N/m^2)	Max. Speed (krpm)	Max. Power (W)	Power Density (MW/m^3)
[22,23]	EI	TM	1.0	1.9	1.0	11	0.22	20	18	-	-	-
[24]	EI	M	1.0	1.9	1.0	11	0.3	26	24	15	$5x10^{-4}$	0.045
[25,26]	EI	M	1.0	1.9	1.0	11	3.5	303	280	55	0.02	1.8
[27,28]	EI	G	1.0	1.9	1.0	11	-	-	-	245	$1x10^{-4}$	0.009
[31-35]	MI	TM	1.0	2.0	2.0	19	0.3	16	20	-	-	-
Ch. 4	MI	TM	3.0	5.0	1.5	75	2.5	33	12	-	-	-
Ch. 5	PM	G	2.8	4.8	2.3	110	-	-	-	150	1.1	10

* EI = electric induction, MI = magnetic induction, PM = permanent magnet; † TM = tethered motor, M = motor, G = generator; ‡ a = core inner radius, b = core outer radius, t = thickness of rotor, air gap, stator

Table 6.2. Comparison of integrability with silicon microengines for various machine types.

Type	Pros	Cons	Integrability
Electric Induction Machine	- high temperature - mechanically robust rotor - no laminations needed	- large windage losses - parasitic losses - large auxiliary electronics - complex, micron-scale features	Good
Magnetic Induction Machine	- no PM materials - all electrodeposited materials	- poor efficiency - voluminous rotor - requires laminated stator - complex micromachining and electroplating	Seems feasible
Permanent Magnet Machine	- excellent performance - simpler stator fabrication	- voluminous, brittle rotor - requires laminated stator - high-temp. compatibility? - potential for demag. - integration of bulk materials? - batch magnetization?	Needs further investigation

6.2 Summary

This research began with the goal of developing second-generation, silicon-based magnetic induction machines as a candidate power generation technology for MIT's silicon microengine. Continuing the efforts of Cros and Koser [29-35], silicon-based magnetic induction machines were developed that demonstrated key fabrication technologies and a path for integration. However, the induction machine design continued to demonstrate minimal performance, falling short of the predicted performance due to numerous fabrication constraints. Thus, a fresh approach was taken, switching the investigation to PM machines rather than induction machines. As with the

first-generation prototypes for the induction machine, the primary goal was to demonstrate power generation while relaxing the requirements for a monolithic, silicon-based fabrication approach. The contributions of this research are, thus, logically organized into three areas:

- Development and analysis of microfabrication technologies to enable magnetic machine components to be integrated within a silicon microengine
- Development of second-generation, silicon-based magnetic induction machines that demonstrated silicon microengine ***integrability*** at the expense of electromechanic *performance*
- Development of novel PM generators that demonstrated superb electro-mechanic ***performance*** while postponing issues of microengine *integrability*

In the first phase of research (Chapter 2), various fabrication technologies were developed to enable thick electroplated materials to be integrated within etch and wafer-bonded silicon microstructures. The first was a method for encapsulating electroplated structures inside cavities within fusion-bonded silicon. A low-temperature bonding scheme permitted strong wafer bonds while permitting the embedded Cu and NiFe structures to retain their electrical and magnetic properties. Second, two methods were developed and characterized to enable vertical magnetic laminations within the thickness of a silicon wafer, critical for minimizing eddy current losses in high-frequency magnetic devices. Third, methods were developed for inlaying large areas of electroplated metals in the surface of silicon. While developed for specific components for magnetic machines, these processes can be applied to a wide variety of other microdevices. Extra

attention was focused on the optimization of magnetic laminations in the context of certain microfabrication constraints (Chapter 3).

In the second phase of research (Chapter 4), these fabrication methods were used to construct two-phase, eight-pole induction machines within silicon substrates. Silicon etching, wafer bonding, and electrodeposition was used to form embedded Cu windings in a laminated, slotted ferromagnetic NiFe or CoFeNi stator core. The induction machines were characterized in motoring mode using tethered rotors, and motoring torques of up to 2.5 μN·m were measured. These devices demonstrated the ability to integrate magnetic machine components within silicon, but mechanical-to-electrical power generation was never achieved.

In the third phase of research (Chapter 5), PM machines were investigated using a hybrid microfabrication/assembly approach. Three-phase, eight-pole stators were made using surface wound electroplated Cu coils on ferromagnetic NiFeMo substrates. The rotors used selectively magnetized SmCo as the PM and FeCoV as the back iron. The PM machines were tested in generating mode with free-spinning rotors, powered by an air-driven turbine. This enabled the demonstration of 2.6 W of mechanical-to-electrical power conversion and continuous DC power generation of up to 1.1 W at 120 krpm rotor speed. These devices prove that watt-level power production is achievable using miniaturized magnetic machines and demonstrate the viability of scaled PM machines for portable power applications.

6.3 Suggestions for Future Work

The PM generators are the first machines developed for the MIT microengine that demonstrated power commensurate with the overall design goals. Thus, regardless of the

design and fabrication challenges, PM machines may have emerged as the most viable approach for achieving the desired 10-100 W for a microengine system. However, there are still many problems to be addressed, most notably, developing a clear strategy for integration with the silicon microturbine.

Methods must be identified for fabricating and magnetizing large regions of PM material in a silicon framework to form the magnetic rotor. This may require a hybrid approach relying on embedding precision-machined, high-performance, bulk magnetic materials within microfabricated silicon structures. Most importantly, the rotor structure must be modeled to determine the mechanical stability and to direct design modifications to achieve the desired operating speeds and temperatures. The mechanical analysis should be coupled with a full electromagnetic optimization to determine the best materials and machine geometries for maximum power output and/or efficiency. Techniques for incorporating laminations in the stator should be identified for minimizing eddy current losses, particularly troublesome at higher operating speeds.

Before undertaking an integrated design approach, additional characterization could be performed with the existing machines and test stand. Higher rotational speeds and/or smaller air gaps could be used to demonstrate higher power densities. Also, elevated temperature testing should be performed to verify proper machine operation at the projected operating temperatures. Various rotor and/or stator materials could be investigated for performance comparisons and to improve the modeling capabilities. One major characterization challenge is finding a method for experimentally measuring the input mechanical power of the high speed rotating device. This would permit more

precise characterization and analysis of eddy current losses and overall machine efficiencies.

To conclude, the goals of this research were fairly focused and constrained by system level design boundaries. However, the scope and application of this research extend well beyond the MIT microengine. Magnetic micromachines and the fabrication processes developed herein can be applied to a wide variety of other electromechanical microdevices including motors/generators, valves, pumps, sensors, etc. The growing area of power MEMS is fertile ground for combining magnetic and electrodynamic transduction schemes with the superb mechanical properties of silicon, and hopefully this research will serve as a springboard for future investigations.

APPENDIX A

ELECTRODEPOSITION BATHS

This section lists the electrodeposition parameters used for depositing Cu, NiFe, and CoFeNi. All chemicals are listed per liter of the final bath solution.

Table A.1. Cu electrodeposition bath [80].

Parameter	Chemical Symbol	Value
Copper Sulfate	$CuSO_4 \cdot 5H_2O$	250 g/L
Sulfuric Acid	H_2SO_4	25 mL/L

Cu anode, pH = ~1, 20-25°C, 10-20 mA/cm^2

Table A.2. $Ni_{81}Fe_{19}$ electrodeposition bath [80].

Parameter	Chemical Symbol	Value
Nickel Sulfate	$NiSO_4 \cdot 6H_2O$	200 g/L
Ferrous Sulfate	$FeSO_4 \cdot 7H_2O$	8 g/L
Nickel Chloride	$NiCl_2 \cdot 6H_2O$	5 g/L
Boric Acid	H_3BO_3	25 g/L
Saccharin	$C_7H_5NO_3S$	3 g/L

Ni anode, pH = ~4, 20-25°C, 10 mA/cm^2

Table A.3. $Co_{52}Fe_{26}Ni_{22}$ electrodeposition bath [81].

Parameter	Chemical Symbol	Value
Nickel Sulfate	$NiSO_4 \cdot 6H_2O$	52.5 g/L
Ferrous Sulfate	$FeSO_4 \cdot 7H_2O$	4.17 g/L
Cobalt Sulfate	$CoSO_4 \cdot 7H_2O$	16 g/L
Boric Acid	H_3BO_3	25 g/L
Saccharin	$C_7H_5NO_3S$	0.5 g/L

Pt anode, pH = 2.8, 20-25°C, pulse plating: 7 ms on, 3 ms off, 10 mA/cm^2 avg.

APPENDIX B

INDUCTION MACHINES MASKS

This section includes the nine masks used in the fabrication of the induction machines. All masks are shown as clear-field, but the actual polarity (clear-field vs. dark-field) of the mask is noted in each caption. Also, the lower half of each mask was designed for machines with more complicated coil windings. However, these devices were not fabricated successfully and are not addressed within this document.

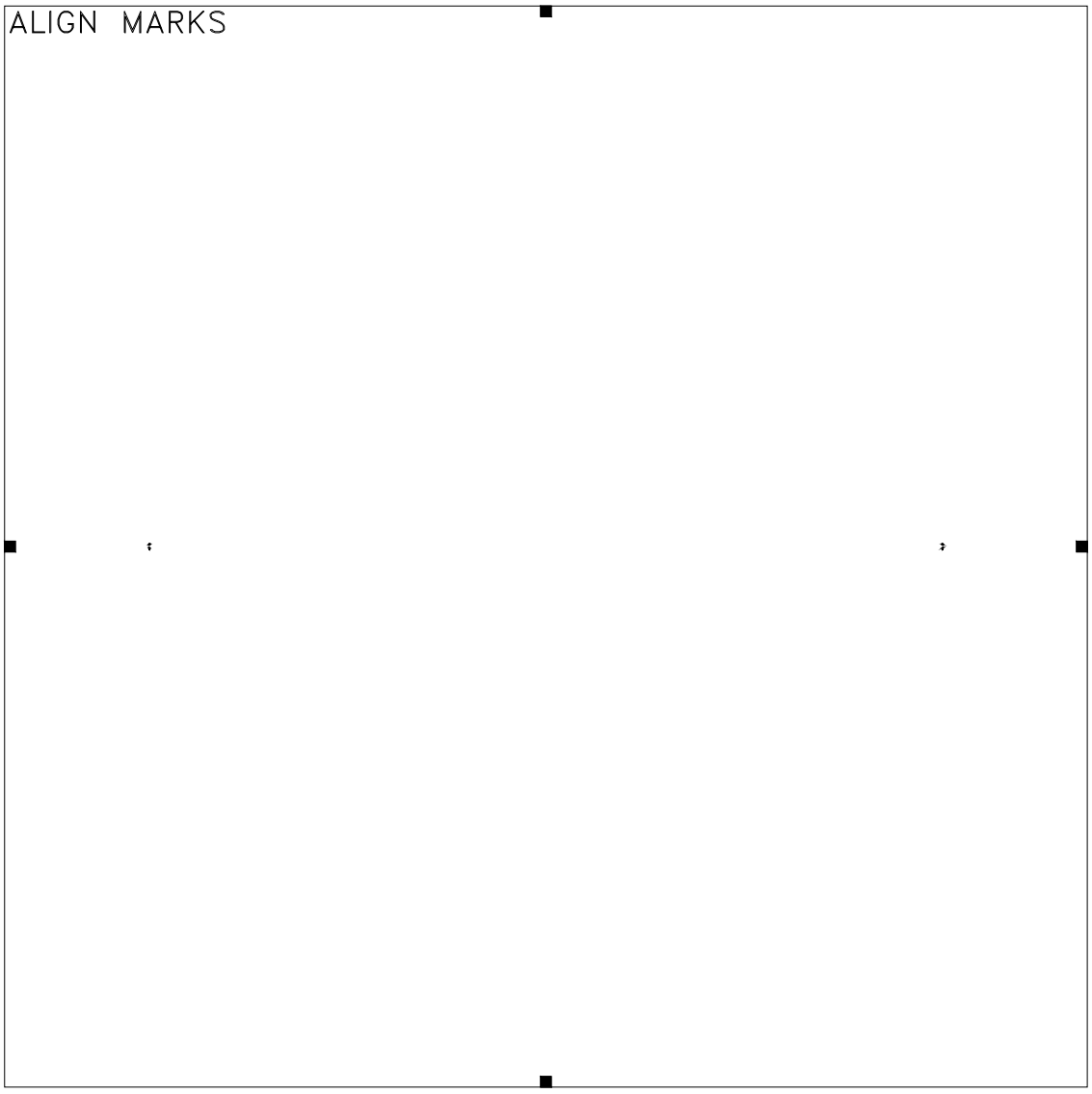

Figure B.1. Induction machine stator alignment marks mask (darkfield).

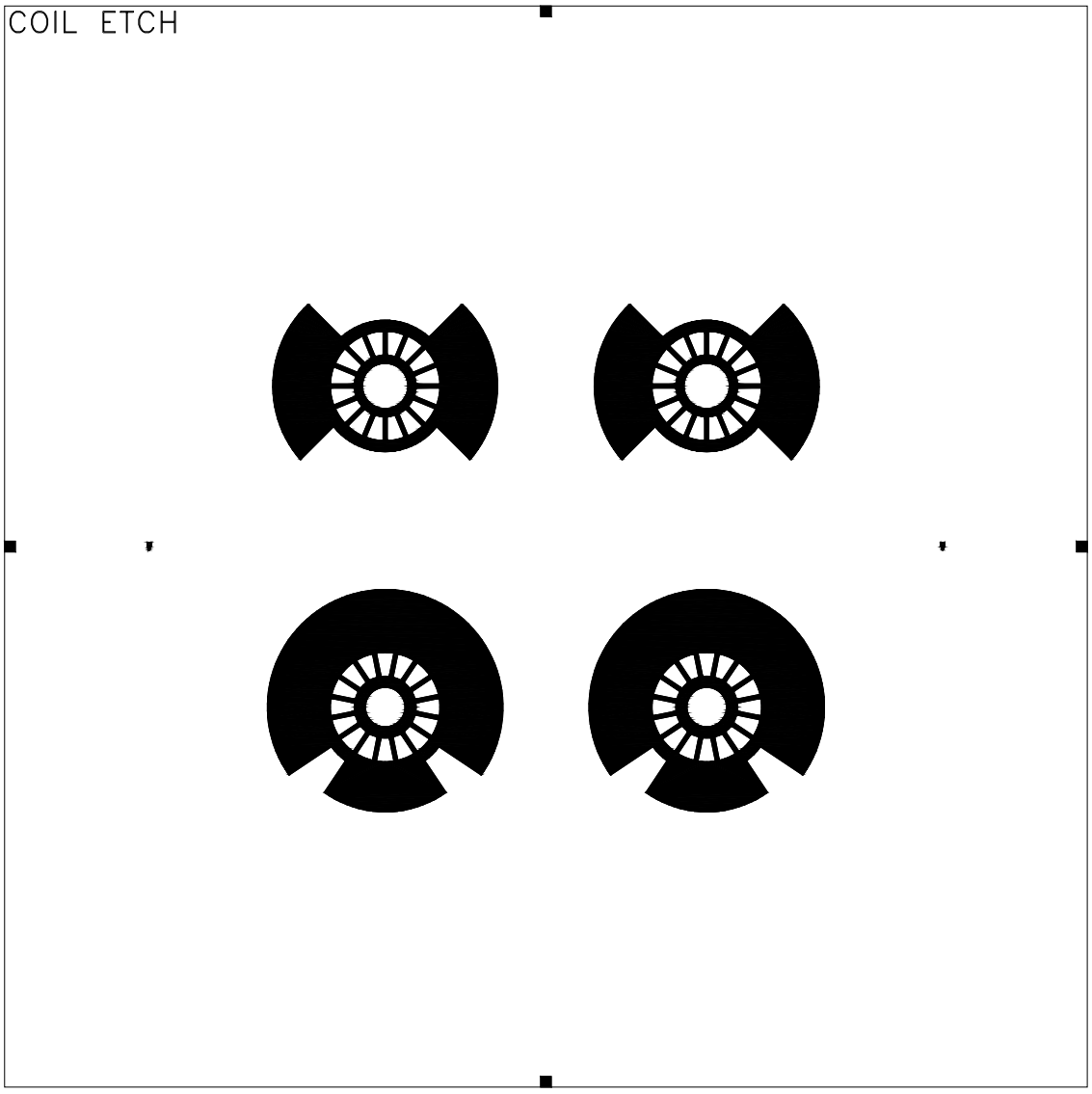

Figure B.2. Induction machine stator coil etch mask (darkfield).

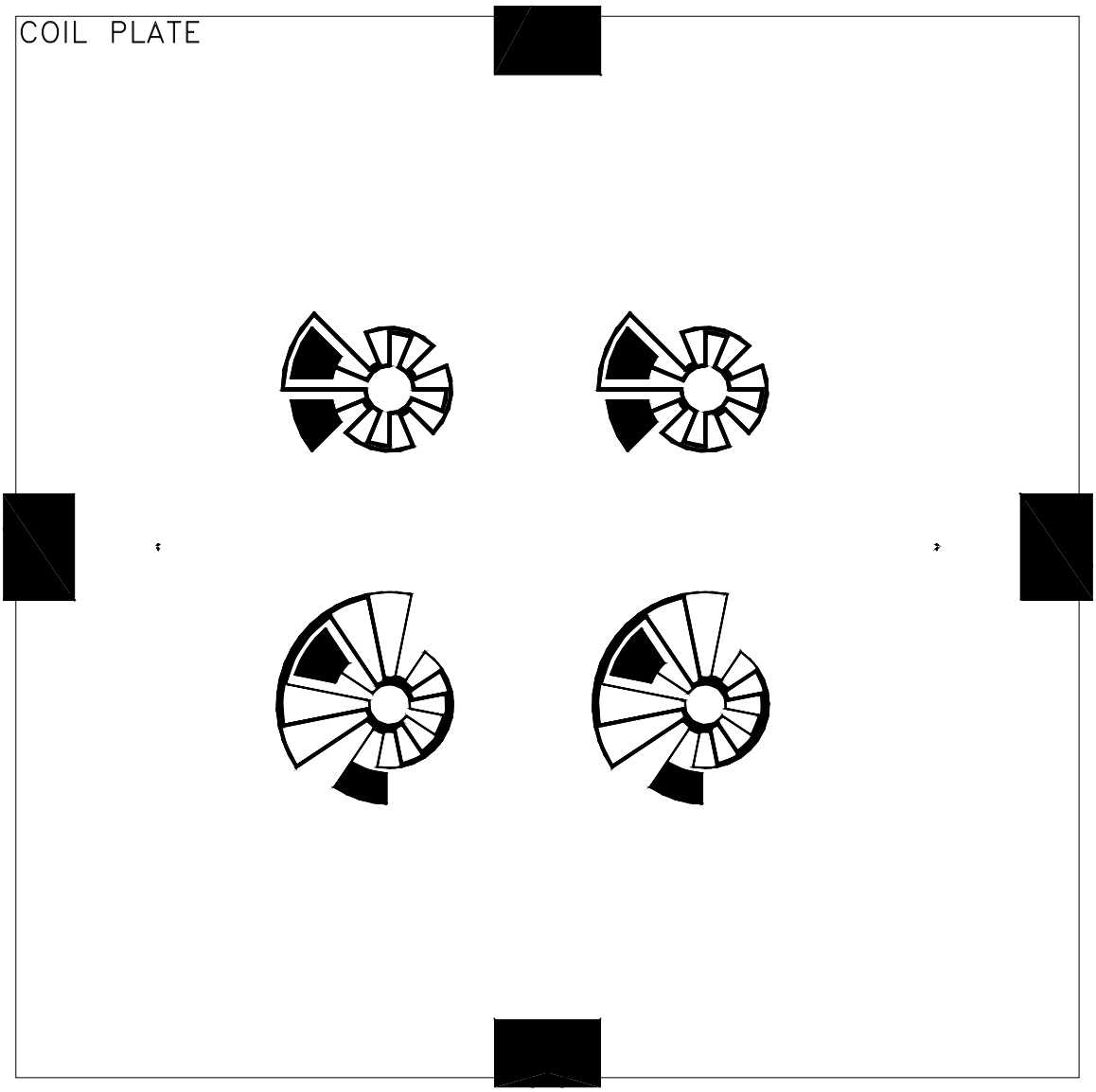

Figure B.3. Induction machine stator coil plating mask (clearfield).

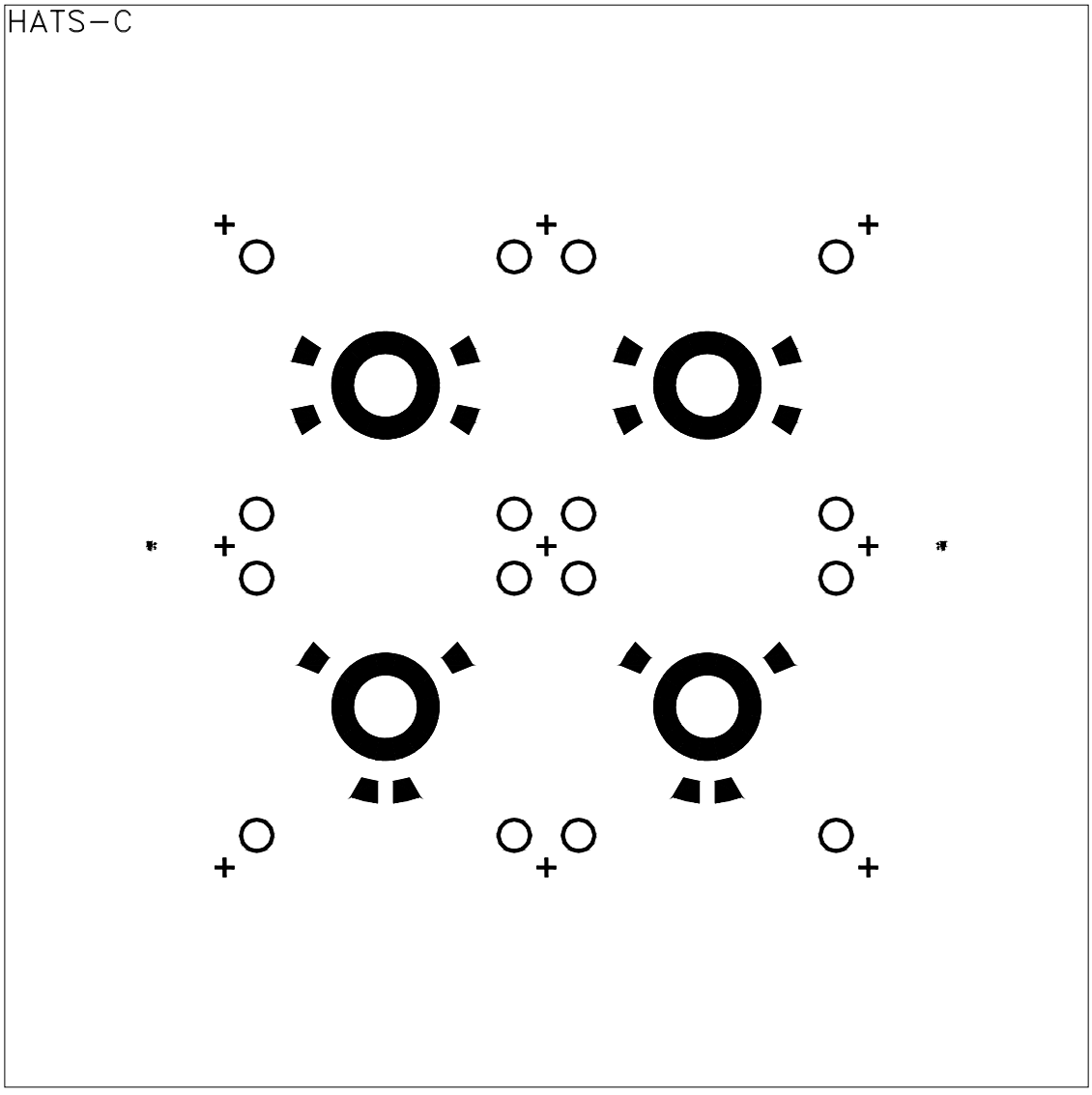

Figure B.4. Induction machine stator hat/contacts etch mask (darkfield).

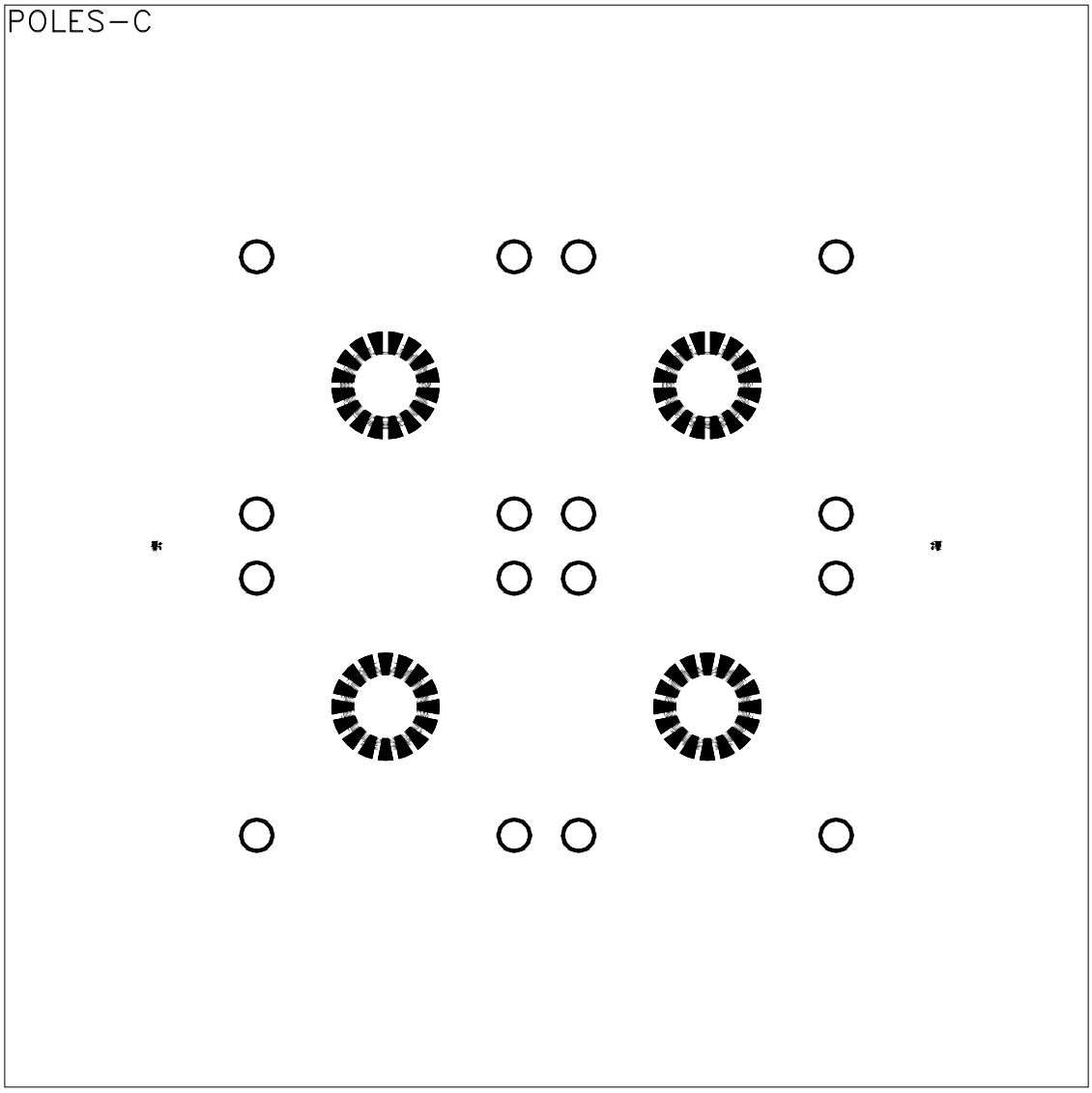

Figure B.5. Induction machine stator pole etch mask (darkfield).

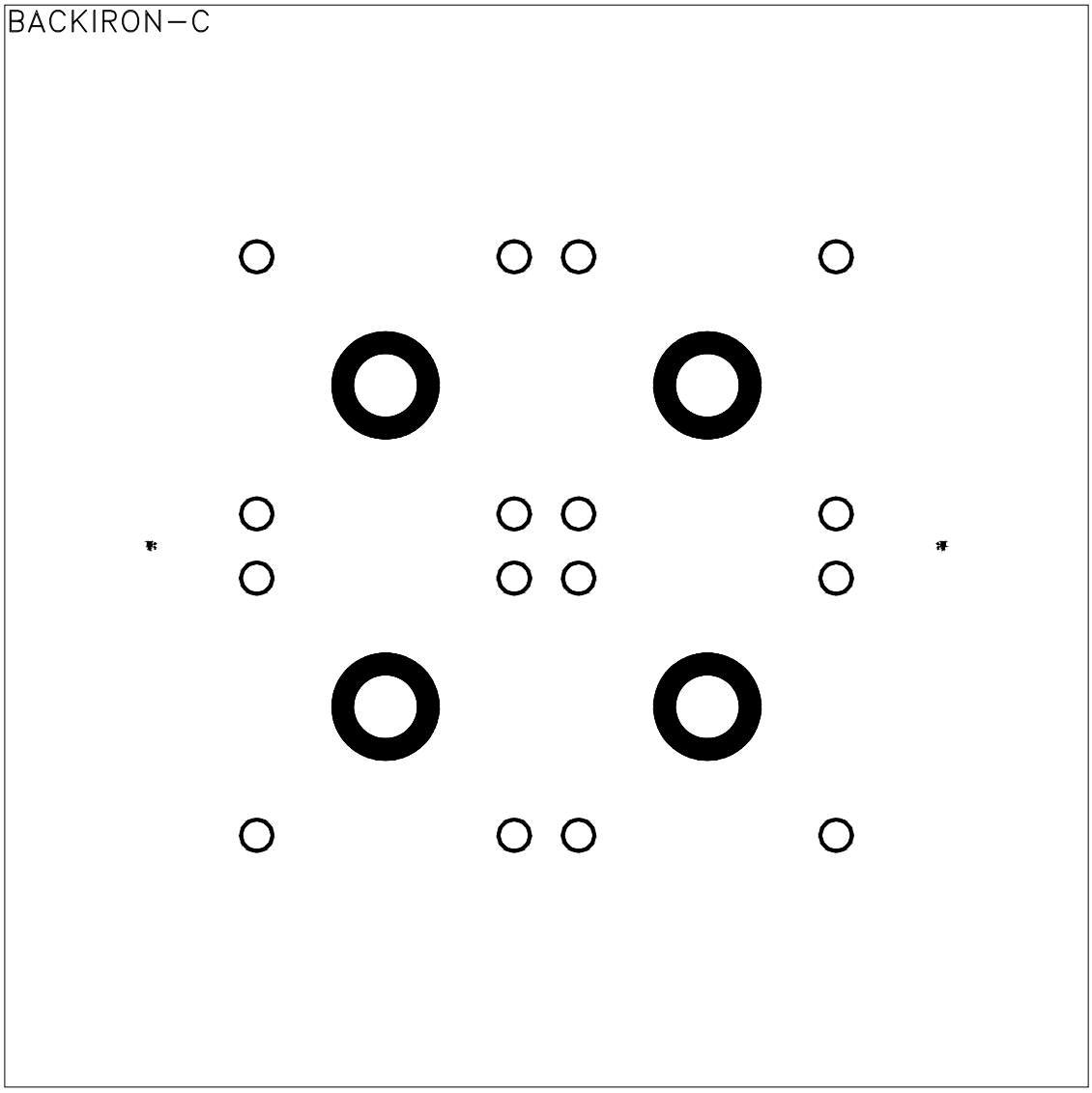

Figure B.6. Induction machine stator back iron etch mask (darkfield).

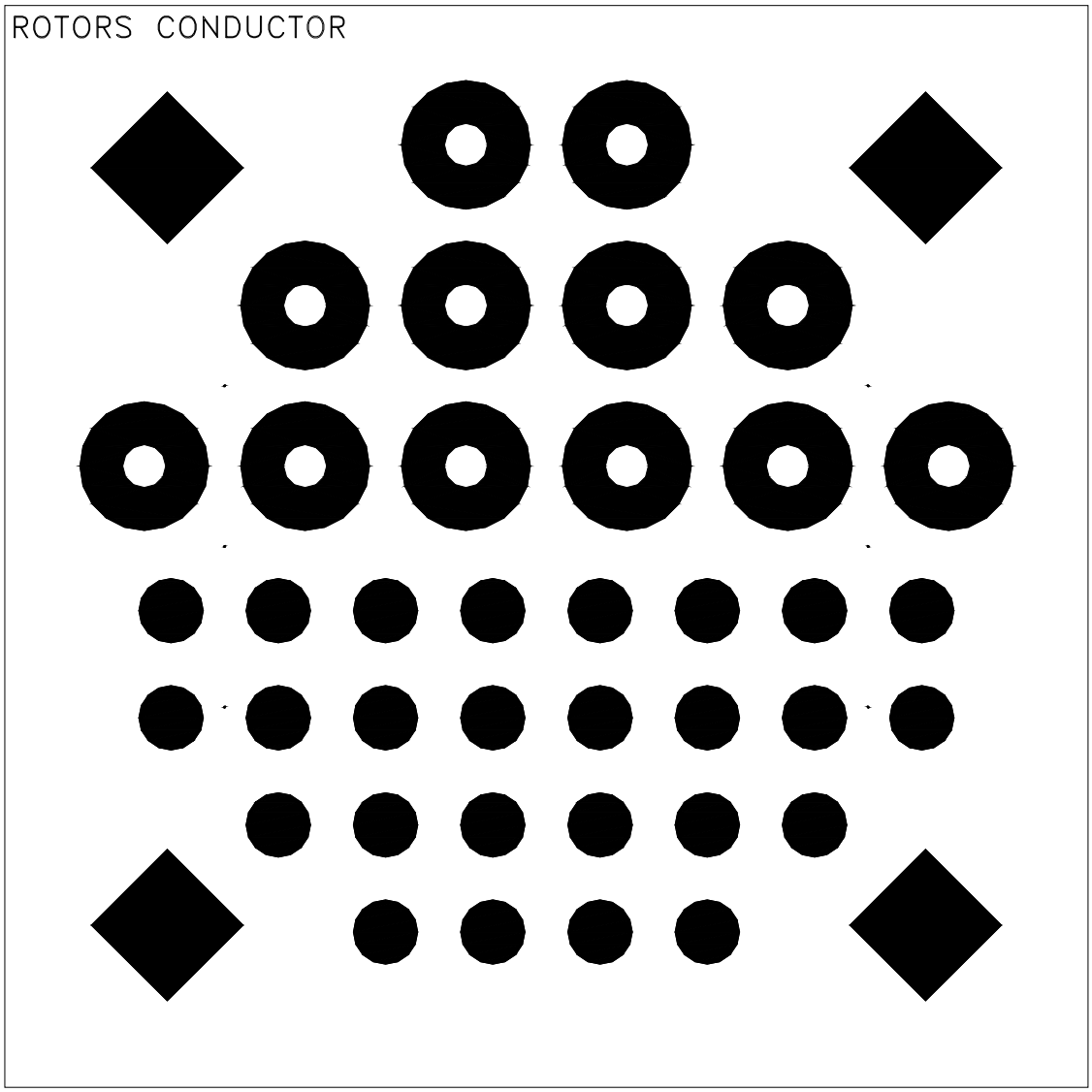

Figure B.7. Induction machine rotor conductor plating mask (clearfield).

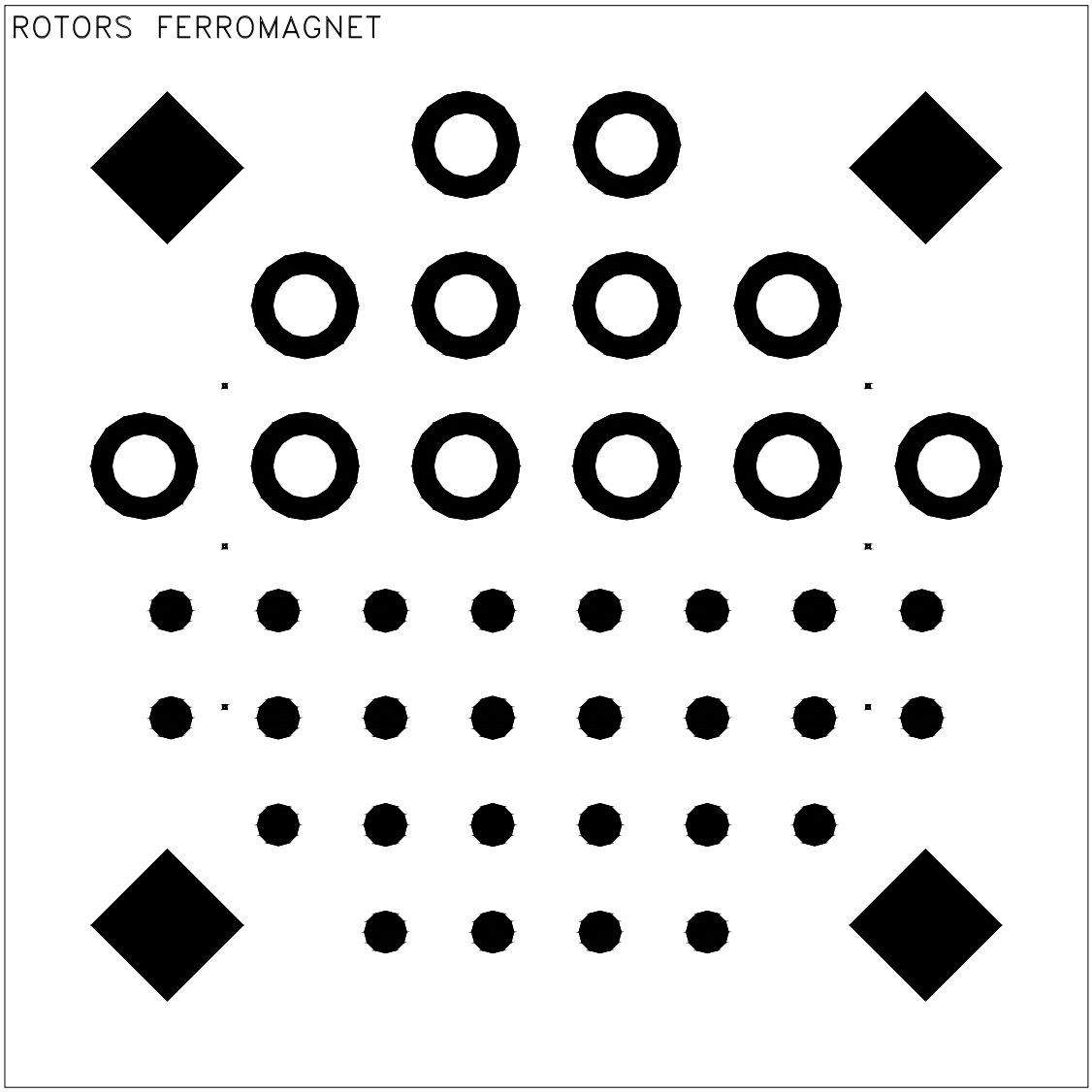

Figure B.8. Induction machine rotor ferromagnet plating mask (darkfield).

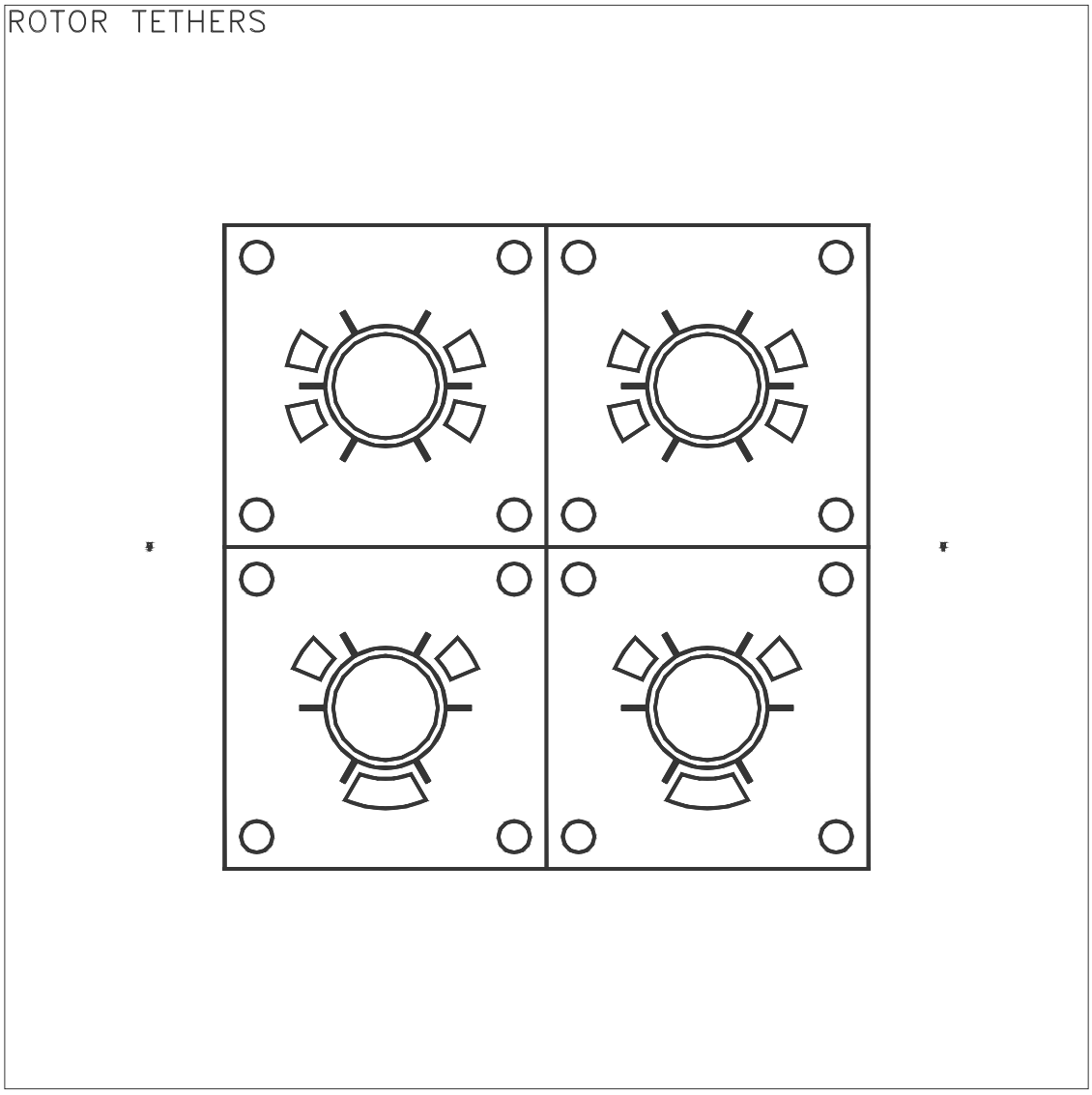

Figure B.9. Induction machine rotor tethers etch mask (darkfield).

APPENDIX C

PERMANENT MAGNET MACHINES MASKS

This section includes the two mask sets used in the fabrication of the PM machines. The first set of three masks was designed for a 100-mm substrate, and contains three 1-turn, six 2-turn, and three 4-turn machines. The second set of three masks was designed for a 75-mm substrate and contains four identical 4-turn machines with enlarged vias. All masks were clear-field for use with negative photoresists.

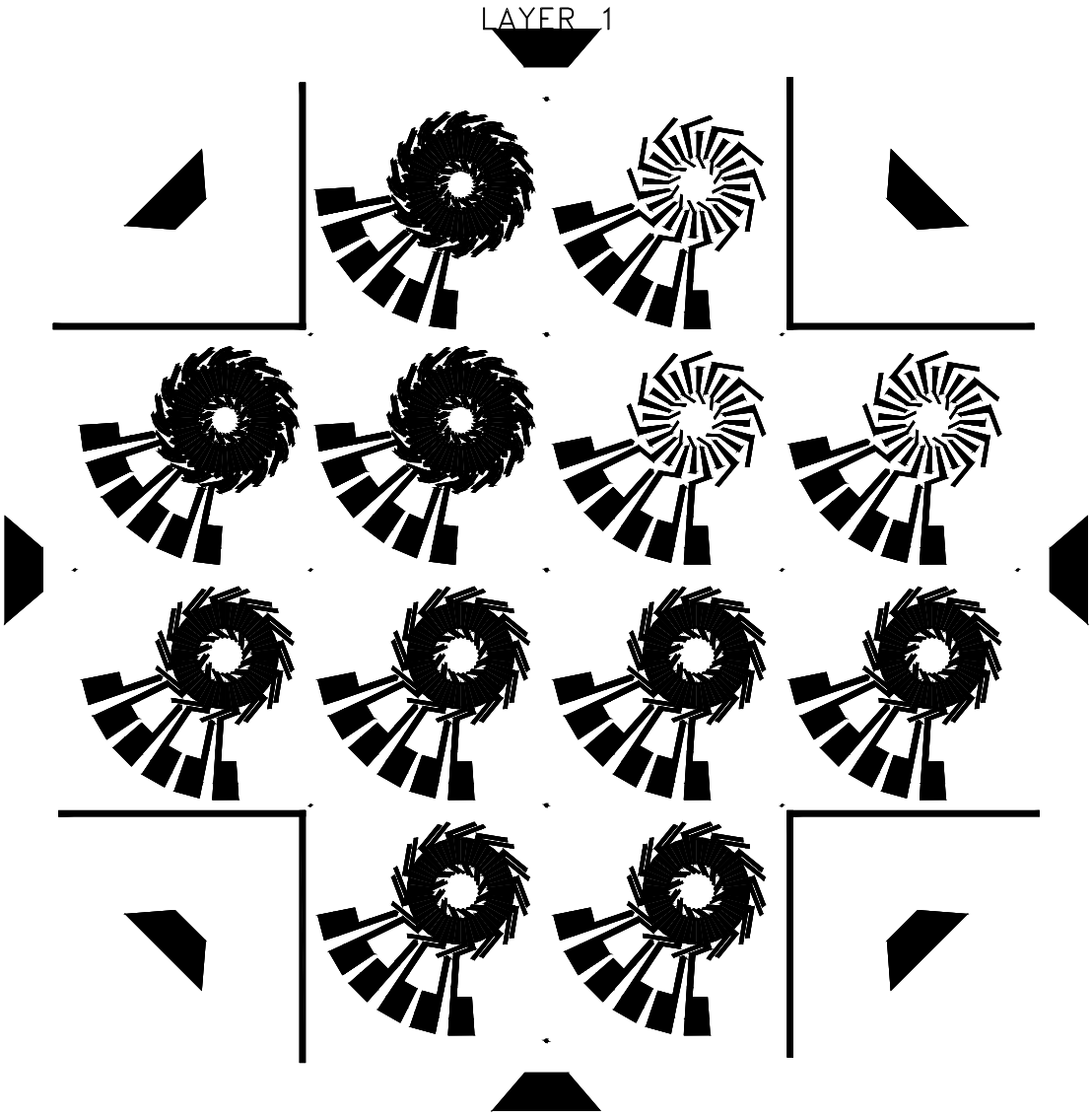

Figure C.1. PM machine stator (1st generation) coil Layer 1 mask.

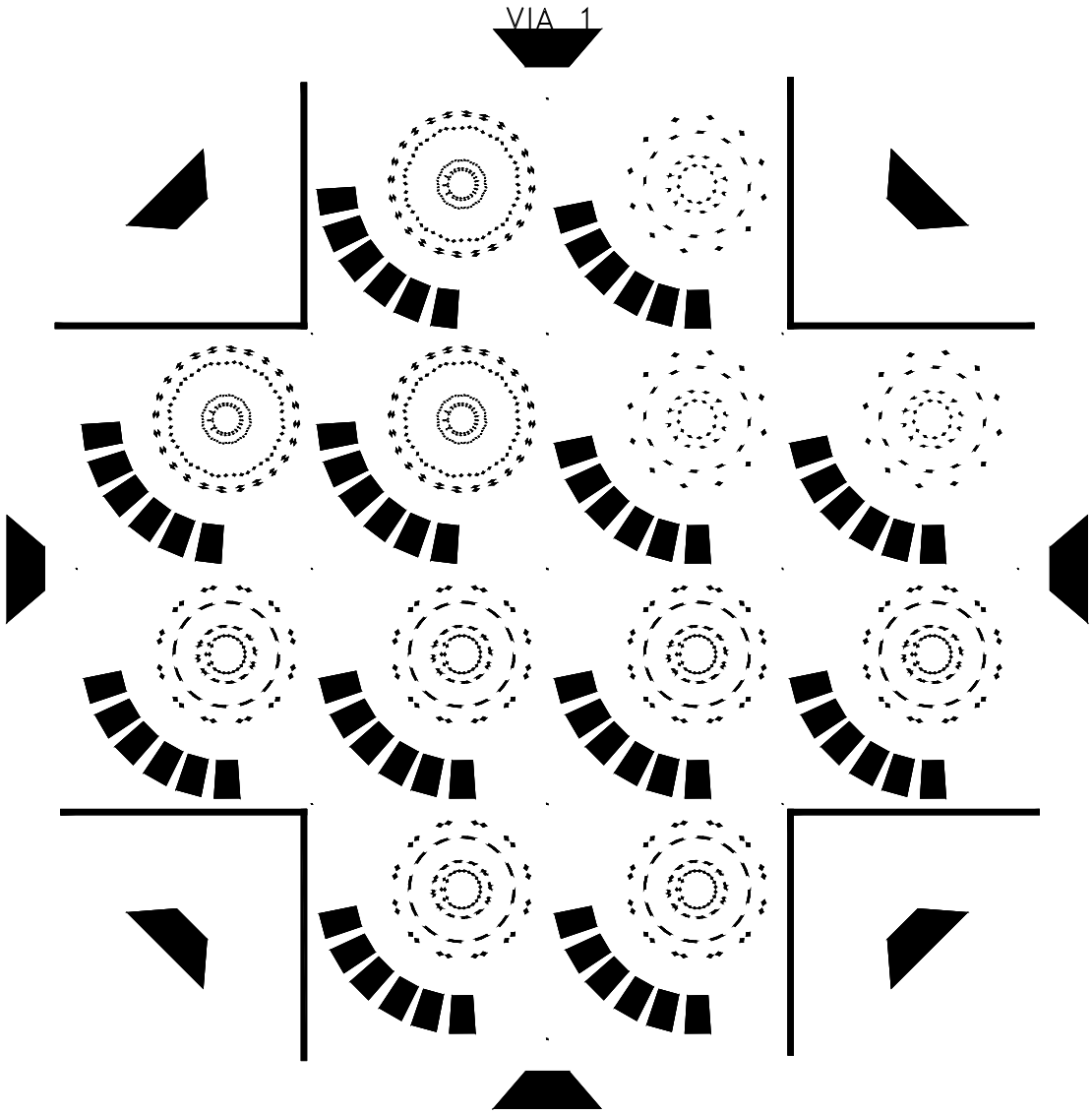

Figure C.2. PM machine stator (1st generation) coil Via 1 mask.

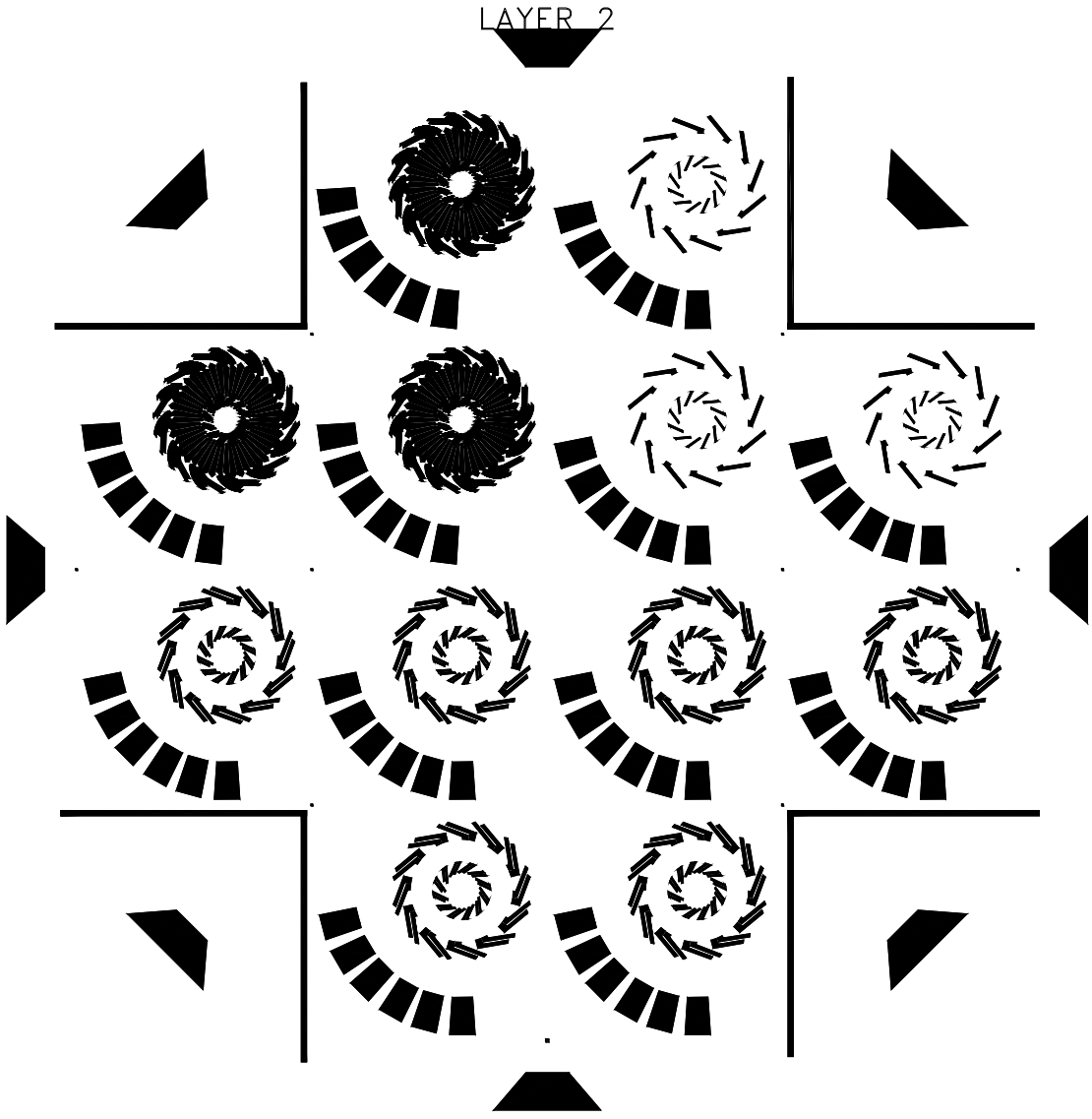

Figure C.3. PM machine stator (1st generation) coil Layer 2 mask.

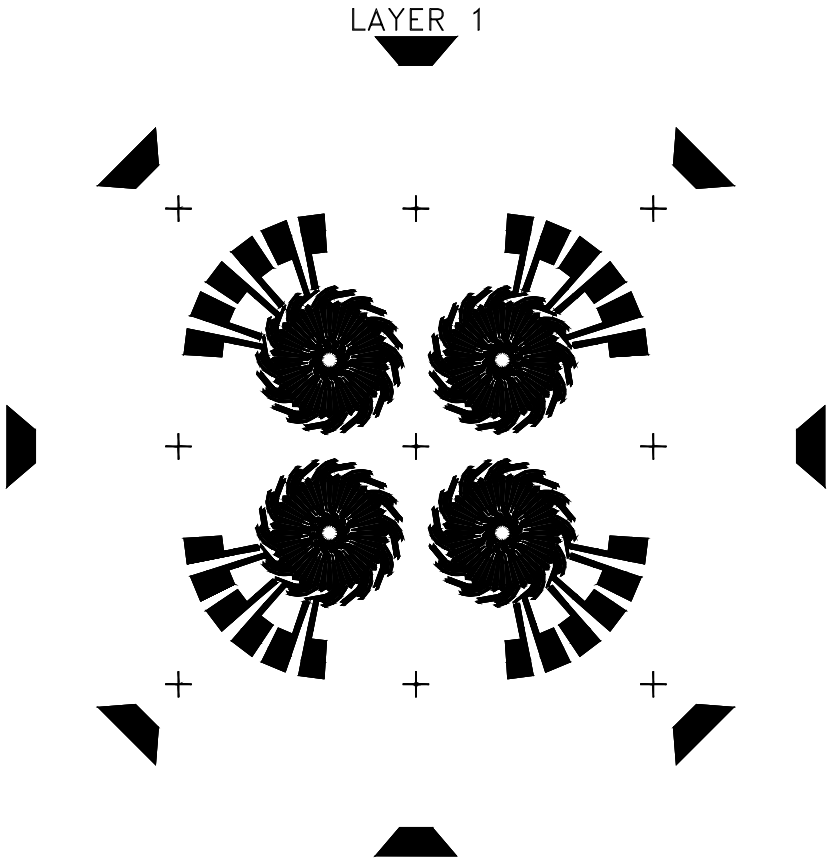

Figure C.4. PM machine stator (2nd generation) coil Layer 1 mask.

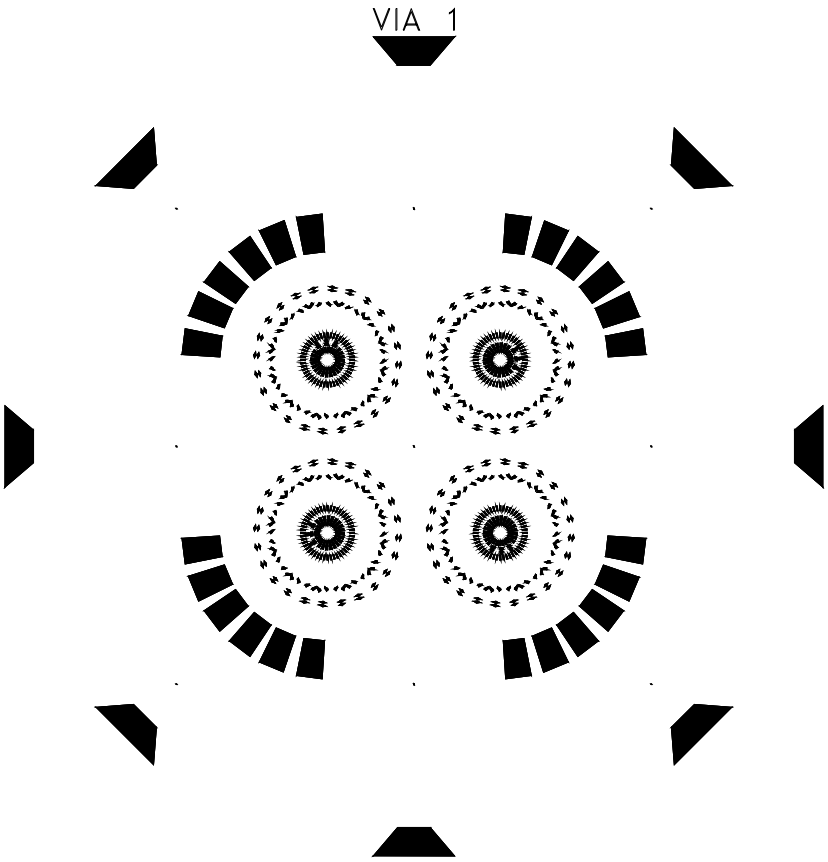

Figure C.5. PM machine stator (2nd generation) coil Via mask.

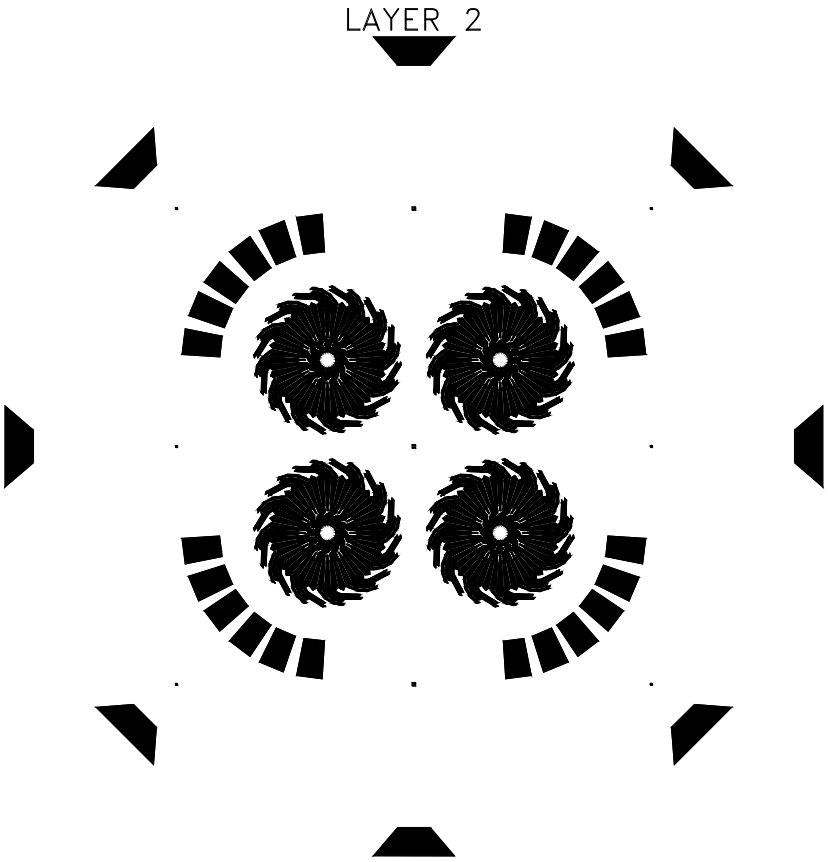

Figure C.6. PM machine stator (2nd generation) coil Layer 2 mask.

REFERENCES

1. S. A. Jacobson and A. H. Epstein, "An informal survey of power MEMS," presented at *Int. Symp. Micro-Mech. Eng.* (*ISMME 2003*), Tsukuba, Japan, Dec. 2003, Available: http://www.ttivanguard.com/montrealreconn/powerMEMS.pdf

2. A. H. Epstein and S. D. Senturia, "Macro power from micro machinery;" *Science*, vol. 276, no. 5316, p. 1211, May 1997.

3. A. H. Epstein, S. D. Senturia, et al., "Power MEMS and microengines," *Tech. Dig. Int. Conf. Solid-State Sensors and Actuators (Transducers '97)*, June 1997, pp. 753-756.

4. A. H. Epstein, S. D. Senturia, et al., "Micro-heat engines, gas turbines, and rocket engines - The MIT microengine project," AIAA Paper 97-1773, *28th AIAA Fluid Dyn. Conf.*, June 1997.

5. B. Becker and V. Thien, "High-efficiency industrial gas turbine designed for medium-load service," presented at *Power-Gen Europe 2003*, Düsseldorf, Germany, May 2003, Available: http://www.siemenswestinghouse.com/en/techpapers/gasturpowplant/index.cfm

6. C. C. Lin, et al., "Fabrication and characterization of a micro turbine/bearing rig;" *Tech. Dig. 12th IEEE Int. Conf. MEMS* (MEMS '99), Jan. 1999, pp. 529-533.

7. C. C. Lin, "Development of a microfabricated turbine-drive air bearing rig;" Ph.D. Dissertation, Massachusetts Institute of Technology, Cambridge, MA, June 1999.

8. D. J. Orr, "Macro-scale investigation of high speed gas bearings for MEMS devices;" Ph.D. Dissertation, Massachusetts Institute of Technology, Cambridge, MA, Feb. 2000.

9. E. Peikos, "Numerical simulation of gas-lubricated journal bearings for microfabricated machines;" Ph.D. Dissertation, Massachusetts Institute of Technology, Cambridge, MA, Feb. 2000.

10. A. Mehra, A. A. Ayon, I. A. Waitz, and M. A. Schmidt, "Microfabrication of high temperature silicon devices using wafer bonding and deep reactive ion etching;" *J. Microelectromech. Syst.*, vol. 8, no. 2, pp. 152-60, June 1999.

11. A. Mehra, "Development of a high power density combustion system for a silicon micro gas turbine engine;" Ph.D. Dissertation, Massachusetts Institute of Technology, Cambridge, MA, Feb. 2000.

12. A. Mehra, et al., "A six-wafer combustion system for a silicon micro gas turbine engine," *J. Microelectromech. Syst.*, vol. 9, pp. 517-27, 2000.

13. L. G. Frèchette, et al., "Demonstration of a microfabricated high-speed turbine supported on gas bearings," *Tech. Dig. Solid-State Sensor and Actuator Workshop* (Hilton Head 2000), June 2000, pp. 43-7.

14. L. G. Frèchette, "Development of a microfabricated silicon motor-driven compressor system," Ph.D. Dissertation, Massachusetts Institute of Technology, Cambridge, MA, Aug. 2000.

15. K. Lohner, K-S. Chen, A. A. Ayon, and S. M. Spearing, "Microfabricated silicon carbide microengine structures" *Proc. Symposium. Mater. Res. Soc.*, *Materials Science of Microelectromechanical Systems (MEMS) Devices,* 1999, pp. 85-90.

16. K-S. Chen, "Materials characterization and structural design of ceramic micro turbomachinery," Ph.D. Dissertation, Massachusetts Institute of Technology, Cambridge, MA, Feb. 1999.

17. K-S. Chen, A. Ayon, and S. M. Spearing, "Controlling and testing the fracture strength of silicon on the mesoscale," *J. Amer. Ceramic Soc.*, vol. 83, no. 6, pp. 1476-1484, June 2000.

18. A. A. Ayón, et al., "Characterization of a time multiplexed inductively coupled plasma etcher," *J. Electrochem. Soc*., vol. 146, pp. 339-349, Jan. 1999.

19. A. A. Ayón, X. Zhang, and R. Khanna, "Anisotropic silicon trenches 300-500 μm deep employing time multiplexed deep etching (TMDE)," *Sens. Actuators: Phys. A*, vol. 91, pp. 381-385, 2001.

20. A. A. Ayón, et al., "Characterization of silicon wafer bonding for power MEMS applications," *Sens. Actuators: Phys. A*, vol. 103, pp. 1-8, 2003.

21. N. Miki, et al., "Multi-stack silicon-direct wafer bonding for 3D MEMS manufacturing," *Sens. Actuators: Phys. A*, vol. 103, pp. 194-201, 2003.

22. S. F. Nagle and J. H. Lang; "A micro-scale electric-induction machine for a micro gas-turbine generator;" *Proc. 27th Meeting Electrostatics Soc. Amer.*, June 1999, pp. 57-66.

23. S. F. Nagle, "Analysis, design, and fabrication of an electric induction micromotor for a micro gas-turbine generator," Ph.D. Dissertation, Massachusetts Institute of Technology, Cambridge, MA, Oct. 2000.

24. L. G. Frechette, et al., "An electrostatic induction micromotor supported on gas-lubricated bearings," *Tech. Dig. 14th IEEE Int. Conf. MEMS* (MEMS 2001), Jan. 2001, pp. 290-293.

25. C. Livermore, et al., "A high-power MEMS electric induction motor," *Tech. Dig. Solid-State Sensor and Actuator Workshop* (Hilton Head 2002), June 2002, pp. 251-254.

26. C. Livermore, et al., "A high-power MEMS electric induction motor," *J. Microelectromech. Syst.*, vol. 13, no. 3, pp. 465-471, June 2004.

27. L. Steyn, et al., "Generating electric power with a MEMS electroquasistatic induction turbine-generator," *Tech. Dig. 18th IEEE Int. Conf. MEMS* (MEMS 2005), Jan 2005, (to be published).

28. L. Steyn, "A microfabricated electroquasistatic induction turbine generator" Ph.D. Dissertation, Massachusetts Institute of Technology, Cambridge, MA, (to be published c. June 2005).

29. H. Koser, F. Cros, M. G. Allen, and J. H. Lang, "A high torque density magnetic induction machine," *Tech. Dig. 11th Int. Conf. Solid-State Sensors and Actuators* (Transducers '01), June 2001, pp. 284-287.

30. H. Koser, F. Cros, M. G. Allen, and J. H. Lang, "Magnetic diffusion modeling in nonlinear micro-media: A modified finite-difference time-domain approach," *Proc. 6th Int. Conf. Model. Sim. of Microsyst*. (MSM 2003), Feb. 2003, pt. 2, vol.2, pp. 408-411.

31. H. Koser, "Development of magnetic induction machines for micro turbo machinery," Ph.D. Dissertation, Massachusetts Institute of Technology, Cambridge, MA, June 2002.

32. F. Cros., "Developpement d'une micromachine a induction magnetique – developpement de Techniques de microfabrication pour micro-electroaimants," Ph.D. Dissertation, Ecole Doctorale de Toulouse, France, Sept. 2002.

33. H. Koser and J. H. Lang, "Magnetic induction micro machine – Part I: Design and analysis," *J. Microelectromech. Syst*., (submitted for review).

34. F. Cros, H. Koser, M. G. Allen, and J. H. Lang, "Magnetic induction micro machine – Part II: Fabrication and testing," *J. Microelectromech. Syst*., (submitted for review).

35. H. Koser, F. Cros, M. G. Allen, and J. H. Lang, "Magnetic induction micro machine – Part III: Eddy currents and nonlinear effects," *J. Microelectromech. Syst*., (submitted for review).

36. H. Guckel, et al., “A first functional current excited planar rotational magnetic micromotor;” *Proc. IEEE Micro Electro Mechanical Systems* (MEMS ’93), Feb. 1993, pp. 7-11.

37. H. Guckel, et al., “Planar rotational magnetic micromotors,” *Int. J. Appl. Electromagn. in Mat.*, vol. 4, no. 4, pp. 377-382, June 1994.

38. C. H. Ahn, Y. J. Kim, and M. G. Allen, “A planar variable reluctance magnetic micromotor with fully integrated stator and coils” *J. Microelectromech. Syst*., vol. 2, no. 4, pp. 165-73, Dec. 1993.

39. A. M. Jungreis and A. W. Kelley, “The axial air gap wobble motor – an appropriate topology for magnetic micromotors,” *Conf. Rec. 1995 IEEE Ind. Appl. Conf.* (IAS '95), pt. 1, vol.1, pp. 781-788.

40. B. Wagner, M. Kreutzer, and W. Benecke, “Permanent magnet micromotors on silicon substrates,” *J. Microelectromech. Syst*., vol. 2, no. 1, pp. 23-29, Mar. 1993.

41. K.-P. Kamper, et al., “Electromagnetic permanent magnet micromotor with integrated micro gear box,” *Proc. 5th Int. Conf. New Actuators* (Actuator ‘96), June 1996, pp. 429-432.

42. U. Berg, et al., “Series production and testing of a micro motor,” *Proc. 6th Int. Conf. New Actuators* (Actuator ‘98), June 1998, pp. 552-555.

43. P.-A.Gilles, J. Delamare, O. Cugat, and J.-L. Schanen, “Design of a permanent magnet planar synchronous micromotor,” *Proc. 35th Mtg. IEEE Industry Appl. Soc.*, Oct. 2000, vol. 1, pp. 223-227.

44. C. Yang, et al., “An axial flux electromagnetic micromotor,” *J. Micromech. Microeng.*, vol. 11, pp. 113-117, 2001.

45. T. G. Wiegele, “Micro-turbo-generator design and fabrication: a preliminary study,” *Proc. 31st Intersociety Energy Conversion Engineering Conference* (IECEM 96), Aug. 1996, part 4, pp. 2308-2313.

46. A. S. Holmes, G. Hong, K. R. Pullen, and K. R. Buffard, “Axial-flow microturbine with electromagnetic generator: design, CFD simulation, and prototype demonstration,” *Tech. Dig. 17th IEEE Int. Conf. MEMS* (MEMS ‘04), Jan. 2004, pp. 568-571.

47. M. A. Schmidt, “Wafer-to-wafer bonding for microstructure formation,” *Proc. IEEE*, vol. 86, no. 8, pp. 1575-1585, Aug. 1998.

48. Q.-Y. Tong and U. Gösele, *Semiconductor Wafer Bonding: Science and Technology*, New York: Wiley & Sons, 1999.

49. B. Müller and A. Stoffel, "Tensile strength characterization of low-temperature fusion-bonded silicon wafers," *J. Micromech. Microeng.*, vol. 1, pp. 161-166, 1991.

50. G. Kissinger and W. Kissinger, "Void-free silicon-wafer-bond strengthening in the 200-400 degrees C range," *Sens. Actuators: Phys. A*, vol. A36, no. 2, pp. 149-156, Apr. 1993.

51. S. N. Farrens, C. E. Hunt, B. E. Roberds, and J. K. Smith, "A kinetics study of the bond strength of direct bonded wafers," *J. Electrochem. Soc.*, vol. 141, no. 11, pp. 3225-30, Nov. 1994.

52. Q.-Y. Tong, G. Cha, R. Gafiteanu, and U. Gösele, "Low temperature wafer direct bonding," *J. Microelectromech. Syst*., vol. 3, no. 1, pp. 29-35, Mar. 1994.

53. A. Berthold and M.J. Vellekoop, "IC-compatible silicon wafer-to-wafer bonding, *Sens. Actuators: Phys. A*, vol. 60, 208-211, 1997.

54. Q.-Y. Tong, W. J. Kim, T.-H. Lee, and U. Gösele, "Low vacuum wafer bonding," *Electrochem. Solid-State Lett.*, vol. 1, no. 1, pp. 52-53, 1998.

55. C. H. Ahn and M. G. Allen, "A fully integrated surface micromachined magnetic microactuator with a multilevel meander magnetic core," *J. Microelectromech. Syst*., vol. 2, no. 1, pp. 15-22, Mar. 1993.

56. J.-W. Park and Mark G. Allen, "Ultra low-profile micromachined power inductors with highly laminated Ni/Fe cores: Application to low-megahertz DC-DC converters," *IEEE Trans. Magn*., vol. 39, no. 5, pp. 3184-3186, Sept. 2003.

57. M. G. Allen, "MEMS Technology for the fabrication of RF components," *IEEE Trans. Magn.*, vol. 39, no. 5, pp. 3073-3078, Sept. 2003.

58. J.-W. Park, J. Y. Park, Y.-H. Joung, and M. G. Allen, "Fabrication of high current and low profile micromachined inductor with laminated Ni/Fe core," *IEEE Trans. Comp. Packag. Technol*., vol. 25, pp. 106–111, Mar. 2002.

59. J. Y. Park, S. H. Han, and M. G. Allen, "Batch-fabricated microinductors with electroplated magnetically anisotropic and laminated alloy cores," *IEEE Trans. Magn*., vol. 35, pp. 4291–4300, Sept. 1999.

60. J.-W. Park and M. G. Allen, "Ultralow-profile micromachined power inductors with highly laminated Ni/Fe cores: Application to Low-Megahertz DC-DC converters," *IEEE Trans. Magn.*, vol. 39, pp. 3184–3186, Sept. 2003.

61. C. R. Sullivan and S. R. Sanders, "Microfabrication process for high frequency power-conversion transformers," *Proc. 26th Annu. Power Electronics Specialists Conf.*, June 1995, pp. 658–664.

62. M. Xu, T. M. Liakopoulos, C. H. Ahn, S. H. Han, and H. J. Kim, "A microfabricated transformer for high-frequency power or signal conversion," *IEEE Trans. Magn*., vol. 34, pp. 1369–1371, July 1998.

63. T. Laurila, K. Zeng, and J. K. Kivilahti, "Failure mechanism of Ta diffusion barrier between Cu and Si," *J. Appl. Phys*., vol. 88, no. 6, pp. 3377-3384, Sept. 2000.

64. S.-Q. Wang, S. Suthar, K. Hoeflich, and B. J. Burrow, "Diffusion barrier properties of TiW between Si and Cu," *J. Appl. Phys.*, vol. 73, no. 5, pp. 2301-2320, Mar. 1993.

65. T. Laurila, "Tantalum-based diffusion barriers for copper metallization," Ph.D. Dissertation, Helsinki University of Technology, Espoo, Finland, Dec. 2001.

66. C. H. Seah, S. Mridha, and L. H. Chan, "Annealing of copper electrodeposits," *J. Vac. Sci. Tech. A*, vol. 17, no. 4, pp. 1963-1967, July 1999.

67. A. S. Kao and P. Kasiraj, "Effect of magnetic annealing on plated permalloy and domain configurations in thin-film inductive head," *IEEE Trans. Magn*., vol. 27, no. 6, pp. 4452-4457, Nov. 1991.

68. J.-J. Sun, et al., "High-aspect-ratio copper via filling used for three-dimensional chip stacking," *J. Electrochem. Soc*., vol. 150, pp. G355-G358, July 2003.

69. J. Lammeraner and M. Stafl, *Eddy Current*, London: Iliffe, ch. 1-2, 1966.

70. A.E. Fitzgerald, C. Kingsley, Jr., and S. D. Umans, *Electric Machinery*, 6th Ed., New York: McGraw Hill, 2002.

71. M. S. Sarma, *Electric Machines*, New York: West, 2nd Ed., ch. 5,8, 1994.

72. R. M. Bozorth, *Ferromagnetism*, New York: IEEE Press, Reissue, 1993.

73. D. M. Freeman, A. J. Aranyosi, M. J. Gordon, and S. S. Hong, "Multidimensional motion analysis of MEMS using computer microvision," *Tech. Dig. Solid-State Sensor and Actuator Workshop* (Hilton Head 1998), June 1998, pp. 150-155.

74. W. C. Young, *Roark's Formulas for Stress and Strain*, 6th Ed., New York: McGraw Hill, 1989.

75. H. Lorenz, et al., "High-aspect-ratio, ultrathick, negative-tone near-UV photoresist and its applications for MEMS," *Sens. Actuators: Phys. A*, vol. 64, no. 1, pp. 33-39, Jan. 1998.

76. O. Cugat, J. Delamare, and G. Reyne, "Magnetic micro-actuators and systems (MAGMAS)," *J. Microelectromech. Syst.*, vol. 39, no. 5, pp. 3607-3612, Nov. 2003.

77. "MMPA Standard No. 0100-00, Standard Specifications for Permanent Magnet Materials," published by International Magnetics Association (formerly Magnetic Materials Producers Association), Available: http://www.intl-magnetics.org/pdfs/0100-00.pdf.

78. S. Das, "Magnetic machines and power electronics for power-MEMS applications," Ph.D. Dissertation, Massachusetts Institute of Technology, Cambridge, MA, (to be published c. Aug. 2005).

79. P.A. Gilles, J. Delamare, and O. Cugat, "Rotor for a brushless micromotor," *J. Magnetism Magn. Mat.*, vol. 242-245, pp. 1186-1189, 2002.

80. A. B. Frazier and M. G. Allen, "Metallic microstructures fabricated using photosensitive polyimide electroplating molds," *J. Microelectromech. Syst.*, vol. 2, no. 2, pp. 87-94, June 1993.

81. X. Liu, G. Zangari, and L. Shen, "Electrodeposition of soft, high moment Co–Fe–Ni thin films," *J. Appl. Phys.*, vol. 87, no. 9, pp. 5410-5412, May 2001.

VITA

David P. Arnold was born in 1978 in Kissimmee, Florida. He received dual B.S. degrees in electrical and computer engineering in 1999, followed by the M.S. degree in electrical engineering in 2001, from the University of Florida, Gainesville. He received the Ph.D. degree in electrical engineering at the Georgia Institute of Technology, Atlanta, in 2004.

He was awarded fellowships from Tau Beta Pi in 1999 and from the National Science Foundation in 2000. For his master's thesis, he developed piezoresistive silicon microphones and MEMS-based acoustic array technologies for aeroacoustic measurements in the Interdisciplinary Microsystems Group at the University of Florida. In 2002, he began his doctoral research at the Microsensor and Microactuator Laboratory at Georgia Tech, focusing on magnetic micromachines for microengine power generation. He has since accepted a postdoctoral research position at Georgia Tech, while preparing for a career in academia.

His research interests include the design, fabrication, and characterization of magnetic, acoustic, and mechanical microsystems. Mr. Arnold is also a member of IEEE, Eta Kappa Nu and Tau Beta Pi.